NUREG/CR-6933
PNNL-16292

Assessment of Crack Detection in Heavy-Walled Cast Stainless Steel Piping Welds Using Advanced Low-Frequency Ultrasonic Methods

Pacific Northwest National Laboratory

U.S. Nuclear Regulatory Commission
Office of Nuclear Regulatory Research
Washington, DC 20555-0001

NUREG/CR-6933
PNNL-16292

Assessment of Crack Detection in Heavy-Walled Cast Stainless Steel Piping Welds Using Advanced Low-Frequency Ultrasonic Methods

Manuscript Completed: August 2006
Date Published: March 2007

Prepared by
M.T. Anderson, S.L. Crawford, S.E. Cumblidge,
K.M. Denslow, A.A. Diaz, S.R. Doctor

Pacific Northwest National Laboratory
Richland, WA 99352

D.A. Jackson and W.E. Norris, NRC Project Managers

Prepared for
Division of Fuel, Engineering and Radiological Research
Office of Nuclear Regulatory Research
U.S. Nuclear Regulatory Commission
Washington, DC 20555-0001
NRC Job Code Y6604

Abstract

Studies conducted at the Pacific Northwest National Laboratory in Richland, Washington, have focused on assessing the effectiveness and reliability of novel approaches to nondestructive examination (NDE) for inspecting coarse-grained, cast stainless steel reactor components. The primary objective of this work is to provide information to the U.S. Nuclear Regulatory Commission on the effectiveness and reliability of advanced NDE methods as related to the inservice inspection of safety-related components in pressurized water reactors (PWRs). This report provides progress, recent developments, and results from an assessment of low frequency ultrasonic testing (UT) for detection of inside surface-breaking cracks in cast stainless steel reactor piping weldments as applied from the outside surface of the components.

Vintage centrifugally cast stainless steel piping segments were examined to assess the capability of low-frequency UT to adequately penetrate challenging microstructures and determine acoustic propagation limitations or conditions that may interfere with reliable flaw detection. In addition, welded specimens containing mechanical and thermal fatigue cracks were examined. The specimens were fabricated using vintage centrifugally cast and statically cast stainless steel materials, which are typical of configurations installed in PWR primary coolant circuits.

Ultrasonic studies on the vintage centrifugally cast stainless steel piping segments were conducted with a 400-kHz synthetic aperture focusing technique and phased array technology applied at 500 kHz, 750 kHz, and 1.0 MHz. Flaw detection and characterization on the welded specimens was performed with the phased array method operating at the frequencies stated above. This report documents the methodologies used and provides results from laboratory studies to assess baseline material noise, crack detection, and length-sizing capability for low-frequency UT in cast stainless steel piping.

Foreword

Cast stainless steel (CSS) material was used extensively in the primary pressure boundary of pressurized water reactors (PWRs) due to its relatively low cost and resistance to corrosion. The American Society of Mechanical Engineers (ASME) Boiler and Pressure Vessel (BPV) Code requires periodic inservice inspection (ISI) of welds in the primary pressure boundary. Because of background radiation and access limitations, inspection personnel use ultrasonic testing (UT) techniques rather than radiography to inspect these welds. In most applications, UT can reliably detect and accurately size flaws that may occur during service. This is not the case for CSS material.

The coarse-grained and anisotropic microstructure of CSS material makes it difficult to inspect CSS components such as statically cast elbows, statically cast pump bowls, and centrifugally cast stainless steel piping. Similar inspection problems exist for dissimilar metal welds and weld-overlay-repaired pipe joints. The large grain sizes of these materials strongly affect the propagation of ultrasound by causing severe attenuation, change in velocity, and scattering of ultrasonic energy. Thus, the signal patterns originating from flaws can be difficult to distinguish from scatter. In addition, the result of redirection of the sound beam may be that some portions of the material are not examined.

Given the unreliability of volumetric examination of CSS material and considering the occupational dose incurred by inspection personnel while performing these inspections, industry representatives proposed removing the BPV Code requirement to inspect CSS piping welds. Because these welds are in safety-related systems, the U.S. Nuclear Regulatory Commission requested that the ASME table the proposal to allow time for further study. The staff searched the literature and inquired at national and international research organizations but discovered no active research programs. The staff then initiated a study at Pacific Northwest National Laboratory (PNNL) to research the feasibility of an effective and reliable inspection technique.

Inspection personnel typically employ volumetric UT methods from the outside-surface (OD) of piping components where they have ready access. However, these OD inspection methods have not been demonstrated to be reliable for coarse-grained materials such as CSS. Inspection personnel have successfully employed inside-surface (ID) eddy-current test (ET) protocols in certain nuclear applications. A direct-contact methodology that is sensitive to surface-breaking cracks likely has an inherently higher probability of successful detection than an OD inspection method. PNNL thus evaluated the applicability and effectiveness of an ID inspection technique. PNNL (1) studied advanced eddy-current probe configurations that provide sensitivity to both axially and circumferentially oriented, near-surface flaws and (2) investigated the reliability and effectiveness of an ID inspection technique. The studied specimens contained cracks created by methods proven to produce realistic, surface-connected mechanical and thermal fatigue cracks.

This report provides a firm engineering basis for evaluating the technical approach for CSS component inspections. This report describes an eddy-current method—as verified by the PNNL study—which is very effective at detecting these types of surface-breaking cracks when the ID is accessible. This report also describes a number of implementation details that must be resolved before this method can be employed for ISI.

A feasible and effective inspection method for CSS material has been identified. This material is located in safety-related systems. Therefore, the industry should take the steps necessary to add ET to its arsenal of nondestructive examination tools to effectively examine CSS material.

Brian W. Sheron, Director
Office of Nuclear Regulatory Research
U.S. Nuclear Regulatory Commission

Contents

Figures

Tables

Executive Summary

Laboratory investigations were conducted for the U.S. Nuclear Regulatory Commission (NRC) at the Pacific Northwest National Laboratory (PNNL) to evaluate the effectiveness and determine the reliability of advanced nondestructive examination (NDE) methods used on light water reactor components containing cast stainless steel (CSS) material. The specific goal of this work is to assess various NDE methods to directly improve our ability to detect, localize, and, if possible, size cracks in coarse-grained steel components used in the U.S. nuclear industry.

The volumetric examination of vintage CSS piping existing in operating nuclear power plants remains a significant challenge to NDE technologies. Low-frequency ultrasonic testing (UT) offers the capability to penetrate relatively thick-walled sections of primary piping circuits. However, detection and characterization of flaws is problematic due to the varied microstructures from materials of both centrifugally cast stainless steel (CCSS) and statically cast stainless steel (SCSS). During this study, we built upon decades of work at PNNL with UT using a low-frequency/Synthetic Aperture Focusing Technique (SAFT) by migrating to an approach that uses state-of-the-art phased array methods operating at low frequencies to determine if detection and sizing of cracks could be improved. Phased array (PA) techniques offer the ability to electronically steer the UT beam through multiple propagation angles nearly simultaneously so that any existing "windows" for optimum material penetration may be accessed more readily. Phased array systems are being increasingly deployed on a wide range of component inspections because their use allows a more rapid examination than conventional automated UT while providing enhanced imaging capabilities to facilitate data analyses.

Longitudinal waves produced by dual phased arrays operating at 500 kHz, 750 kHz, and 1.0 MHz, and a conventionally designed dual transducer operating at 400 kHz, were applied to thick-section (65–80 mm, or 2.6–3.2 in.) unflawed CCSS piping segments to determine whether ultrasound at these frequencies could be expected to adequately penetrate the varied microstructures and to assess inherent background noise that may interfere with detection and characterization of flaws. The work indicated that the lower two frequencies (400 kHz and 500 kHz) produced the best overall corner-trap responses obtained from the machined end of the specimens.

Over normalized scan lengths, the 400-kHz SAFT-processed images provided the most consistent corner detection, while the best signal-to-noise ratio was obtained from the 500-kHz phased array method. The frequency response from returned corner-trap signals in vintage CCSS shows that 500 kHz is a stable operating range, while higher frequencies exhibit variability and filtering due to the microstructures. Certain vintage CCSS microstructures produced signal loss and associated high background noise in certain areas of the tested segments. Similar CCSS microstructures may be present in portions of primary coolant system piping of early Westinghouse-designed nuclear power plants, and in these areas, ultrasonic inspection reliability will be affected. This research has shown that the use of large-aperture, low-frequency phased arrays, coupled with careful analyses of data images are necessary to support robust and effective examination of this material.

Baseline material analyses indicate that vintage CCSS piping microstructures may produce certain regions of diminished UT response. From the results of detected corner-trap responses using the 500-kHz PA probe, areas up to approximately 10 cm (4 in.) in circumferential length were observed to be the worst cases of diminished response. Given the high fracture toughness of CCSS piping, flaws would need to be 5 to 10 times longer than these worst-case areas to challenge structural integrity. Therefore, it is concluded that any structurally significant cracks would be detected in CCSS, as these cracks would extend well beyond the diminished response regions.

The 500-kHz PA data show that background UT noise due to scattering from the CCSS grains does not appear to cause detected responses that one might misinterpret as a crack. However, small flaws located very near inner diameter (ID) geometry, such as counterbore, may be overlooked because of the large-amplitude, broad time base responses from these geometrical reflectors. Performing examinations with a wider range of flaw lengths, through-wall depths, and at varied distances from ID counterbore and weld root conditions may determine the limitations to flaw detection as a function of spatial location relative to geometrical reflectors. In addition, the results suggest that outer diameter (OD) weld profiling and ID contour mapping using focused straight-beam methods should be performed on all CCSS welds prior to implementing any angle beam UT procedure.

The capability of low-frequency phased array methods to detect and characterize cracks was explored using a set of specimens developed by the nuclear industry. These specimens contain mechanical and thermal fatigue cracks adjacent to welds joining CSS materials in configurations representative of those installed in Westinghouse-designed primary coolant systems. The specimens are useful but restrictive by their small size and the short length of cracks that they contain relative to the size of zones with diminished signal response and the size of critical flaws. Further assessment is warranted to put the PA effectiveness into perspective regarding component structural integrity. Both CCSS and SCSS piping materials were used to fabricate these short circumferential piping segments, which exhibit inside and outside surface geometries one would expect to encounter in large-bore reactor coolant circuit welds. Phased arrays operating at 500 kHz, 750 kHz, and 1.0 MHz were applied from the outside surface to detect the inside surface-breaking cracks. Line scans adjacent to the welds were performed using inspection angles from 30–60°.

Crack detection was made by careful analyses of composite data images acquired from both CCSS and SCSS sides of the weld. The 500-kHz phased array proved to be the better performer, with a combined detection rate of approximately 77% (91% from the SCSS and 63% from the CCSS). The performance of the 750-kHz and 1.0-MHz arrays was significantly affected by the microstructure of the CSS materials, with combined detection rates of around only 50% for each frequency. As expected, thermal fatigue cracks are generally more difficult to detect than mechanical fatigue cracks; this is shown by detection capabilities of the 500-kHz array (the best performer), with 93% of mechanical fatigue cracks being detected versus only 57% of those produced by thermal fatigue.

The CCSS piping presented the more challenging microstructure and resulting varied acoustic properties; consequently, detection performance was lower from this side of the weld. Parent

material microstructure (SCSS versus CCSS) appears to dominate attenuation of the sound beam, as no trend was observed to indicate enhanced detection based on whether the flaws are located on the near- or far-side of the weld.

Length sizing was attempted for all detected cracks. Measurements were made by using standard 6-dB drop and loss-of-signal techniques to ascertain the overall length of these flaws. The results were poorer than expected. Because of beam redirection and partitioning, the length-sizing root mean square error (RMSE) was approximately 24 mm (0.95 in.) for the 500-kHz array. The 1.0-MHz array performed better, with an RMSE of approximately 20 mm (0.79 in.). As evidenced by the RMSE values obtained in this study, the coarse microstructure results in degradation of length-sizing capability for thick-walled CSS piping. The general trend for these low-frequency arrays is to undersize the length of the cracks. This is consistent with results of the corner-trap responses on the unflawed CCSS segments described above, in that portions of the crack response may be significantly diminished over the crack length so that images of the flaws are shorter than actual length. Also, if shallow flaws cannot be reliably detected, and the crack shape tends to be semi-elliptical so that the ends have only limited areas for reflection, the length of the crack will be undersized.

It is concluded that 500-kHz large-aperture phased arrays are capable of detecting ID-connected cracking in heavy-walled CSS piping when inspected from the OD surface of the pipe. The results show that for inside surface-breaking thermal and mechanical fatigue cracks greater than approximately 30% through-wall in depth, the 500-kHz method detected 100% of the flaws, provided that access to the outside surface was sufficient for adequate transducer placement and coupling. Further, cracks on the order of 15–30% through-wall could also be periodically detected with the 500-kHz phased array method. No through-wall sizing of flaws was performed due to an absence of tip-diffracted responses. Length sizing is possible, although the RMSE is slightly higher than currently allowed by Section XI of the ASME Code.

This study shows automated low-frequency phased array technology to be capable of detecting and length-sizing cracks in CSS materials installed in primary coolant piping at nuclear power plants. The demonstrated superiority of this technology over conventional UT methods suggests that low-frequency phased array methods be used to supplant current examination techniques, which typically employ manual 1.0-MHz transducers, for increasing the reliability of weld inspections in these systems. Because of the complexity of data acquisition and analysis methods using phased arrays to detect service-induced cracks on these coarse-grained microstructures, examiners, equipment, and procedures need to demonstrate effective performance—for example, to the criteria specified in the ASME Code Section XI, Appendix VIII—for reliable ISI deployment.

Acknowledgments

The work reported here was sponsored by the U.S. Nuclear Regulatory Commission (NRC) and conducted under NRC Job Code Number Y6604. During the period of this work, two NRC program managers led the effort and provided valuable guidance and technical direction. The Pacific Northwest National Laboratory (PNNL) acknowledges both Deborah Jackson and Wallace Norris for their contributions.

The authors also express their gratitude to Greg Selby at the Electric Power Research Institute NDE Center in Charlotte, North Carolina, for his support through loaned cast stainless steel (CSS) specimens and flexibility in allowing PNNL to extract a specimen of the Spanish spool piece for subsequent polishing and chemical etching. Also we wish to acknowledge Grady Lagleder at IHI Southwest Technologies, Inc., and Dave Kurek at WesDyne International for providing vintage CSS specimens to PNNL for ongoing research in this area.

In addition, PNNL would like to thank Guy Maes at ZETEC, Inc. for modifying a phased array instrument to operate at low frequency and his technical insights on cast material inspections and probe development, and Michel DeLaide at AIB-Vincotte for fabricating and loaning the first-generation 500-kHz phased array probe to PNNL for initial work in this area.

At PNNL, the authors wish to thank Anthony Elliot for his work in creating false-color images and grain size measurements of the CSS microstructures, and Earlene Prickett for her support in finalizing this document. The authors also acknowledge Kay Hass for preparing the final manuscript and Andrea Currie for editing. PNNL is operated by Battelle for the U.S. Department of Energy under Contract DE-AC05-76RL01830.

Abbreviations and Acronyms

ASME	American Society of Mechanical Engineers
CSS	cast stainless steel
CCSS	centrifugally cast stainless steel
DMW	dissimilar metal weld
EPRI	Electric Power Research Institute
FCP	false call probability
ID	inner diameter
IHI-SW	IHI Southwest Technologies, Inc.
ISI	inservice inspection
LOS	loss of signal
LWR	light water reactor
MFC	mechanical fatigue crack
MPATS	multi-parameter analysis tool set
NDE	nondestructive examination
NRC	U.S. Nuclear Regulatory Commission
OD	outer diameter
PA	phased array
PDI	Performance Demonstration Initiative
PISC III	Programme for the Inspection of Steel Components Phase III
PNNL	Pacific Northwest National Laboratory
PODCI	probability of detection and correct interpretation
PWR	pressurized water reactor
RF	radio frequency
RT	radiographic testing
SAFT	Synthetic Aperture Focusing Technique
SCSS	statically cast stainless steel
SNR	signal-to-noise ratio
TFC	thermal fatigue crack
TRL	transmit-receive longitudinal

UT	ultrasonic testing
WOG	Westinghouse Owners Group
WSS	wrought stainless steel

1 Introduction

This report provides a synopsis of the laboratory investigations conducted for the U.S. Nuclear Regulatory Commission (NRC) at the Pacific Northwest National Laboratory (PNNL) to evaluate the effectiveness and determine capabilities of low-frequency ultrasonic methodologies as applied to the inspection of cast stainless steel (CSS) welds in nuclear reactor piping. Progress, recent developments, and results are described from the assessment of low-frequency techniques for the detection of surface-breaking cracks in CSS reactor piping components from the outside surface of the pipe wall.

The overall objective of the research is to determine the effectiveness and reliability of advanced nondestructive examination (NDE) methods on light water reactor components containing cast stainless steel material and other coarse-grained components that encompass dissimilar metal welds, piping with corrosion-resistant cladding, and far-side examinations of austenitic piping welds. The specific goal of this work is to enhance various NDE methods to directly improve our ability to detect, localize, and, if possible, size cracks in coarse-grained steel components.

The most recent advances using state-of-the-art, low-frequency phased array and low-frequency Synthetic Aperture Focusing Technique (SAFT) methods for improving the inspection of CSS components are described in this report. Section 2 provides detailed descriptions of the special challenges posed to NDE inspectors when examining CSS components. Section 2 also presents a historical perspective on efforts to address the challenges associated with CSS component inspections and introduces the notion of phased array methodology. In Section 3, technical descriptions are provided for the ultrasonic transducers used in PNNL's research. Section 4 documents the CSS piping specimens used in the study. The PNNL analysis of inherent ultrasonic noise in heavy-walled centrifugally cast stainless steel piping in non-welded parent material, or baseline material, is detailed in Section 5. Section 6 documents the methodology with which PNNL detected and characterized cracks in flawed specimens. Overall findings are summarized and conclusions are drawn in Section 7, followed by a list of references cited in Section 8. Detailed illustrations of the specimens and inspection results are provided in Appendixes A through C. Appendix A contains photographs of the flawed weld specimens provided by the Westinghouse Owners Group and PNNL. Appendix B provides the corner signal data from phased array and low-frequency/SAFT examinations of CCSS base metal, used to characterize the signal-to-noise ratios obtained with the two technologies. Phased array detection data for the Westinghouse Owners Group and PNNL flawed specimens are presented in Appendix C.

2 Background

This section provides a description of the inspection challenges posed by cast stainless steels and documents efforts to date to meet those challenges. The configuration and capabilities of the low-frequency phased array inspection system used at PNNL also are described.

2.1 Inspection Challenges for Cast Stainless Steels

The relatively low cost and high corrosion resistance of cast stainless steel (CSS) have resulted in extensive use of this material in the primary coolant piping systems of Westinghouse-designed pressurized water reactors (PWRs). Alloying elements and casting processes used in the fabrication of CSS materials are responsible for its corrosion resistance and strength but also create complex and coarse-grained microstructures. Figure 2.1 illustrates the general location of key CSS components in the primary coolant loop of a Westinghouse-designed PWR.

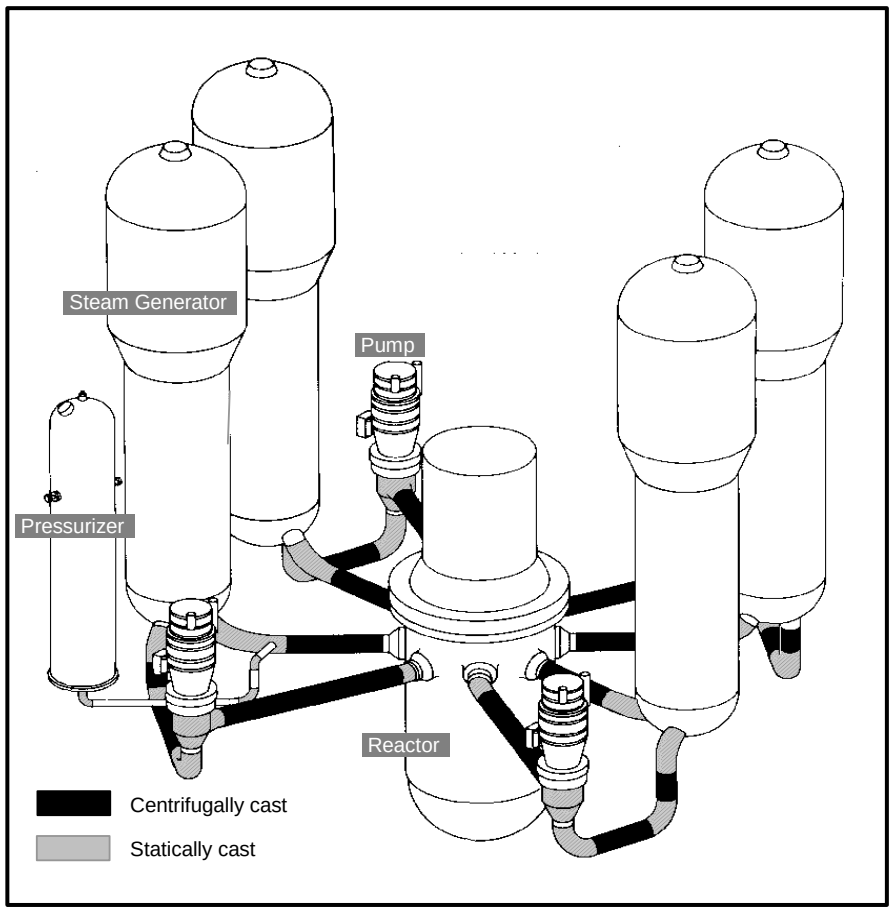

Figure 2.1 Cast Stainless Steel Material in Primary Coolant System for Westinghouse-Designed Pressurized Water Reactor Four-Loop Plant (based on Westinghouse diagrams; illustration courtesy of A. Chockie, Chockie Group International, Inc.)

As part of a defense-in-depth philosophy, inservice inspection (ISI) of welds in the primary coolant circuit of light water reactors (LWRs) is performed to ensure that service-induced degradation does not compromise the structural integrity of safety-related components. As such, CSS piping is subjected to periodic volumetric examination based on requirements found in the American Society of Mechanical Engineers (ASME) Boiler and Pressure Vessel Code, Section XI, Rules for Inservice Inspection of Nuclear Power Plant Components. The ASME Code lists radiographic testing (RT) or ultrasonic testing (UT) as being acceptable nondestructive examination (NDE) methods for implementing volumetric inspections of selected components. For commercial nuclear power plants, component background radiation and access limitations generally prevent the use of radiography. Therefore, UT is the standard NDE method used to inspect cast austenitic welds in LWR primary piping loops. For ISI to be successful, service-induced flaws must be found and repaired prior to becoming of such size that the integrity of a component is challenged. Detection of flaws is the initial priority, and for UT this is accomplished by analyzing ultrasonic echo waveforms from reflections within the volume of inspected material that could potentially be caused by service degradation. Due to the coarse microstructure of CSS material, many inspection problems exist and are common to structures such as statically cast stainless steel (SCSS) elbows, statically cast pump bowls, centrifugally cast stainless steel (CCSS) piping, dissimilar metal welds (DMWs), and weld-overlay-repaired pipe joints. Far-side UT of stainless steel welds (i.e., attempting to detect flaws on the opposite side of welds) also encounters these inspection problems because the ultrasonic field must pass through the coarse-grained, anisotropic weld material.

Because Westinghouse Electric Corporation used CCSS piping in primary reactor coolant loops of 27 PWRs in the United States (Diaz et al. 1998), and thermal aging, or embrittlement, in cast piping is possible, development of effective and reliable inspection techniques for these important safety-related components is mandatory for long-term operation. In addition, there are many pipe-to-component weld configurations where inspection from the component side of the weld is not possible due to the geometry. When risk-informed principles are applied, some of these welds have been classified as high safety significant. Thus to inspect these welds, the examination must be performed from the cast piping side. The general microstructural classifications for CCSS are columnar, equiaxed, and a mixed and layered columnar-equiaxed condition of which the majority of field material is believed to be the latter. Figures 2.2 and 2.3 illustrate the general classes of microstructures and the diverse variations in grain orientations, mixing, and layering.

Centrifugally cast stainless steel is an anisotropic and inhomogeneous material. The manufacturing process can result in the formation of long columnar (dendritic) grain structures (approximately normal to the surface), with grain growth oriented along the direction of heat dissipation, often several centimeters in length. Additionally, during the cooling and solidification process, columnar, equiaxed (randomly speckled microstructure), or a mixed structure can result, depending on chemical content, control of the cooling, and other variables in the casting process. The outer-diameter (OD) and inner-diameter (ID) surfaces of specimens used in the current study possess relatively smooth, machined conditions; this is a normal part of the fabrication method, performed to remove imperfections resulting from the casting process.

The large size of the anisotropic grains, relative to the acoustic pulse wavelength, strongly affects the propagation of ultrasound by causing severe attenuation, changes in velocity, and scattering of ultrasonic energy. Refraction and reflection of the sound beam occur at the grain boundaries, resulting in defects being incorrectly reported, specific volumes of material not being examined, or both. When coherent reflection and scattering of the sound beam effectively occur at grain boundaries, ultrasonic indications that are difficult to distinguish from signals originating from flaws may be produced. When piping components are inspected from the outside surface, where the returning signal-to-noise ratio (SNR) is relatively low, ultrasonic examination can be confusing, unpredictable, and unreliable (Taylor 1984). To reduce the impact of the microstructure on the inspection technique, the work reported here focuses on low-frequency (400 kHz to 1.0 MHz) ultrasonic energy propagation through the material as applied from the OD surface.

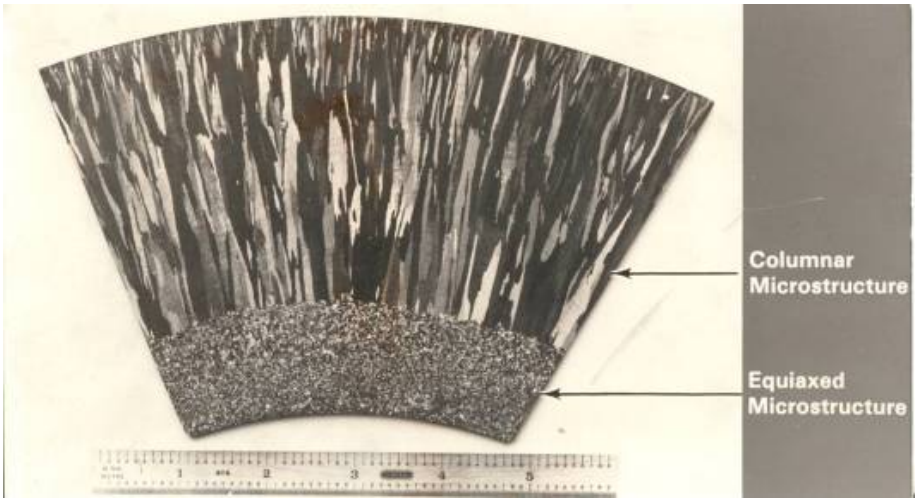

Figure 2.2 Specially Fabricated Sample Illustrating Both Columnar (Dendritic) and Equiaxed Microstructures in Centrifugally Cast Stainless Steel

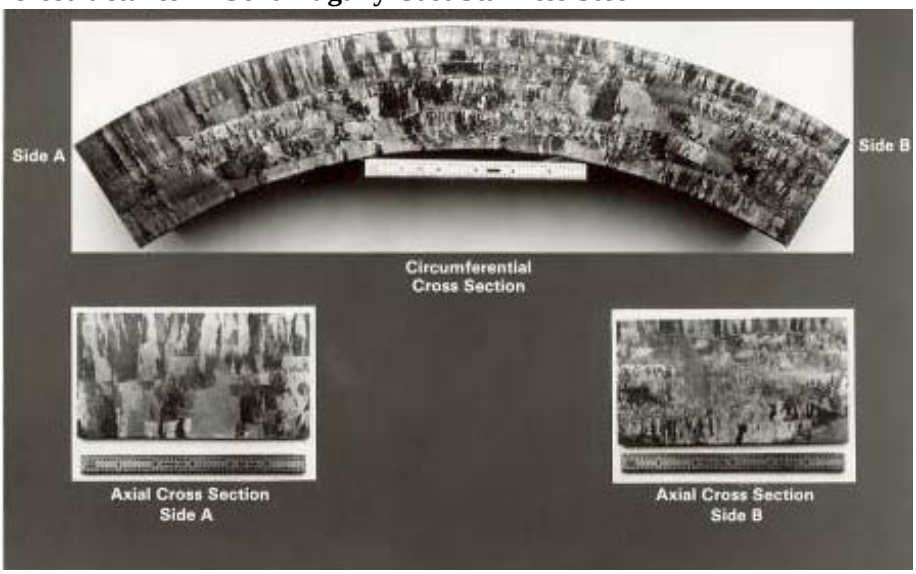

Figure 2.3 Circumferential and Axial Cross Sections of a Centrifugally Cast Stainless Steel Pipe Section Provided by Southwest Research Institute

2.2 A Historical Perspective – Efforts to Address Cast Stainless Steel Inspection Problems

Inservice inspection using ultrasonic testing for NDE of nuclear reactor piping and pressure vessels requires reliable detection and accurate sizing methodologies for material degradation. In cast stainless steel materials, the first challenge is to reliably and consistently detect defects and then to obtain enough data to accurately size these defects. In 1978, a multiyear program, "The Evaluation and Improvement of NDE Reliability for Inservice Inspection of Light Water Reactors" (NDE Reliability), was established at PNNL to assess the capability of current ISI techniques and develop recommendations that would ensure a suitably high inspection reliability if needed. Work on this program began to shed light on the complexity of addressing inspectability of coarse-grained materials. This NRC-sponsored work has continued under a program titled "Assessment of the Reliability of UT and Improved Programs for ISI."

The initial work on CCSS began with parametric studies looking at a host of UT equipment parameters, flaw characteristics (size, location, orientation, and type), and materials used in the primary circuit of light water reactors (Becker et al. 1981). These parametric studies evaluated various cracking processes, with the majority of the effort on mechanical fatigue cracking and thermal fatigue cracking. The UT response from thermal fatigue cracks was much less than that from mechanical fatigue cracks as a result of the large residual compressive stresses remaining after the cracks were produced. The thermal fatigue process was used to grow cracks in CCSS material for use in a round-robin study conducted by PNNL. This study was called the Piping Inspection Round Robin (PIRR) and was conducted in the early 1980s (Heasler and Doctor 1996). One of the important conclusions of the PIRR was that CCSS material was being inspected very ineffectively with the UT technology that was available at that time and in meeting the requirements in Section XI of the ASME Boiler and Pressure Vessel Code.

This work was followed by studies on CSS materials that included a joint PNNL and Westinghouse cooperative program (Taylor 1984) that focused on developing an understanding of the microstructural effects on ultrasonic propagation through limited round–robin trials and characterization of acoustic velocity variations in these materials. This work helped to generate interest across the international NDE community, and in 1985 the Programme for the Inspection of Steel Components (PISC III) initiated an international round-robin test to assess the effectiveness of state-of-the-art ultrasonic testing of CSS materials (Bates et al. 1987). PNNL coordinated the round-robin tests in the United States for the NRC. Eighteen inspection teams participated in this round robin, and a variety of procedures were employed, including manual UT, automated UT, automated UT coupled with advanced signal processing methodologies, and non–UT-based techniques. The most common technique at that time employed a dual probe using longitudinal (compressional) waves at 1.0 MHz. The intent of this effort was to identify the most promising ISI procedures and to provide a foundation for more in-depth studies. Blank samples were included in the suite of specimens to provide estimates of the false call probability (misclassifying blank material as cracked). Cracks were placed at various circumferential locations so that no one region could be considered more likely to contain cracks. Results from this round robin indicated that the NDE techniques current at that time could not effectively discriminate between the coherent scattered energy from thermal fatigue cracks and that from uncracked CSS material.

One major problem identified as affecting the development of improved ISI procedures was the incomplete characterization of CSS microstructures. During the 1980s, the direction of work performed at PNNL included metallurgical characterization of these materials to identify the various microstructures that could exist in the field. From this early work, the program at PNNL partially focused on specifically classifying CSS microstructures. The concept behind this is that once the specific grain structure of the material was identified, the ultrasonic system could be optimized for the grain structure under test (Jeong 1987, p. 167). The purpose of optimizing the ultrasonic system was to achieve a high signal-to-noise ratio so that subsequent defect detection, classification, and sizing could be carried out more reliably. Most difficulties in testing CCSS come from the compound effects of coarse grains, their distribution patterns, and associated anisotropy. For this reason, parameters such as ultrasonic wave mode, probe frequency and type (dual- versus single-element, broadband versus narrowband, focused versus nonfocused), and pulser/receiver type need to be optimized for achieving an effective inspection.

Also during this period, studies were conducted at PNNL to evaluate the utility of advanced signal processing methods—in particular, the synthetic aperture focusing technique (SAFT). In tandem with the study of SAFT, low-frequency (500-kHz) shear-wave propagation was evaluated to determine if relevant information could be extracted from the frequency domain of UT signals as a function of reflector geometry, orientation, and microstructure. Ultrasonic data were compiled from zones of CSS material containing defects and defect-free areas, and the data were transformed into the frequency domain where the results were summed and sorted into classes of equiaxed, columnar, high-probability detections and low-probability detections. The conclusions from this work indicated that detection of a defect was most likely based upon signal amplitude and that no simple filter existed for both columnar and equiaxed microstructures for rejection of unwanted coherent grain scattered signals. Thus, the problem was not based solely upon signal-to-noise because the frequency response data from both defects and noise were found to be quite similar.

During the late 1980s and early 1990s, work at PNNL focused on evaluating and quantifying sound field coherence and distortion in CSS microstructures. This work led to a better understanding of what happens to the sound field as it travels through these coarse-grained materials. Ultrasonic beam profiles (sound field maps) as a function of wave mode, probe frequency, incident angle, microstructure, and other pertinent inspection parameters were acquired and evaluated. Other efforts included phase imaging of the far-side (back surface) echoes (Good et al. 1990) and imaging of the subsurface microstructure using leaky Rayleigh-waves to aid in classification and mapping of the microstructure's texture.[(1)] In conjunction with this, work continued on measuring the acoustic velocity and attenuation characteristics of these microstructures in CSS materials (Good 1991). These studies provided a technical basis for understanding sound field propagation as a function of inspection parameters in CSS and showed that for purely columnar and purely equiaxed microstructures, there was a high degree of spatial coherence to the sound field but spatial coherence for mixed-banded microstructures degraded significantly. Finally, the use of microstructural classification information and texture maps appeared to provide some useful information that could be employed to further optimize

---

([1]) Hildebrand BP, MS Good, and AA Diaz. *Ultrasonic Classification of Centrifugally Cast Stainless Steel Utilizing the Rayleigh Critical Angle Technique*. 1991 Technical Letter Report from PNNL to the NRC.

inspection parameters for improved UT of CSS. However, the ability to classify and characterize specific macrostructures did not directly alleviate the problem of ineffective and unreliable UT inspections of coarse-grained materials.

NRC guidance in the early to mid-1990s was to shift to a more direct approach and focus on developing, investigating, and testing new and advanced inspection methodologies that are inherently less sensitive to the effects of CSS microstructures. This guidance included the use of fracture mechanics calculations to help quantify realistic flaw sizes that start to challenge the structural integrity of CSS components under various service conditions and to couple this data with the most promising inspection techniques and determine the smallest flaw dimensions that could be reliably detected. It was during this period that PNNL developed a low-frequency ultrasonic method coupled with the SAFT for improved penetration and detection of cracks in CSS materials. At this same time, evaluations were conducted to study other advanced processing techniques taken from the field of optics including phase aberration correction and time reversal mirroring techniques. This effort included PNNL's participation in a limited round robin sponsored by the Electric Power Research Institute Nondestructive Examination Center (EPRI NDE Center), Yankee Atomic Electric Company, and Northeast Utilities in 1993. Thirteen teams participated in this round-robin test, which included six manual UT techniques and seven automated UT techniques. The initial application of PNNL's low-frequency/SAFT inspection method resulted in the round robin's best performance for an automated system, with a 70% probability of detection and correct interpretation (PODCI) versus a 30% false call probability (FCP) (Diaz et al. 1998).

Throughout the mid to latter 1990s, ongoing work at PNNL continued to focus on evolving the low-frequency/SAFT technique. These efforts included a field exercise at Seabrook Station Unit 2, where PNNL researchers and NRC Region 1 inspectors conducted data acquisition and exercises to assess current industry standard inspections and compare the performance (inspection results) against the low-frequency/SAFT methodology. Laboratory-based development continued as well with evaluations of the PISC and PNNL CSS specimen set. A subsequent field exercise, held at the EPRI NDE Center for evaluation of some of the Westinghouse Owners Group (WOG) CSS and dissimilar metal weld (DMW) specimens, was conducted in 1997. The results of these activities provided promising insights toward the development and eventual evolution of this technique that included crack identification criteria based upon analysis of redundant reflections as a function of various inspection parameters. Work between 1998 and 2003 focused on transducer modifications and performance enhancements, optimization of the inspection system electronics, evaluation of post-processing algorithms (wavelet processing and maximum entropy processing) for noise/clutter reduction, and enhancements to the functionality of the SAFT analysis software.

The low-frequency/SAFT inspection methodology employs a zone-focused, low-frequency (250- to 450-kHz) inspection protocol coupled with the synthetic aperture focusing technique. This technical approach is based upon the premise that sufficient differences exist between the characteristics of coherently scattered ultrasonic energy from grain boundaries and geometrical reflectors versus the scattered ultrasonic energy from surface-breaking thermal and mechanical fatigue cracks in coarse-grained steels. PNNL's empirical approach relies on the notion that acoustic impedance variations at the grain boundaries can be minimized by using lower

frequencies (longer wavelengths), and the degree of coherent energy scattered from these grain boundaries should be inconsistent as a function of frequency, insonification angle, scan direction, and the amplitude of returning signals. The low-frequency/SAFT approach is directed toward detecting specular responses from the surface-breaking crack as a function of time, spatial position, and amplitude. If the frequency is low enough, the examination is less sensitive to the effects of the microstructure and the probability of detection increases for these cracks. The tradeoff is resolution in that small flaws (≤ 20% through-wall) may not be consistently detected due to the longer wavelengths of ultrasound being employed. However, with the addition of SAFT signal processing, the examination can be performed at low frequencies while maintaining the capability to detect cracks approximately 35% deep or greater in typical CSS and DMW piping components that are 62–75 mm (2.44–2.95 in.) in thickness. In fact, for later vintage CSS piping which possesses more homogeneous microstructures, it is expected that cracks smaller than 35% through-wall may also be reliably detected. Therefore, by employing multiple examination frequencies and incident angles and inspecting from both sides of a weld, the low-frequency/SAFT methodology uses a multiparameter approach for detection, localization, and sizing of cracks in CSS and DMW material.

The examination process is further enhanced by the addition of a low-frequency, variable-angle, high-bandwidth search unit that enables the inspector to compensate for acoustic velocity variations due to the microstructure by selecting the optimal incident angle in the material under test. The high bandwidth allows the inspector to use a wide range of examination frequencies centered at 350 kHz. The zone-focal characteristics of the dual element search unit provide optimal insonification of the inner surface (ID) over a specified range of incident angles.

Nondestructive examination studies conducted in the 1970s and 1980s showed that conventional ultrasonic inspection methods using frequencies in the range of 1.0 MHz to 2.25 MHz, and primarily the shear-wave modality, were not effective at inspecting CSS materials. The work PNNL has conducted over the years indicates that lower frequencies outside the conventional UT frequency range, equating to longer wavelengths, result in less sensitivity to the effects of the microstructure, and provide better penetration for thick-section CSS components. This work also shows that use of longitudinal waves, isolation of the transmission and reception pathways of the transducer (by employing dual elements in a pitch-catch inspection technique), and incorporating data from multiple inspection angles (0º to 70º) and both sides of the weldment significantly increases the ability to detect and discriminate reflectors in CSS material.

While promising results had been achieved with this technique, some challenges needed to be addressed. The low-frequency/SAFT methodology is a time-intensive approach that requires acquisition and analysis of multiple raster scans over a range of specific incident angles, both near- and far-side orientations, and at multiple frequencies, typically 250 kHz, 350 kHz, and 450 kHz. In 2002 and 2003, PNNL addressed the issue of data fusion and composite data analysis techniques to be employed with the low-frequency/ SAFT methodology.

Although laboratory and field trials have provided promising results with regard to localization and detection capabilities in CSS materials, the procedures required for effective analysis of the low-frequency/SAFT data were very time-consuming and labor-intensive. The inspection procedures resulted in the acquisition of multiple ultrasonic data sets as a function of inspection

angle, examination frequency, and the scan direction relative to the weld. The large volume of data was difficult to manage and challenging to analyze, as the various steps required to process the data files, study the ultrasonic responses, and determine the comprehensive meaning between the various data sets were very challenging. Hence there was a need to develop and test a set of software tools for effective data fusion and improved analytical capabilities that reduced the time for analysis, improved consistency of the process, and enhanced the ability to discriminate between ultrasonic responses from material structure (e.g., grain boundaries) and cracks.

In general, the data analysis protocol employed multiple data sets for crack identification, localization, and sizing. The analysis technique was based upon redundancy of the ultrasonic indications as a function of the various inspection parameters. Scans were performed at various angles and frequencies and, when possible, from both sides of the weld. Data sets were then post-processed using the SAFT. The SAFT-processed data sets were then properly projected, and the resultant full-volume focused image provided a visual platform for ultrasonic characterization or mapping of the inspected area.

Prior to this, each scan was separately analyzed for indications. Each indication was given a start and stop pair of *x, y* coordinates related to OD positional data on the component under test. These coordinates were manually entered into an Excel® spreadsheet. The different scans were placed in different columns so that Excel could automatically assign colors and symbols to the respective data sets (scans). The multiple indications from these data sets (scans) were then manually superimposed (essentially overlaid) on top of one another in Excel, and the plots were examined visually to determine what indications appeared to recur most often, which (if any) were geometrical features, and which seemed to be attributed to grain noise or other irrelevant indications, based upon a well-defined set of criteria. The most likely cluster (using elementary positional averaging and redundancy) was used to determine the crack location. In some cases, an arithmetic average of the endpoints and distance from the weld centerline were used. In other cases, a visual estimate was used; this had the advantage of allowing the inspector to assign (implicit) weights to the data sets. Finally, a single composite data set was formulated from the data acquired from the multiple scans, and a call was made on the component under examination.

The effort conducted in 2003 focused on implementing a semi-automated analysis method for combining these data sets in a reliable and consistent fashion. The new software and interactive toolset provided a means for more effectively combining data sets taken at multiple angles and frequencies and was called a multi-parameter analysis tool set (MPATS). The interactive toolset addressed the difficult challenges of proper registration between multiple independent UT data sets. The previous data fusion analysis process was too time-intensive and required automation to provide an analysis that is reliable, less time-consuming, and easier to use. Issues of accurate registration (positional) between data sets, overlaying and fusion of multiple data sets, and interactive application of specific crack identification and sizing criteria were also addressed in this effort.

As this effort continued, the concept of combining low-frequency ultrasonic energy with multi-angle scanning and multi-side access became more achievable with the advent of phased array ultrasonic technologies. It is now possible to rapidly acquire data using state-of-the-art beam-focusing and beam-steering algorithms that provide high-resolution images at frequencies as low

as 500 kHz. In 2003, the NRC funded PNNL to evaluate and assess advanced NDE methodologies for far-side inspection of wrought stainless steel piping with austenitic welds. This study employed both the low-frequency/SAFT and phased array technologies in a comparative assessment of detection performance.[2] From this work and subsequent work that has included the use of low-frequency phased array methods for CSS materials, the low-frequency/SAFT methodology has given way to the improved performance of the phased array approach using 500-kHz refracted longitudinal waves.

Using a phased array method operating at low frequencies is a relatively new concept and was the product of brainstorming sessions between PNNL, and vendor representatives from ZETEC, Inc. (phased array equipment manufacturer) and AIB-Vincotte (array design and manufacturer). This approach makes use of PNNL's experience with low-frequency UT that has been evolving over the last decade, and couples state-of-the-art phased array technology with new array manufacturing methods.

For nearly 30 years, PNNL has taken a systematic approach toward addressing the CSS inspection problem, by assessing current inspection capabilities; involving utilities, vendors, regulatory agencies, and the international community; improving our understanding of the fundamental physics of UT in CSS materials; and improving detection and sizing techniques that lead to the development of novel, more effective, and reliable inspection capabilities for anisotropic, inhomogeneous coarse-grained steel components.[3]

2.3 Current Approach Using Low-Frequency Phased Array Methods

As stated in Section 2.2, low-frequency/SAFT methods show promise in detecting larger (approximately >35% through-wall) cracks in CCSS piping welds. The work indicates that at longer wavelengths, certain angles of propagation may be able to coherently penetrate regions of varied grain structures in these materials. In other words, it may be possible to examine CCSS welds using long compressional waves oriented at the proper angles with respect to the large grains that may be encountered. Unfortunately, there is no existing method to determine grain sizes or orientations of this material in situ. In addition, metallographic images (see Figures 2.2 and 2.3) show that grain size, orientation, and layering may vary as a function of circumferential location on the same piece of vintage CCSS piping, so it may not be feasible to choose a single optimum angle for ultrasonic propagation with respect to grain orientation. For these reasons, low-frequency/SAFT requires multiple angles of interrogation performed from both sides of the weld to account for unknown grain structures. Results from these multiple data sets may then be integrated to distinguish between signal responses from grain boundaries and those from targeted flaws. The process can result in several hours to inspect a single weld, which for most commercial nuclear power plants is not desirable due to high radiation fields that could be encountered and the short critical path times available for ISI during refueling outages.

([2]) Anderson, Diaz, Cumblidge, Doctor, Judd, Morra, and Hixon. Unpublished. *Capabilities of Ultrasonic Techniques for the Far-Side Examinations of Austenitic Stainless Steel Piping Welds.* Draft submitted to the NRC for review.

([3]) Diaz, Mathews, Hixon, and Doctor. Unpublished. *Assessment of Eddy Current Testing for the Detection of Cracks in Cast Stainless Steel Reactor Piping Components.* Under review by the NRC.

To benefit from previous work using low frequencies and to extend the capability to propagate sound through multiple angles while minimizing inspection and analysis time, PNNL, with assistance from phased array vendors, pursued a low-frequency phased array approach. The basic premise for all phased array (PA) transducers involves a set of small, individual piezoelectric elements that are independently driven. Although these elements may be pulsed individually, or in groups, to simulate conventional transducer excitation, the real strength of this technique lies in the capability of the system to electronically delay signals to and from each of these piezoelectric elements during both generation and reception of ultrasonic sound fields. The wave-fronts produced by subsets of elements interfere within the inspected component to produce a resultant, phase-integrated ultrasonic wave. This is commonly referred to as *beam forming* (see Figure 2.4).

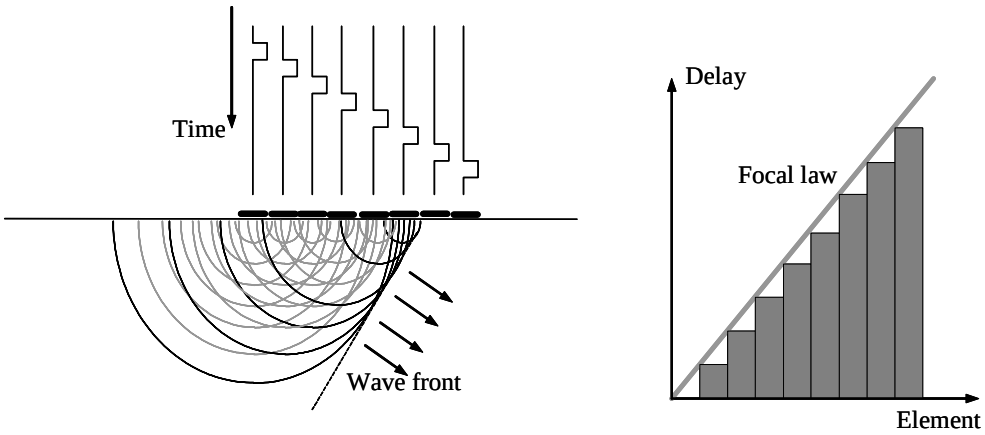

Figure 2.4 Beam Forming Using a Phased Array (courtesy R/D Tech, Inc.)

The PA system can therefore steer and focus the integrated ultrasonic beam within the component. The geometrical design of a PA transducer is typically a function of specific implementation variables—that is, geometries such as linear, annular, circular, or matrix designs are developed to address specific ultrasonic application needs (Poguet et al. 2001). For example, depending on the array design and the component thickness, a one-dimensional linear array, with major axis oriented normal to a pipe weld, may interrogate close to an entire planar cross section of the weld by sweeping through a series of inspection angles without having to mechanically move the transducer toward or away from the weld. Therefore, in theory, an entire pipe weld can be examined with a single circumferential scan motion along the weld. Because of the variations of images that can be produced, a systematic method should be employed when performing analyses of phased array data by using a standardized procedure (Anderson et al. 2003).

The phased array system at PNNL consists of a Tomoscan III 32-channel instrument produced by ZETEC, Inc. (formerly R/D Tech, Inc.). This is a standard piece of equipment used for PA applications in several industrial sectors. This type of system is used by General Electric to inspect reactor internals and at the Electric Power Research Institute (EPRI) NDE Center for a variety of applications, including far-side inspection procedure development and initial true-state characterization of the industry's Performance Demonstration Initiative (PDI) specimens. The instrument can be programmed (by development of focal laws in software) to control up to 32 channels for transmission and reception of ultrasonic signals. It has 12-bit logic and operates

through a local Ethernet connection to a standard desktop computer. Figure 2.5 shows the PNNL phased array system. It should be noted that for operation at 500 kHz, an internal board in the system would have to be modified; for the work described in this report, PNNL chose to rent a similar Tomoscan III instrument modified to operate in this lower frequency range.

The arrays used for the current work were designed similar to conventional transmit-receive longitudinal (TRL) transducers in that discrete portions of the search unit are used for transmitting the longitudinal wave ultrasound and other portions are used only for reception. Although housed as a unit, transmit and receive sections are mounted on an integral wedge and acoustically separated. Design specifications and theoretical sound fields produced by these arrays are further described in Section 3 of this report. The design of these arrays is consistent with conventional mono-element transducers being used throughout

Figure 2.5 Typical Phased Array System Components

industry for inspecting austenitic and dissimilar metal welds. The primary difference is that matrices of individually-controlled elements are used as opposed to a single piezoelectric crystal and, of course, the elements are made to operate at 500 kHz. Therefore, instead of being able to generate only a single angle of sound within the component, the arrays allow steering sound beams through multiple angles in near real time. In addition, focusing of sound at the proper depths within the material can also be accomplished with the array. This means that a single line scan adjacent to the weld can be made while data are being collected for many angles simultaneously. This is the equivalent of performing multiple scans at many angles with a conventional transducer and enables production of detailed UT images with only a single pass from the array along each weld. Given appropriate acquisition and digitization rates, line scan times are very fast, up to approximately 50 mm/sec (2 in./sec), and control software allows angles of transmitted sound to be performed in segments of degrees. The result is that instead of conventional raster scanning that requires several hours to complete for a large-diameter piping

weld, the phased array method can be accomplished in a fraction of this time—only a few minutes are required for scanning an entire piping weld, thus reducing ISI outage time and decreasing the amount of absorbed radiation dose.

Of primary importance for this study is that the PA method allows for multiple angles of inspection; which assumes that certain angles may propagate better within the coarse grain structure. Therefore, this method increases the probability that an optimum inspection angle will be applied, even if the grain structure changes as a function of circumferential piping position. PNNL chose to set line scan speeds at approximately 25 mm/sec (1 in./sec), and to make several scan passes at varied distances from the weld centerline to augment the data for this research. The longitudinal waves were steered through an angular range of 30-60°, at 1° increments through the weld and adjacent base material volume.

One of the advantages of automated PA is that all data are stored digitally during each scan, allowing off-line processing and interpretation to be performed in an environment better suited for analysis than one usually encounters during data acquisition. Several image channels of the data can be displayed, based on the preference of the analyst. The volume corrected B-, C-, and S-scan images, along with supplemental A-scans, were used to assist our understanding of the data.

For the TomoView® and UltraVision® PA software used during these trials, the B-scan image is a projection of the sound field through the component, oriented as if looking along the direction of sound propagation, displaying a circumferential cross section of the weld (shown in the right pane of the analysis screen in Figure 2.6). The S-scan (shown in the upper left pane of the analysis screen), or sector view, provides a projection of the sound fields (from initial to final angle being used, i.e., 30° to 60° for the TRL arrays). The black line in the S-scan shows which angle is currently selected. Finally, the A-scan (lower left pane of analysis screen) represents the electronic responses for reflectors based on x-y axes of time and amplitude, respectively. A typical composite analysis screen showing the scan images described above is included as Figure 2.6.

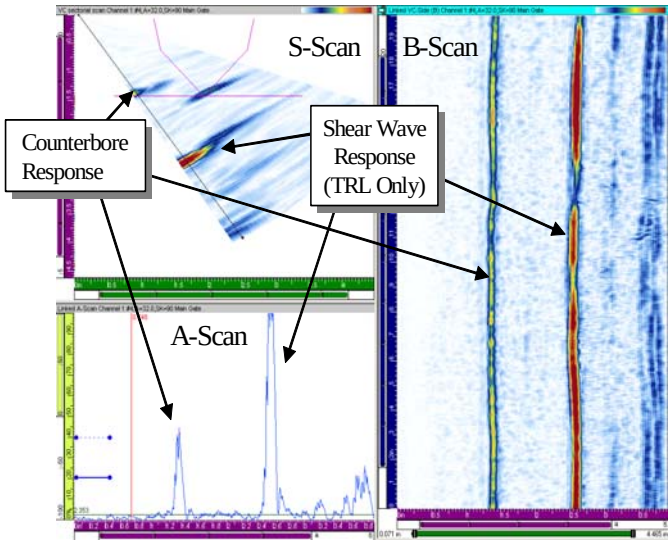

Figure 2.6 Typical Analysis Images Used for Phased Array Inspection

Each of the B- and S-scan images contains all data in the linear scan. Measurement, gating, and sound field cursors are used to provide slices of material to view along the projected sound beam, and discrete beam angle responses are shown in the A-scan. By manipulating these cursors, the analyst is able to walk through cross sections of the material along each linear scan. Because the images in Figure 2.6 were made using a longitudinal wave array, a mode-converted shear wave response is also detected. Images in the A-, B-, and S-scans appearing farther in time (beyond the ID surface) are the result of mode-converted shear waves produced when longitudinal waves strike the inner surface or other reflectors in the component.

An important analysis tool of the phased array system is the ability to examine each angle individually. This allows the investigator to view the different response images in a given scan and discriminate between the various features in a specimen. In Figure 2.6, the system is displaying the results for an inspection angle of 35°, which shows reflections from the counterbore of a pipe. When a higher angle is displayed, shown by 53° in Figure 2.7, other features such as weld root become visible, and for this example, when one displays 65° data (Figure 2.8), targeted flaws become visible. This angular

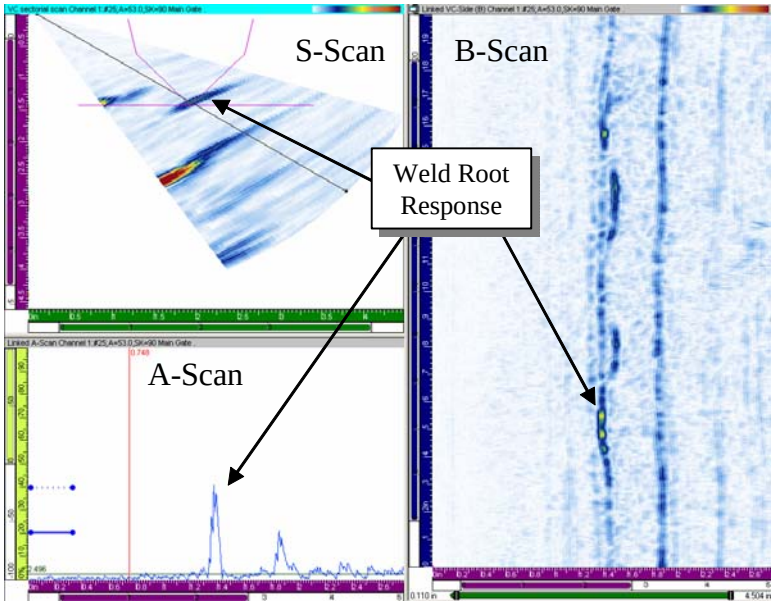

Figure 2.7 Typical Analysis Screen with Mid-Range Angle (53°) Selected, Showing Weld Root with TRL Array

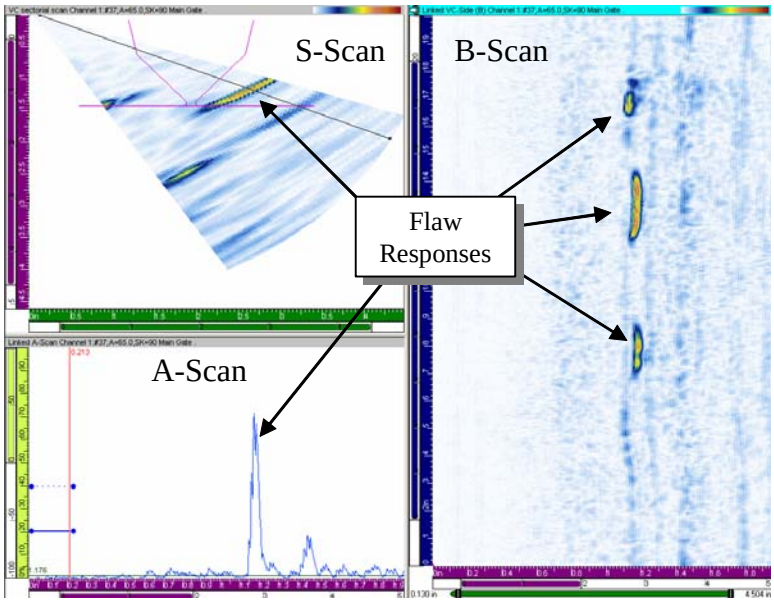

Figure 2.8 Typical Analysis Screen with High Angle (65°) Selected, Showing Flaws with TRL Array

discrimination is a very useful tool when linked with A-, B-, and C-scans. Using the location of geometrical responses from ID counterbore and weld root (if these exist), one can ensure that the sound is penetrating to the ID surface, and these aid in locating flaw responses in coarse-grained materials.

Post-acquisition images afforded by phased array analysis software provide fundamentally important capabilities for discrimination of responses in the coarse-grained materials studied in this research. Only through automated scanning and storing of data during acquisition can one realize the power of the images produced via off-line analyses. Consequently, it is believed that manual techniques using real-time analysis methods would not reliably detect service-induced flaws in CSS piping.

The images presented in Figures 2.6 through 2.8 are shown to provide the reader with the general concept of how phased array data analyses may be performed. Typical data sets from wrought stainless steel piping welds are presented in these images for ease of discrimination between geometrical, metallurgical, and flaw responses. However, data on the CSS materials is much more challenging due to the nature of the grain structure and the need to use a low frequency for ultrasound penetration. The image in Figure 2.9 shows actual phased array data acquired during this CSS research.

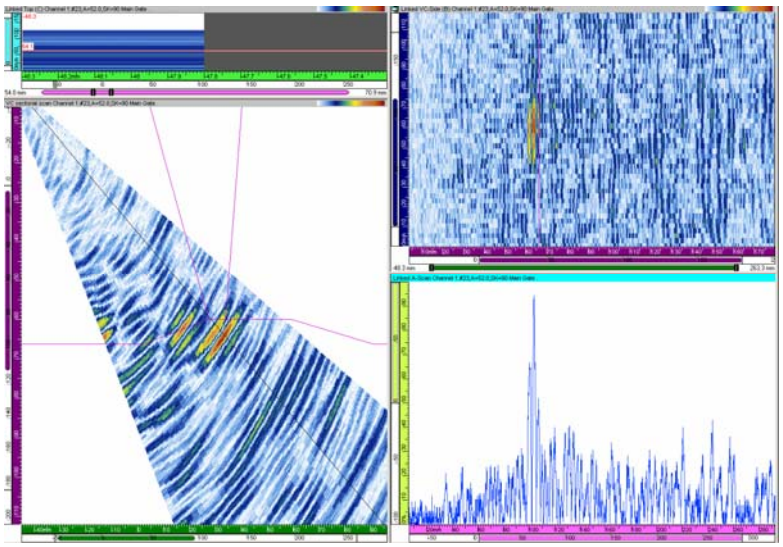

Figure 2.9 Low-Frequency (500-kHz) Data Acquired from CCSS Side of Specimen in Current Study

It is important to note the high level of overall background material noise exhibited in the images and the lower S/N ratio that one might expect from a flaw in CCSS welds. However, the concept of using reference and angle cursers to walk through the data is the same for this material, and geometrical benchmarks such as ID counterbore are useful in verifying location and sound penetration. Inherent noise due to CSS grain structure simply makes the analytical process more challenging. The flaw depicted in Figure 2.9 is an approximately 18% through-wall ID-connected mechanical fatigue crack located on the opposite side of the weld. The 500-kHz sound field is originating from the OD surface on the CCSS side.

3 Ultrasonic Transducers Employed for this Research

Technical descriptions are provided in this section for the ultrasonic transducers used in the PNNL research.

3.1 Phased Arrays

The initial low-frequency PA work was performed with a first-generation, or prototype, transducer developed by Michel DeLaide at AIB-Vincotte in Belgium. Mr. DeLaide designed and constructed the prototype with piezo-ceramic elements, as these were the only low-frequency materials available in late 2003.

Photographs of the first-generation 500-kHz array are shown as Figure 3.1. As can be seen, the prototype has a very large footprint because of the active aperture length needed for sound field focusing, the radiating area of each element required for beam steering in the 500-kHz domain, and an integral wedge to enable steered beams up to 70° in stainless steel. The plastic housing and insulating materials also contributed to this large overall footprint. The specifications for this array are shown in Table 3.1.

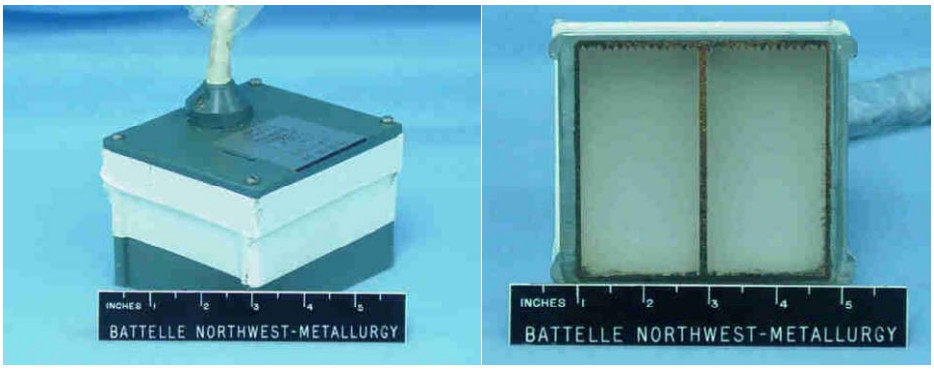

a) side view b) array interface footprint

Figure 3.1 500-kHz Prototype Phased Array

Table 3.1 Specifications of the Prototype 500-kHz Phased Array

Material	Piezoelectric
Configuration	2 × (2 × 10)
Element length	8.44 mm (0.33 in.)
Element width	21.2 mm (0.83 in.)
Active aperture	84 mm (3.31 in.)
Passive aperture	42 mm (1.65 in.)
Total footprint (includes housing)	115 mm × 115 mm (4.5 in. × 4.5 in.)

The preliminary results obtained in 2005 with this prototype design were encouraging in that many of the mechanical and thermal fatigue cracks in the WOG and PNNL CSS specimens (see Section 4 of this report for a full description of the materials) were detected easily; 7 of 11 cracks (64% of all cracks examined) were detectable through centrifugally cast material. Several WOG specimens have OD surface features, such as tapers, base-to-weld metal transitions, and short axial surface regions, which severely limit access to perform proper scanning, especially for the low-angle beams. Due to the large (116-mm-square) footprint of the probe in combination with the surface features of the WOG specimens, the array could not be located near enough to the weld on some specimens to be in an optimum position to acquire data through the entire range of steered beams (30-70°). This resulted in responses with reduced signal-to-noise ratios, often on the order of around 2:1 or less, and made flaw detection more problematic. In fact, 3 of the 15 WOG specimens could not be scanned due to the large footprint of the prototype probe. In addition, the piezo-ceramic elements produced a narrower bandwidth than current piezo-composite elements and required high gain settings for sound generation, which effectively lowers the dynamic range of the system.

However, much was learned from the use of the first-generation PA probe. For example, it was noted that in cast materials, use of lower angles (30-50°) provided better flaw responses in most specimens. Therefore, the footprint of the array would need to be minimized for use on challenging OD surface geometries to allow the active array to be placed closer to the weld/flawed region. Also, the first-generation probe geometry was designed with a limited matrix of elements and a transmit-to-receive crossover point that was too shallow for very small flaws, although this probe feature actually enhanced responses from flaws on the order of 30% through-wall and greater. Because specular reflections from the flaw face dominate the responses detected in this material, a probe that can focus at varied depths would be more effective in detecting flaws. PNNL noted that most of the flaws, especially those made by thermal fatigue, exhibited significant branching, or portions of the flaw face were oriented at oblique angles to the sound field. Thus the ability to detect flaws may be improved with an array that can not only steer the beam but skew the beam in the passive direction. Finally, it was felt that by using piezo-composite elements, one could increase frequency response via a broader bandwidth and improve dynamic range, as they require less excitation energy (instrument gain) to produce comparable sound fields as compared to conventional piezo-ceramics. This would increase the dynamic range of the system and provide better images for data analysts. The insights gained by using the first-generation array were used to design an improved 500-kHz array.

The 500-kHz probes have large footprints to produce focused sound fields in the area of interest. The use of higher-frequency probes allows PNNL to explore array performance for detecting flaws with a decreased wavelength of the ultrasound. Also, the higher-frequency probes are much smaller than the 500-kHz probes, allowing for greater access to the welded region of the samples. The longer the wavelength, the easier the sound can propagate through the large grains. However, at the same time, larger wavelengths have a lower resolution than short wavelengths. The higher-frequency phased arrays used include probes with a 1.0-MHz, 2 × 11 matrix and a 750-kHz, 2 × 11 matrix. The 750-kHz array was built originally to be a 1.0-MHz probe, but when tested it showed a center frequency of 750-780 kHz. The 750-kHz probe has a total bandwidth of 58.8%, while the 1.0-MHz probe has a total bandwidth of 88.4%. The improved

500-kHz probe has a bandwidth of 50%. In all cases, the probes were pulsed with a square wave of approximately 500 nanoseconds, which is the proper pulse width for a 1.0-MHz probe and the longest pulse duration allowed by the phased array system employed. This means that the full bandwidth of the 500-kHz and 750-kHz arrays could not be attained.
The specifications for the 1.0-MHz, the 750-kHz, and the improved 500-kHz array probes are shown in Table 3.2. The improved 500-kHz array is shown in Figure 3.2.

Table 3.2 Specifications of the Phased Array Probes Used in this Study

	1.0-MHz	**750-kHz**	**500-kHz Improved Design**
Material	Piezocomposite	Piezocomposite	Piezocomposite
Configuration	2 × (2 x 11)	2 × (2 × 11)	2 × (4 × 8)
Element length	4.4 mm (0.17 in.)	4.4 mm (0.17 in.)	9.19 mm (0.36 in.)
Element width	12 mm (0.47 in.)	12 mm (0.47 in.)	9.29 mm (0.37 in.)
Active aperture	48 mm (1.89 in.)	48 mm (1.89 in.)	72.8 mm (2.87 in.)
Passive aperture	24 mm (0.94 in.)	24 mm (0.94 in.)	36.4 mm (1.43 in.)
Total footprint	55 mm × 55 mm (2.17 in. × 2.17 in.)	55 mm × 55 mm (2.17 in. × 2.17 in.)	85 mm × 85 mm (3.35 in. × 3.35 in.)

Figure 3.2 Improved Design 500-kHz Phased Array Probe

To ensure that the probes are capable of providing insonification in the areas of interest, the sound fields for all of the probes were simulated using the ZETEC 3-D Ray Tracing Beam Simulation and UT Data Visualization software package. The sound fields generated by this software assume the material to have a constant ultrasonic velocity (e.g., wrought stainless steel);

thus, the software cannot accurately simulate the strong velocity variations caused by the large grain sizes found in CSS. However, the modeling results are not meant to represent actual sound fields in the CSS samples but to show that the probes are capable of producing a useful sound field at the angles and depths required in isotropic material. The results are shown in Figures 3.3 through 3.5. The theoretical beam simulations show that the arrays used in this study are capable (in wrought stainless steel) of projecting a focused sound beam to the depths of interest at angles ranging from 30° to 60°.

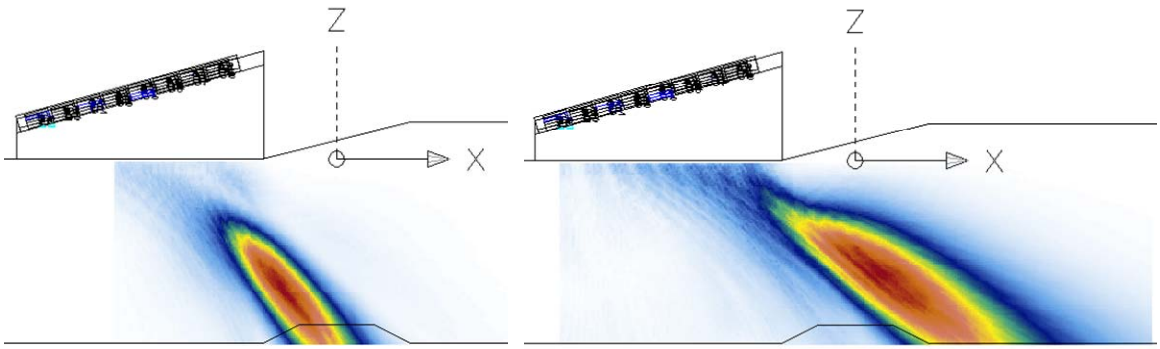

Figure 3.3 Side View of Sound Profile Generated by 500-kHz Probe with Focal Laws Set To Provide Angle of 45° (left) and 60° (right)

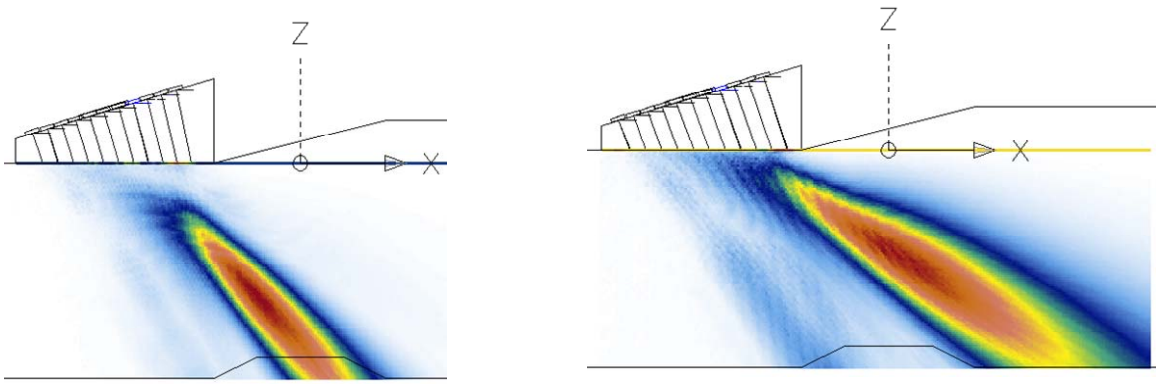

Figure 3.4 Side View of Sound Profile Generated by 750-kHz Probe with Focal Laws Set To Provide Angle of 45° (left) and 60° (right)

The width of the beam is important for determining the resolution capability of the phased array systems. Figure 3.6 depicts beam sizes for the three arrays used in this study. Theoretical simulations for the 500-kHz array show a primary beam diameter of approximately 20 mm (0.79 in.). The 750-kHz array exhibits a slightly narrower beam, with a diameter of 17 mm (0.67 in.), and the 1.0-MHz array has a theoretical beam width of 14 mm (0.55 in.).

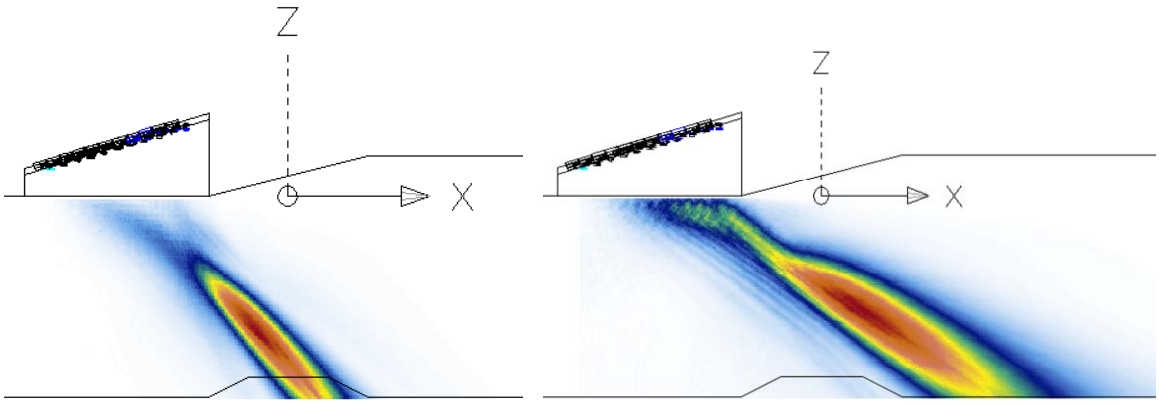

Figure 3.5 Side View of Sound Profile Generated by 1.0-MHz Probe with Focal Laws Set To Provide Angle of 45° (left) and 60° (right)

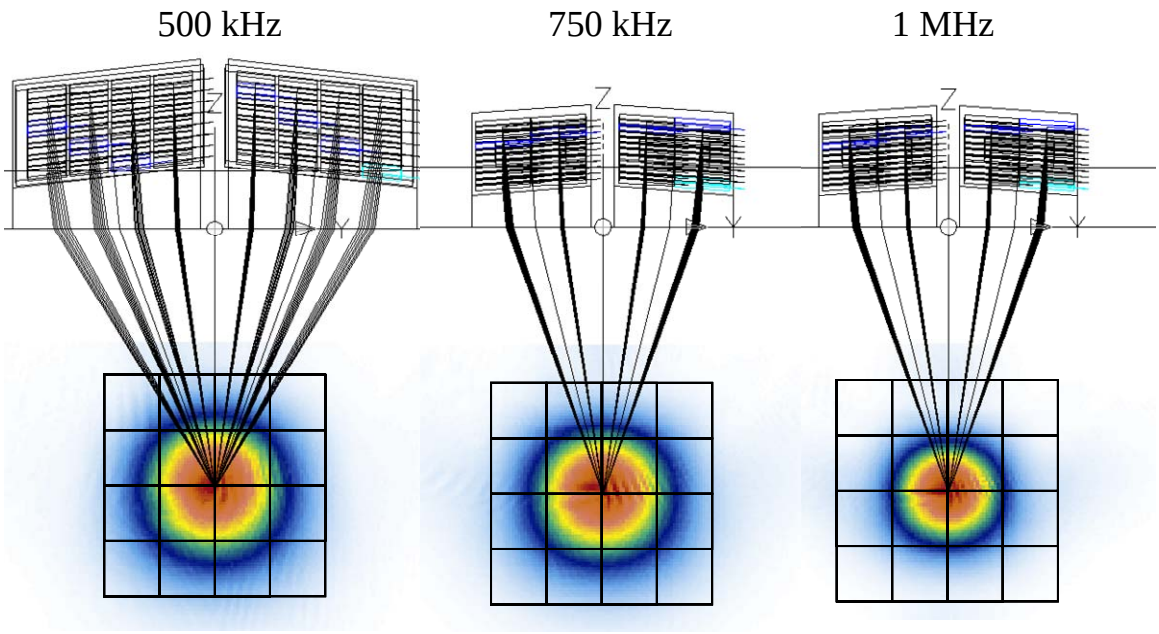

Figure 3.6 View of Sound Profile Generated by 500-kHz, 750-kHz, and 1.0-MHz Array Probes with Focal Laws Set To Provide Angle of 45°. The grid spacing is 12.7 mm (0.5 in.), and the view is from behind the transducer looking in the direction of sound propagation.

The 500-kHz probe was designed to allow an examiner to skew the beam to enhance the detection of branched cracks, such as those generally observed for thermal fatigue cracks. Simulations were performed to determine the range of skew angles possible with the probe and the beam profile at the skew angles of interest. The simulations show that the 500-kHz probe is capable of skewing the beam 20° to either side, as well as shifting the angle horizontally. This skewing is helpful in detecting branching cracks that may not reflect sound directly back to the probe when no skewing is used. Figure 3.7 shows the sound field of the 500-kHz probe when skewed from 0° to 10° and 20°. Although some elongation of the field is exhibited, the primary beam is not radically changed.

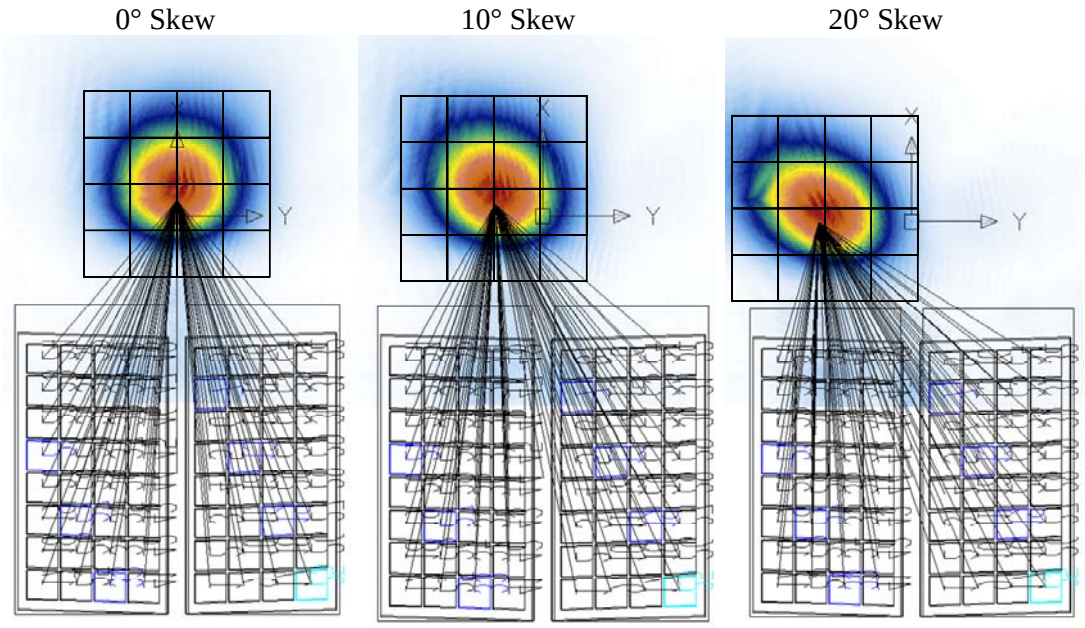

Figure 3.7 Skewing Capabilities of 4 × 8 matrix 500-kHz Probe. The grid spacing is 12.7 mm (0.5 in.).

3.2 Low-Frequency SAFT Probe

A 400-kHz dual-element variable-angle transducer in a pitch-catch configuration was employed in the inspections of the IHI-Southwest and Westinghouse vintage pipe segments and WOG specimens APE-1 and MPE-6. A beam entry angle of 45° in the CCSS material was used for all scans of the corner traps. The photograph in Figure 3.8 shows the dual-element, pitch-catch transducer configuration used in this work.

The longitudinal-wave acoustic velocity in 304 stainless steel is 5.790 mm/μs (0.228 in./μs), while the shear-wave acoustic velocity is 3.180 mm/μs (0.125 in./μs). The equation for calculating wavelength is given by

$$\lambda = \frac{c}{f}$$

where λ is the wavelength, c is the appropriate acoustic velocity for the specific wave mode employed, and f is the frequency. The calculation typically is made using velocity units of centimeters per second or millimeters per second and frequency units of hertz or cycles per second. In this manner, the wavelength

Figure 3.8 Variable-Angle Low-Frequency/SAFT Probe Shown on Westinghouse Piping Segment

calculation results in a familiar unit length. Although the pulser was configured to generate a square-wave excitation of 350 kHz, the peak operating frequency for the transducer was measured at 400 kHz after signal conditioning and amplification. The longitudinal-wave and shear-wave wavelengths at 400 kHz as well as at 500 kHz, 750 kHz, and 1.0 MHz were calculated and are reported in Table 3.3. Near the corner trap, the thicknesses of the specimens ranged from 6.32 cm (2.49 in.) to 8.33 cm (3.28 in.).

Table 3.3 Theoretical Ultrasonic Wavelengths for Austenitic Stainless Steel

Frequency	Longitudinal-Wave λ	Shear-Wave λ
400 kHz	1.45 cm (0.57 in.)	0.79 cm (0.31 in.)
500 kHz	1.16 cm (0.46 in.)	0.64 cm (0.25 in.)
750 kHz	0.77 cm (0.30 in.)	0.42 cm (0.17 in.)
1.0 MHz	0.58 cm (0.23 in.)	0.32 cm (0.13 in.)

4 Cast Stainless Steel Piping Specimens Used in This Study

To assess the affects of varied grain structures on low-frequency UT beam propagation in CSS piping, materials that represent those installed in primary piping circuits at commercial operating plants were needed. Vintage piping segments were made available by EPRI, Westinghouse, Inc., and IHI Southwest Technologies, Inc., for this purpose. These base material specimens were without flaws. Specimens containing flaws included 15 welded piping segments on loan to PNNL by EPRI that were fabricated to be typical of primary coolant loop components in Westinghouse-designed plants and a number of PNNL segments. The Westinghouse specimens contained surface-breaking thermal or mechanical fatigue cracks on either side of the weld. The PNNL specimens, originally fabricated for the Programme for the Inspection of Steel Components (PISC) in the early to mid 1980s, contained surface-breaking thermal fatigue cracks, also on either side of the weld.

Although a metallurgical comparison of structure has not yet been performed between piping at U.S. nuclear power plants and the specimens discussed above, the piping segments loaned to PNNL are believed to represent generic vintage classes of CCSS that were used for fabricating Class 1 reactor coolant piping in all Westinghouse-designed PWRs.

No unflawed segments of statically cast stainless steel (SCSS) piping components—elbows, tees, or valves—were available for use in this study. Specific fabrication parameters used during casting processes that may have produced resultant structures are unclear at the present and not within the scope of the research described in this report.

The unflawed specimens are described in Section 4.1; those with weld flaws are characterized in Section 4.2. In addition, grain size considerations for both specimen types are presented in Section 4.3.

4.1 Unflawed Centrifugally Cast Stainless Steel Base Material Piping

Cross sections in the circumferential-radial plane of the unflawed piping segments were polished, etched, and photographed to document the grain structures in these materials. The photographs were enlarged and used to determine average grain-size measurements via the lineal intercept method. Engineering judgment was employed to define separate regions (if existing) of the CCSS piping cross sections containing similar grain sizes and orientations; a circumferentially oriented line bisecting each of these regions was then applied and used to measure each grain that was intercepted. Measurements of the intercepted grains along this line were averaged to assess approximate grain size by region.

The oldest vintage, or initial CCSS piping fabricated (from early to mid 1960s), is thought to be similar to the IHI Southwest Technologies piping segment, which is 15.24 cm (6 in.) in axial extent by 127 cm (50 in.) in circumferential extent. The segment has an 8.4-cm (3.3-in.) wall thickness and is approximately 91 cm (36 in.) in outside diameter. It consists of coarse-grained, mixed, and banded microstructure and had some surface defects, sawcuts, and notches machined into the specimen but no fabricated or implanted cracks. A photograph of the IHI Southwest Technologies segment is shown in Figure 4.1. This material contains a wide range of grain sizes

and structures, with significant layering, as can be seen in Figure 4.2. Note the variation of grain types as a function of circumferential location. This metallurgical configuration represents the most challenging microstructure for ultrasonic examination because of the variability, overall

Figure 4.1 Centrifugally Cast Stainless Steel Piping Segment Loaned by IHI Southwest Technologies, Inc.

size, and layering of grains. Because of the large variation of grains in this specimen, different regions of the cross section have been false-colored to enable the reader to better visualize the significant range of sizes and shapes present in this early vintage CCSS.

As described above, the sizes listed in Figure 4.2 are a function of an intercept line drawn normal to primary grain growth, which for CCSS is the radial direction. The result is that grain sizes listed are representative of the minor axis of each grain, which, in some cases, also exhibit major axes of extensive lengths. However, during weld examinations, sound beam propagation is more likely to be directed along, or nearer, the minor axes of the grains. For this reason, PNNL researchers decided that this grain dimension measurement was more appropriate.

The next class, or intermediate vintage, of CCSS microstructures is represented by the piping segment on loan from Westinghouse, Inc. This segment is believed to have been fabricated in the late 1960s to mid-1970s and, although the microstructure is still very challenging to examine, shows consistent grain orientation and size throughout the circumference, which may indicate the casting process was becoming more refined. The Westinghouse segment is 25.4 cm (10 in.) in axial extent by 130 cm (51 in.) in circumferential length, with a 6.4-cm (2.5-in.) wall thickness and an approximately 71-cm (28-in.) outside diameter. This segment exhibits a coarse-grained, dendritic (columnar) microstructure with a banding condition evident as well. Figure 4.3 shows

a portion of the circumferentially consistent microstructure of the Westinghouse segment. The specimen contains some minor surface defects, sawcuts, and small notches machined into the surface but no fabricated or implanted cracks. This segment was also polished, etched, and photographed; then a lineal intercept method applied to determine the grain sizes shown in Figure 4.3. A photograph of the Westinghouse segment is shown in Figure 4.4.

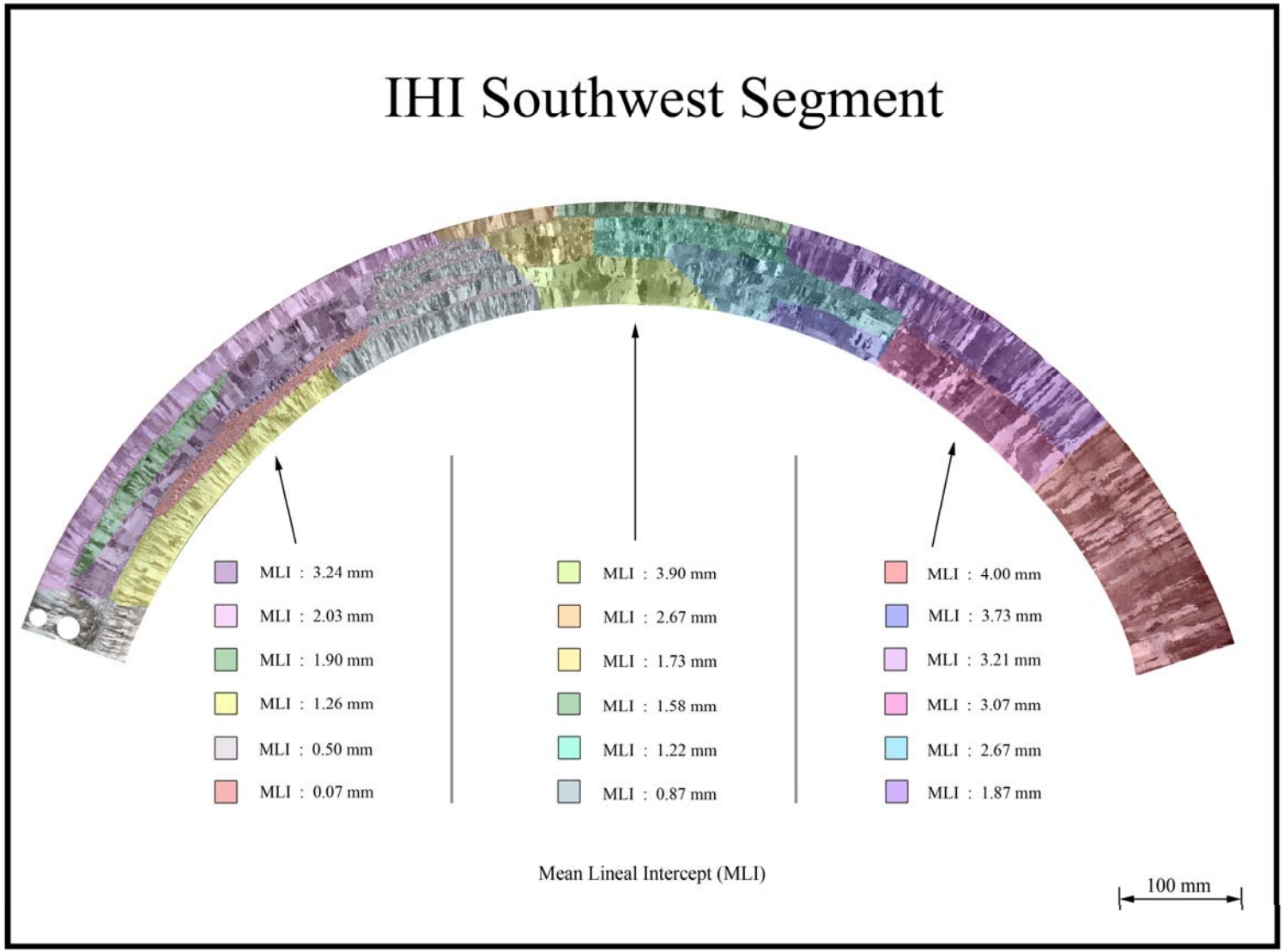

Figure 4.2 False-Color Map Depicting Variation of Grains in CCSS Piping from IHI Southwest Technologies, Inc.

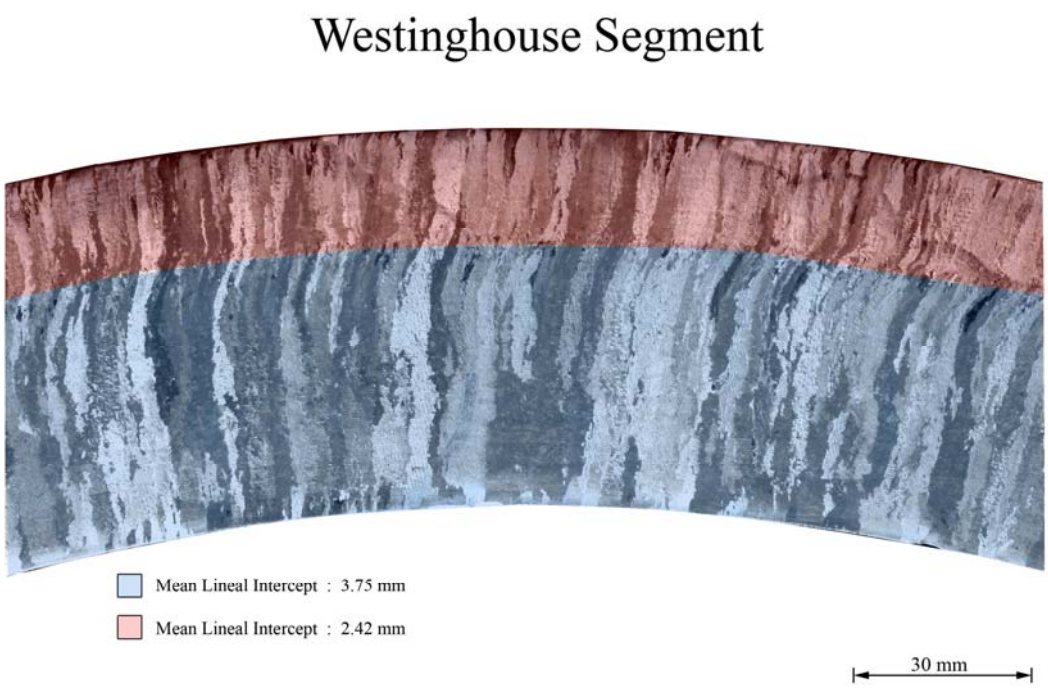

Figure 4.3 Portion of CCSS Piping Specimen from Westinghouse, Inc., Showing Dendritic Grain Structure Observed to be Consistent Throughout Circumference

Figure 4.4 Westinghouse, Inc. CCSS Piping Segment on Loan to PNNL

The most recently fabricated CCSS base material was loaned to PNNL by EPRI and was extracted from a cancelled nuclear power plant in Spain. The large blank spool piece (see Figure 4.5) has consistent fine-grained CCSS microstructure. The piece is 1.86 m (6.1 ft) in length, with a 6.35-cm (2.5-in.) wall thickness and an outside diameter of 86.4 cm (34.0 in.). A ring at one end of the spool piece was cut off, polished, and chemically etched to obtain digital photographs of the material structure. Figure 4.6 depicts a region of the polished and chemically etched ring, which shows the relatively fine (for CCSS) equiaxed microstructure and approximate grain size, present over the entire circumference of the segment. Again, the grain size determination was performed by the lineal intercept method as described previously. This type of microstructure is believed to represent the latest class of CCSS piping installed in primary coolant systems of later vintage Westinghouse-designed plants (circa mid-1970s through mid-1980s). Of all CCSS piping examined in this study, this microstructure is believed to be the least challenging to ultrasonic testing. This premise is to be tested in forthcomings studies.

Figure 4.5 Large Blank Spool Piece on Late-Vintage CCSS Piping from Cancelled Spanish Plant on Loan to PNNL by EPRI

Low-frequency UT was performed on all of the unflawed piping segments to assess the effects of the varied coarse-grained microstructures on beam propagation. The UT was applied from the outside-diameter surface, and by targeting the inside-diameter corner at the end of the segments, measurements of returning signal and inherent material noise were acquired to assess sound penetration for these baseline materials. The results of the baseline material UT work are described in Section 5 of this report.

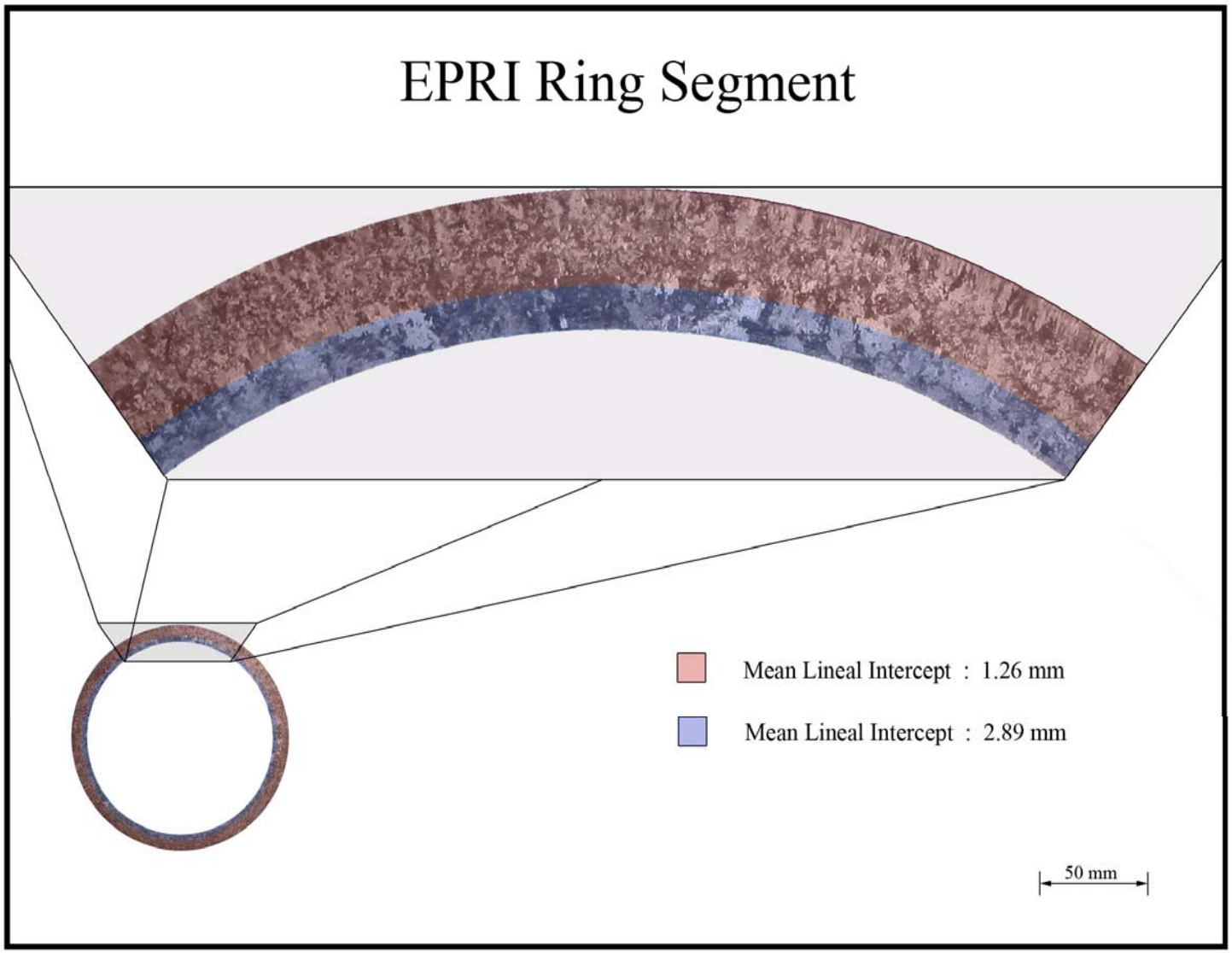

Figure 4.6 Portion of Westinghouse, Inc. CCSS Piping Segment Showing Dendritic Grain Structure Observed To Be Consistent Throughout Circumference

4.2 Welded Flaw Specimens

Fifteen welded piping specimens fabricated by the industry's Westinghouse Owners Group (WOG) were loaned to PNNL by EPRI for this study. These specimens represent typical configurations of several components in the primary coolant loop of Westinghouse-designed plants, and contain surface-breaking thermal or mechanical fatigue cracks located on either side of a weld joining CSS to CSS or CSS to wrought stainless steel (WSS) materials. The flaws are basically considered to be planar cracks oriented parallel to the weld centerline, and perpendicular to and connected to the inside diameter surface. However, the fabrication processes have also created some transverse cracking in some of the specimens. In general, the tightness and branched orientations of the thermal fatigue cracks make them more difficult to ultrasonically detect in comparison to the mechanical fatigue cracks. Each specimen was assigned a designation that indicates the mock-up configuration. The piping configurations and crack details for the WOG specimens used in this study are described in Table 4.1. A photograph showing the WOG specimens is presented as Figure 4.7. Note the varied inside- and outside-diameter surface conditions indicative of piping geometries installed in the field.

Table 4.1 Westinghouse Owners Group Specimens Available for This Study

WOG Specimen	Mock-Up Configuration	Crack Type	Crack Through-Wall (%)	Crack Location (Side of Weld)
APE-1	CCSS pipe-to-SCSS elbow	MF	13	SCSS
APE-4	CCSS pipe-to-SCSS elbow	MF	14	SCSS
INE-A-1	SCSS elbow-to-WSS safe end	MF	42	SCSS
INE-A-4	SCSS elbow-to-WSS safe end	TF	29	SCSS
INE-A-5	SCSS elbow-to-WSS safe end	MF	34	WSS
MPE-3	CCSS pipe-to-SCSS elbow	MF	30	SCSS
MPE-6	CCSS pipe-to-SCSS elbow	TF	18	SCSS
ONP-D-2	CCSS pipe-to-WSS safe end	TF	28	CCSS
ONP-D-5	CCSS pipe-to-WSS safe end	MF	18	CCSS
ONP-3-5	CCSS pipe-to-WSS safe end	TF	28	WSS
ONP-3-8	CCSS pipe-to-WSS safe end	MF	28	WSS
OPE-2	CCSS pipe-to-SCSS elbow	MF	18	SCSS
OPE-5	CCSS pipe-to-SCSS elbow	TF	23	SCSS
POP-7	CCSS pipe-to-SCSS pump nozzle	MF	31	SCSS
POP-8	CCSS pipe-to-SCSS pump nozzle	TF	18	CCSS

WOG specimen APE-1 is 25.4 cm (10.0 in.) wide (circumferential distance) and 60.96 cm (24.0 in.) long in axial extent. This specimen is a statically cast elbow to centrifugally cast pipe section in which the elbow side is 8.89 cm (3.5 in.) thick and the pipe side is 6.6 cm (2.6 in.) thick. The statically cast microstructure is defined as thin-band equiaxed grains, while the

centrifugally cast microstructure is defined as bands of coarse columnar grains mixed with bands of small equiaxed grains. The crack in APE-1 is a mechanical fatigue crack on the elbow

Figure 4.7 Westinghouse Owners Group Specimens Showing Varied Inside and Outside Surface Geometries Typical of Field-Installed Components

side of the weld centerline, with a circumferential extent (length) of 3.94 cm (1.55 in.) and a depth of 1.14 cm (0.45 in.). See Figure A.1 in Appendix A for an image of the microstructural detail and inside/outside surface geometries typical of the APE weld configuration.

Specimen APE-4 is 20.3 cm (8.0 in.) wide (circumferential distance) and 60.96 cm (24.0 in.) long in axial extent. This specimen is a statically cast elbow to centrifugally cast pipe section, where the elbow side is 8.89 cm (3.5 in.) thick and the pipe side is 6.6 cm (2.6 in.) thick. The statically cast microstructure is defined as thin-band equiaxed grains, while the centrifugally cast microstructure is defined as bands of coarse columnar grains mixed with bands of small equiaxed grains. The crack in APE-4 is a mechanical fatigue crack on the pipe side of the weld centerline, with a circumferential extent (length) of 4.19 cm (1.65 in.) and a depth of 1.27 cm (0.5 in.). See Figure A.1 in Appendix A for an image of the microstructural detail and inside/outside surface geometries typical of the APE weld configuration.

Specimen INE-A-1 is 26.0 cm (10.25 in.) wide (circumferential distance) and 60.96 cm (24.0 in.) long in axial extent. This specimen is a clad carbon steel inlet nozzle to forged stainless steel safe end to statically cast elbow section, where the nozzle side consists of 6.6-cm (2.6-in.) thick carbon steel and 0.76-cm (0.3-in.) thick cladding. The forged stainless steel safe end is 7.37 cm (2.9 in.) thick, and the SCSS elbow segment is 6.35 cm (2.5 in.) thick. Both clad carbon steel and forged stainless steel segments are defined as consisting of a fine-grained equiaxed microstructure, while the statically cast microstructure is defined as a coarse matrix of grains. The crack in INE-A-1 is a mechanical fatigue crack on the elbow side of the weld centerline

between the forged stainless steel elbow segment, with a circumferential extent (length) of 6.99 cm (2.75 in.) and a depth of 2.64 cm (1.04 in.). See Figure A.2 in Appendix A for an image of the microstructural detail and inside/outside surface geometries typical of the INE-A weld configuration.

Specimen INE-A-4 is 20.3 cm (8.0 in.) wide (circumferential distance) and 60.96 cm (24.0 in.) long in axial extent. This specimen is a clad carbon steel inlet nozzle to forged stainless steel safe end to statically cast elbow section, where the nozzle side consists of 6.6 cm (2.6 in.) thick carbon steel and 0.76 cm (0.3 in.) thick cladding. The forged stainless steel safe end is 7.37 cm (2.9 in.) thick, and the SCSS elbow segment is 6.35 cm (2.5 in.) thick. Both clad carbon steel and forged stainless steel segments are defined as consisting of a fine-grained equiaxed microstructure, while the statically cast microstructure is defined as a coarse matrix of grains. The crack in INE-A-4 is a thermal fatigue crack on the elbow side of the weld centerline between the forged stainless steel elbow segment, with a circumferential extent (length) of 6.86 cm (2.7 in.) and a depth of 1.85 cm (0.73 in.). See Figure A.2 in Appendix A for an image of the microstructural detail and inside/outside surface geometries typical of the INE-A weld configuration.

Specimen INE-A-5 is 25.4 cm (10.0 in.) wide (circumferential distance) and 60.96 cm (24.0 in.) long in axial extent. This specimen is a clad carbon steel inlet nozzle to forged stainless steel safe end to statically cast elbow section, where the nozzle side consists of 6.6-cm (2.6-in.) thick carbon steel and 0.76-cm (0.3-in.) thick cladding. The forged stainless steel safe end is 7.37 cm (2.9 in.) thick, and the SCSS elbow segment is 6.35 cm (2.5 in.) thick. Both clad carbon steel and forged stainless steel segments are defined as consisting of a fine-grained equiaxed microstructure, while the statically cast microstructure is defined as a coarse matrix of grains. The crack in INE-A-5 is a mechanical fatigue crack on the safe end side of the weld centerline between the forged stainless steel-elbow segment, with a circumferential extent (length) of 6.73 cm (2.65 in.) and a depth of 2.54 cm (1.0 in.). See Figure A.2 in Appendix A for an image of the microstructural detail and inside/outside surface geometries typical of the INE-A weld configuration.

Specimen MPE-3 is 20.3 cm (8.0 in.) wide (circumferential distance) and 60.96 cm (24.0 in.) long in axial extent. This specimen is a statically cast elbow to centrifugally cast pipe section, where the elbow side is 8.38 cm (3.3 in.) thick and the pipe side is 6.6 cm (2.6 in.) thick. Both the statically cast and centrifugally cast microstructures are defined as a coarse-mixed matrix of grains. The crack in MPE-3 is a mechanical fatigue crack on the pipe side of the weld centerline, with a circumferential extent (length) of 6.73 cm (2.65 in.) and a depth of 2.54 cm (1.0 in.). See Figure A.3 in Appendix A for an image of the microstructural detail and inside/outside surface geometries typical of the MPE weld configuration.

Specimen MPE-6 is 26.0 cm (10.25 in.) wide (circumferential distance) and 60.96 cm (24.0 in.) long in axial extent. This specimen is a statically cast elbow to centrifugally cast pipe section, where the elbow side is 8.38 cm (3.3 in.) thick and the pipe side is 6.6 cm (2.6 in.) thick. Both the statically cast and centrifugally cast microstructures are defined as a coarse-mixed matrix of grains. The crack in MPE-6 is a thermal fatigue crack on the elbow side of the weld centerline, with a circumferential extent (length) of 5.92 cm (2.33 in.) and a depth of 1.50 cm (0.59 in.). See

Figure A.3 in Appendix A for an image of the microstructural detail and inside/outside surface geometries typical of the MPE weld configuration.

Specimen ONP-D-2 is 25.4 cm (10.0 in.) wide (circumferential distance) and 61.6 cm (24.25 in.) long in axial extent. This specimen is a clad carbon steel outlet nozzle to forged stainless steel safe end to centrifugally cast pipe section, where the nozzle side consists of 6.86-cm (2.7-in.) thick carbon steel and 0.51-cm (0.2-in.) thick cladding. The forged stainless steel safe end is 7.37 cm (2.9 in.) thick, and the CCSS pipe segment is 6.35 cm (2.5 in.) thick. Both clad carbon steel and forged stainless steel segments are defined as consisting of a fine-grained microstructure, while the centrifugally cast microstructure is defined as a coarse-mixed matrix of grains. The crack in ONP-D-2 is a thermal fatigue crack on the pipe side of the weld centerline between the forged stainless steel-CSS pipe segment, with a circumferential extent (length) of 6.6 cm (2.6 in.) and a depth of 1.78 cm (0.7 in.). See Figure A.44 in Appendix A for an image of the microstructural detail and inside/outside surface geometries typical of the ONP-D weld configuration.

Specimen ONP-D-5 is 25.4 cm (10.0 in.) wide (circumferential distance) and 61.6 cm (24.25 in.) long in axial extent. This specimen is a clad carbon steel outlet nozzle to forged stainless steel safe end to centrifugally cast pipe section, where the nozzle side consists of 6.86-cm (2.7-in.) thick carbon steel and 0.51-cm (0.2-in.) thick cladding. The forged stainless steel safe end is 7.37 cm (2.9 in.) thick, and the CCSS pipe segment is 6.35 cm (2.5 in.) thick. Both clad carbon steel and forged stainless steel segments are defined as consisting of a fine-grained microstructure, while the centrifugally cast microstructure is defined as a coarse-mixed matrix of grains. The crack in ONP-D-5 is a mechanical fatigue crack on the pipe side of the weld centerline between the forged stainless steel-CSS pipe segment, with a circumferential extent (length) of 4.06 cm (1.6 in.) and a depth of 1.19 cm (0.47 in.). See Figure A.4 in Appendix A for an image of the microstructural detail and inside/outside surface geometries typical of the ONP-D weld configuration.

Specimen ONP-3-5 is 20.3 cm (8.0 in.) wide (circumferential distance) and 61.6 cm (24.25 in.) long in axial extent. This specimen is a clad carbon steel outlet nozzle to forged stainless steel safe end to centrifugally cast pipe section, where the nozzle side consists of 6.60-cm (2.6-in.) thick carbon steel and 0.51-cm (0.2-in.) thick clad. The forged stainless steel safe end is 7.11 cm (2.8 in.) thick, and the CCSS pipe segment is 6.35 cm (2.5 in.) thick. Both clad carbon steel and forged stainless steel segments are defined as consisting of a fine-grained microstructure, while the centrifugally cast microstructure is defined as a coarse matrix of grains. The crack in ONP-3-5 is a thermal fatigue crack on the safe-end side of the weld centerline between the nozzle segment and the forged stainless steel safe-end segment, with a circumferential extent (length) of 6.6 cm (2.6 in.) and a depth of 1.78 cm (0.7 in.). See Figure A.5 in Appendix A for an image of the microstructural detail and inside/outside surface geometries typical of the ONP weld configuration.

Specimen ONP-3-8 is 20.3 cm (8.0 in.) wide (circumferential distance) and 61.6 cm (24.25 in.) long in axial extent. This specimen is a clad carbon steel outlet nozzle to forged stainless steel safe end to centrifugally cast pipe section, where the nozzle side consists of 6.60-cm (2.6-in.) thick carbon steel and 0.51-cm (0.2-in.) thick clad. The forged stainless steel safe end is 7.11 cm

(2.8 in.) thick, and the CCSS pipe segment is 6.35 cm (2.5 in.) thick. Both clad carbon steel and forged stainless steel segments are defined as consisting of a fine-grained microstructure, while the centrifugally cast microstructure is defined as a coarse matrix of grains. The crack in ONP-3-8 is a mechanical fatigue crack on the outlet nozzle side of the weld centerline between the nozzle segment and the forged stainless steel safe-end segment, with a circumferential extent (length) of 5.13 cm (2.02 in.) and a depth of 1.78 cm (0.7 in.). See Figure A.5 in Appendix A for an image of the microstructural detail and inside/outside surface geometries typical of the ONP weld configuration.

Specimen OPE-2 is 25.4 cm (10.0 in.) wide (circumferential distance) and 52.1 cm (20.5 in.) long in axial extent. This specimen is a statically cast elbow to centrifugally cast pipe section, where the elbow side is 7.11 cm (2.8 in.) thick and the pipe side is 5.84 cm (2.3 in.) thick. Both the statically cast and centrifugally cast microstructures are defined as a coarse matrix of grains. The crack in OPE-2 is a mechanical fatigue crack on the elbow side of the weld centerline, with a circumferential extent (length) of 4.19 cm (1.65 in.) and a depth of 1.27 cm (0.5 in.). See Figure A.6 in Appendix A for an image of the microstructural detail and inside/outside surface geometries typical of the OPE weld configuration.

Specimen OPE-5 is 20.3 cm (8.0 in.) wide (circumferential distance) and 52.1 cm (20.5 in.) long in axial extent. This specimen is a statically cast elbow to centrifugally cast pipe section, where the elbow side is 7.11 cm (2.8 in.) thick and the pipe side is 5.84 cm (2.3 in.) thick. Both the statically cast and centrifugally cast microstructures are defined as a coarse matrix of grains. The crack in OPE-5 is a thermal fatigue crack on the elbow side of the weld centerline, with a circumferential extent (length) of 6.15 cm (2.42 in.) and a depth of 1.63 cm (0.64 in.). See Figure A.6 in Appendix A for an image of the microstructural detail and inside/outside surface geometries typical of the OPE weld configuration.

Specimen POP-7 is 25.4 cm (10.0 in.) wide (circumferential distance) and 53.3 cm (21 in.) long in axial extent. This specimen is a statically cast pump outlet nozzle to centrifugally cast pipe section, where the nozzle segment is 8.38 cm (3.3 in.) thick and the pipe side is 6.6 cm (2.6 in.) thick. Both the statically cast and centrifugally cast microstructures are defined as a coarse-mixed matrix of grains. The crack in POP-7 is a mechanical fatigue crack on the elbow side of the weld centerline, with a circumferential extent (length) of 6.78 cm (2.67 in.) and a depth of 2.57 cm (1.01 in.). See Figure A.7 in Appendix A for an image of the microstructural detail and inside/outside surface geometries typical of the POP weld configuration.

Specimen POP-8 is 25.4 cm (10.0 in.) wide (circumferential distance) and 53.3 cm (21 in.) long in axial extent. This specimen is a statically cast pump outlet nozzle to centrifugally cast pipe section, where the nozzle segment is 8.38 cm (3.3 in.) thick and the pipe side is 6.6 cm (2.6 in.) thick. Both the statically cast and centrifugally cast microstructures are defined as a coarse-mixed matrix of grains. The crack in POP-8 is a thermal fatigue crack on the pipe side of the weld centerline, with a circumferential extent (length) of 5.72 cm (2.25 in.) and a depth of 1.50 cm (0.59 in.). See Figure A.7 in Appendix A for an image of the microstructural detail and inside/outside surface geometries typical of the POP weld configuration.

The PNNL specimens consist of sections cut from butt-welded, 845-mm (33.3-in.)-OD, 60-mm (2.4-in.)-thick CCSS pipe. This pipe material was from two different heats of ASTM A-351 Grade CF-8A, a centrifugally cast material (Diaz et al. 1998). Many of these specimens have been used in a variety of other studies, and many have labels and identification numbers scribed on them; those labels/scribe numbers are used in this report to aid in distinguishing individual specimens. Many of these specimens contain welds approximately in the middle of each section and were made by welders qualified to meet Section III requirements of the ASME Code. The welds in these specimens were made under shop conditions but are typical of field practice. The weld crowns were ground relatively smooth and blended with the parent pipe, although troughs between weld paths are still present. The ID surface contours are significantly smoother than those of the WOG specimens described earlier. Although these specimens exhibit shallow counterbore facets, the ID surface conditions are relatively smooth, with smoother contour transitions between the weld root, counterbore, and parent material segments.

The cracks in these pipe sections were created using laboratory methods developed at PNNL that have proven useful in producing realistic surface-connected thermal fatigue cracks. The flaws in these specimens are basically considered to be planar cracks, parallel to the weld centerline and perpendicular to and connected to the ID. As previously reported, the tightness and roughness of the thermal fatigue cracks generally make them more difficult to detect in comparison to mechanical fatigue cracks. These specimens had a scribe line located near, but not necessarily coincident with, the weld centerline, which was to be used as the reference line for axial offset measurements. One side of these specimens was marked "-" and the other side "+" to indicate which half of the specimen was to be examined and also to give the directional sign to put on the axial scribe offset measurement for any indications. Specimens marked with "C" or "E" denote columnar microstructure or equiaxed microstructure, respectively.

The PNNL specimens used in this study are listed in Table 4.2 and described below. A photograph in Appendix A.8 shows the grain structure from B515 and is representative of the PNNL specimens. Flaw depths were estimated based on crack growth cycles. Two PNNL specimens from the earlier PNNL conducted Piping Inspection Round Robin (Heasler 1996) were destructively analyzed for flaw sizing confirmation. One of the samples was 7 percent below expected crack depth while the other was 48 percent low. From these limited results a large error may be associated with the reported PNNL TF crack depths.

Table 4.2 PNNL Specimens Available for This Study

Specimen ID	Flaw Type	Flaw Location (side of weld)	Flaw Through-Wall Depth (%)
B501	TFC	Equiaxed	34
B504	TFC	Equiaxed	48
B505	Notch	Equiaxed	10
B508	TFC	Columnar	33
B515	TFC – Mechanically Bent Open and Closed	Equiaxed	25
B519	TFC	Equiaxed	46
B520	TFC	Columnar	16

PNNL Specimen B-501 is 18.19 cm (7.16 in.) wide (circumferential distance) and 40.4 cm (15.92 in.) long in axial extent. This specimen is configured as a pipe-to-pipe segment with the (-) side consisting of intermediate-size columnar grains and the (+) side consisting of intermediate-size equiaxed grains. The weldment is located approximately in the center of the pipe-to-pipe segment, and the weld crown was ground relatively smooth and blended with the parent pipe. The equiaxed segment of this specimen is 5.84 cm (2.3 in.) thick, and the columnar segment of this specimen is 5.59 cm (2.2 in.) thick. The segment thickness at the weld centerline is 5.51 cm (2.17 in.). Originally, this specimen was intentionally fabricated as a blank specimen and contained no crack for the PIRR and the PISC II assessments. Subsequently, however, a thermal fatigue crack was introduced into this specimen by Trueflaw Ltd. (Espoo, Finland) using its patented crack production technology. This work was performed to compare the thermal fatigue crack produced by Trueflaw with those manufactured by PNNL.

PNNL used a process of placing a small starter notch (approximately 0.5 mm [0.020 in.] deep) at the site where the flaw was to be introduced. After the crack was grown, the starter notch was carefully machined away. This results in some modifications to the material and has always been a concern as to whether this might be detectable by the NDE method being employed. The Trueflaw method does not require the use of a starter notch. Rather, it employs a technique that concentrates the heating in the area where crack formation is desired; thus, that is the only place where the crack can initiate and grow. Because this is a different process for introducing thermal fatigue cracks, PNNL wanted to assess this process and compare it to the process that PNNL has previously used. Trueflaw introduced a crack into this specimen 2.92 cm (1.15 in.) long. The intent was to grow something that has a depth of about 20 mm (0.79 in.) because this would make it approximately one-third of the wall thickness. The actual depth of this crack as well as all of the cracks in CSS are not well known because it is very difficult to obtain any tip signals.

PNNL Specimen B-504 is 17.78 cm (7.0 in.) wide (circumferential distance) and 40.4 cm (15.91 in.) long in axial extent. This specimen is configured as a pipe-to-pipe segment with the (+) side consisting of intermediate-size columnar grains and the (-) side consisting of intermediate-size equiaxed grains. The weldment is located approximately in the center of the pipe-to-pipe segment, and the weld crown was ground relatively smooth and blended with the parent pipe. This specimen has a thermal fatigue crack on the equiaxed side of the weld. The crack is 6.15 cm (2.42 in.) in length (circumferential extent) and 2.79 cm (1.10 in.) deep. The equiaxed segment of this specimen is 5.84 cm (2.3 in.) thick; the columnar segment is 5.84 cm (2.3 in.) thick. The segment thickness at the weld centerline is 5.51 cm (2.17 in.).

Specimen B-505 is a pipe section 40 cm (15.75 in.) long (axial extent), 17.15 cm (6.75 in.) wide, and 5.8 cm (2.28 in.) thick containing microstructures both fine-grained equiaxed (on the plus side of the weld) and fine-grained columnar (located on the minus side of the weld). This CSS calibration block was a section cut from a butt-welded, 845-mm-OD, 60-mm-thick (33.267-in.-OD, 2.362-in.-thick) CCSS pipe containing a weld located approximately in the middle of the section. It was fabricated by welders qualified to meet Section III requirements of ASME Code. The weld crown was ground relatively smooth and blended with the parent pipe, although troughs between weld paths are still present. This specimen also contains three 10% through-

wall notches, 5.72 cm (2.25 in.) in length and 0.635 cm (0.25 in.) in width, two on the columnar side and one on the equiaxed side of the weld root, as well as a gouged-out area (defined as a minor surface indication) along the ID of the weld root with small dimensions. This specimen also contains a number of 4.76-mm (0.188-in.)-diameter side-drilled holes at ¼ T, ½ T, and ¾ T depths on both sides of the weld.

PNNL Specimen B-508 is 18.65 cm (7.34 in.) wide (circumferential distance) and 40.32 cm (15.88 in.) long in axial extent. This specimen is configured as a pipe-to-pipe segment with the (+) side consisting of intermediate-size columnar grains and the (-) side consisting of intermediate-size equiaxed grains. The weldment is located approximately in the center of the pipe-to-pipe segment, and the weld crown was ground relatively smooth and blended with the parent pipe. This specimen has a thermal fatigue crack on the columnar side of the weld. The crack is estimated to be 4.83 cm (1.90 in.) in length (circumferential extent) and 1.96 cm (0.77 in.) deep. The equiaxed segment of this specimen is 5.77 cm (2.27 in.) thick; the columnar segment is 5.92 cm (2.33 in.) thick. The segment thickness at the weld centerline is 5.39 cm (2.12 in.).

Specimen B-515 is 18.16 cm (7.15 in.) wide (circumferential distance) and 40.4 cm (15.91 in.) long in axial extent. This specimen is configured as a pipe-to-pipe segment with the (-) side consisting of intermediate-size columnar grains and the (+) side consisting of intermediate-size equiaxed grains. The weldment is located approximately in the center of the pipe-to-pipe segment, and the weld crown was ground relatively smooth and blended with the parent pipe. This specimen has a thermal fatigue crack on the equiaxed (+) side of the weld with an offset of 0.13 cm (0.05 in.) from the weld centerline. The crack is 2.92 cm (1.15 in.) in length (circumferential extent) and 1.52 cm (0.6 in.) deep. The equiaxed segment of this specimen is 5.84 cm (2.3 in.) thick, and the columnar segment of this specimen is 6.05 cm (2.38 in.) thick. The segment thickness at the weld centerline is 5.49 cm (2.16 in.). This specimen is special in that #B-515 has been thermally stress-relieved, mechanically bent open, and then bent back to its original shape. This resulted in an open, easier-to-detect crack, which may not mimic defects anticipated to be found in service.

Specimen B-519 is 18.16 cm (7.15 in.) wide (circumferential distance) and 40.4 cm (15.91 in.) long in axial extent. This specimen is configured as a pipe-to-pipe segment with the (-) side consisting of intermediate-size columnar grains and the (+) side consisting of intermediate-size equiaxed grains. The weldment is approximately in the center of the pipe-to-pipe segment, and the weld crown was ground relatively smooth and blended with the parent pipe. This specimen has a thermal fatigue crack on the equiaxed (+) side of the weld with an offset of 0.25 cm (0.1 in.) from the weld centerline. The crack is 5.72 cm (2.25 in.) in length (circumferential extent) and 2.79 cm (1.10 in.) deep. The equiaxed segment of this specimen is 5.79 cm (2.28 in.) thick, and the columnar segment of this specimen is 6.05 cm (2.38 in.) thick. The segment thickness at the weld centerline is 5.49 cm (2.16 in.).

PNNL Specimen B-520 is 17.54 cm (6.91 in.) wide (circumferential distance) and 40.32 cm (15.88 in.) long in axial extent. This specimen is configured as a pipe-to-pipe segment with one side consisting of intermediate-size columnar grains and the other side consisting of intermediate-size equiaxed grains. The weldment is located approximately in the center of the

pipe-to-pipe segment, and the weld crown was ground relatively smooth and blended with the parent pipe. This specimen has a thermal fatigue crack on the columnar side of the weld. The crack is estimated to be 2.67 cm (1.05 in.) in length (circumferential extent) and 0.64-1.27 cm (0.25-0.50 in.) deep. The equiaxed segment of this specimen is 5.77 cm (2.27 in.) thick; the columnar segment is 6.05 cm (2.38 in.) thick. The segment thickness at the weld centerline is 5.39 cm (2.12 in.).

4.3 Grain Size Considerations

As shown in Figures 4.2 through 4.7 and those in Appendix A, the cumulative average size of grains in varied regions of the CSS materials has been measured by a lineal mean intercept method. However, this average is not a reliable indicator of overall dominant grain sizes and distributions for the specimens used in this study. Table 4.3 provides more insight into a dominant grain size by listing the minimum and maximum for each type of piping segment examined.

By applying good engineering judgment during a review of the mean, minimum, and maximum values, while observing the cross-sectional microstructural photographs, one may approximate the overall size of grains through which the sound fields must propagate. In general, grains in the range of 12-15 mm (0.47-0.59 in) in diameter are found for the SCSS, while 17-20 mm (0.67-0.79 in) grains are typical for the CCSS.

Table 4.3 Range of Grain Sizes in Cast Stainless Steel Specimens

Specimen	CCSS		SCSS	
	Minimum	**Maximum**	**Minimum**	**Maximum**
EPRI Ring	0.50 mm (0.02 in.)	7.4 mm (0.29 in.)	n/a	n/a
IHI Southwest	<0.20 mm <0.008 in.	25.0 mm (0.98 in.)	n/a	n/a
Westinghouse	0.64 mm (0.03 in.)	16.32 mm (0.64 in.)	n/a	n/a
APE-1	0.44 mm (0.02 in.)	8.86 mm (0.35 in.)	0.89 mm (0.03 in.)	9.31 mm (0.37 in.)
INE-A-5	n/a	n/a	0.38 mm (0.01 in.)	4.14 mm (0.16 in.)
MPE-6	0.56 mm (0.02 in.)	26.81 mm (1.06 in.)	0.28 mm (0.01 in.)	5.59 mm (0.22 in.)
ONP-3-8	0.33 mm (0.01 in.)	26.67 mm (1.05 in.)	n/a	n/a
ONP-D-5	0.83 mm (0.03 in.)	20.27 mm (0.80 in.)	n/a	n/a
OPE-5	0.21 mm (0.01 in.)	16.67 mm (0.66 in.)	0.21 mm (0.01 in.)	5.21 mm (0.21 in.)
POP-8	0.21 mm (0.01 in.)	15.69 mm (0.62 in.)	0.21 mm (0.01 in.)	8.26 mm (0.33 in.)
B515-col	0.6 mm (0.02 in.)	12 mm (0.47 in.)	n/a	n/a
B515-equi	0.6 mm (0.02 in.)	7 mm (0.28 in.)	n/a	n/a

5 Baseline Material Noise Analyses in Centrifugally Cast Stainless Steel Piping

Phased array (PA) and low-frequency/SAFT-UT inspections were conducted on PNNL and WOG specimens, and large pipe segments on loan from Westinghouse, IHI Southwest Technologies, Inc. (IHI-SW), and EPRI, to assess inherent material noise. Only phased array data was collected on the PNNL specimens. The large pipe segments, WOG specimens, and one PNNL specimen were subsequently prepared, polished, and chemically etched to enhance the microstructure of the grains for visual appearance. An assessment of the baseline ultrasonic noise levels in the large vintage piping segments and selected welded specimens was made by acquiring the signal responses from the end-of-block corner-trap geometry free of cracks, flaws, or other reflectors. Measurements were conducted, and subsequent analyses quantified the linear percentage detection (of the total specimen length scanned) as a function of the signal-to-noise ratio of the corner-trap response. From a geometrical perspective, the corner trap acts as a perfect ultrasonic inspection reflector, representing a 100% through-wall flaw. This provided a metric for establishing background noise levels due solely to the microstructure, relative to what is essentially the largest flaw possible in the end-of-block corner-trap response. Here the effectiveness of PA and the low-frequency/SAFT method was qualitatively assessed by imaging the −6-dB signal responses from the corner trap and determining the percentage detection over the entire length of the scanned specimen for large-grained CCSS specimens representing varied thickness, grain size, and orientation conditions.

5.1 Phased Array Base Metal Examination of Unflawed Centrifugally Cast Stainless Steel Material

The corner responses from the IHI-SW, EPRI, and Westinghouse vintage pipe segments and WOG specimens APE-1, MPE-3, OPE-5, and POP-7 were recorded at three inspection frequencies of 500 kHz, 750 kHz and 1.0 MHz using PA. Line scans were acquired over approximately 102- to 155-cm (40- to 61-in.) long sections in the three vintage pipe segments and over 18 to 25 cm (7 to 10 in.) on the four WOG specimens. Line scans were also acquired with the 500 kHz PA probe on PNNL specimens B508, B511, and B520. These narrow specimens only accommodated approximately an 8-cm (3-in.) scan. Both the equiaxed CSS end and columnar CSS end of these two pieces were examined. The laboratory setup for data acquisition on the IHI-SW piece is shown in Figure 5.1. Without interference from the large grains, the response from such a line scan would appear as an even, unbroken response across the entire image. In this material, the response is found to be broken and varying in amplitude.

The data from 30° to 60° for a particular segment/specimen and frequency applied were merged, and the merged files were evaluated for signal and noise information as well as the presence or absence of the corner-reflected signal. Figure 5.2 shows the B-scan side views for the IHI-SW segment at 500 kHz, 750 kHz, and 1.0 MHz, with the corner response running horizontally through the image. The full view of the polished and etched surface is shown in Figure 5.3, with arrows marking the start and end of the scans. The 500-kHz, 750-kHz and 1.0-MHz scans all show, to some degree, a loss of signal near 50.8 cm (20 in.) in the scan. A more detailed image

of the corresponding loss of signal location on the polished and etched photograph is shown in Figure 5.4. This appears to be an area where the material is changing

Figure 5.1 Laboratory Setup for Phased Array Data Acquisition on the IHI-SW Vintage Piping Segment

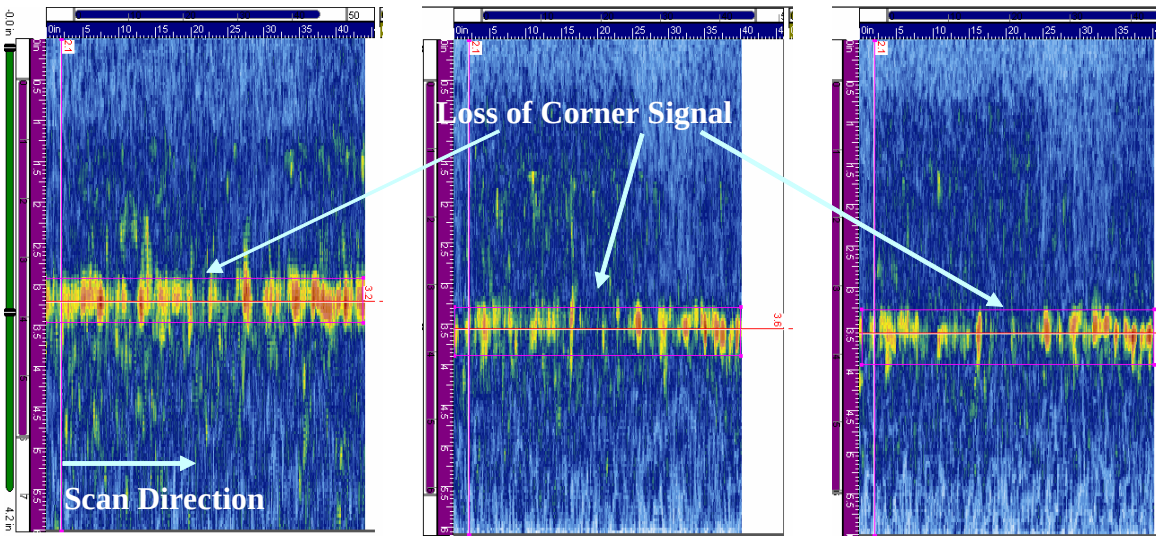

Figure 5.2 Merged B-Scan Views of IHI-SW Segment Corner Signal at 500 kHz (left), 750 kHz (center), and 1.0 MHz (right). Scan length is 112 cm (49 in.), 102 cm (40 in.), and 98 cm (39 in.), respectively.

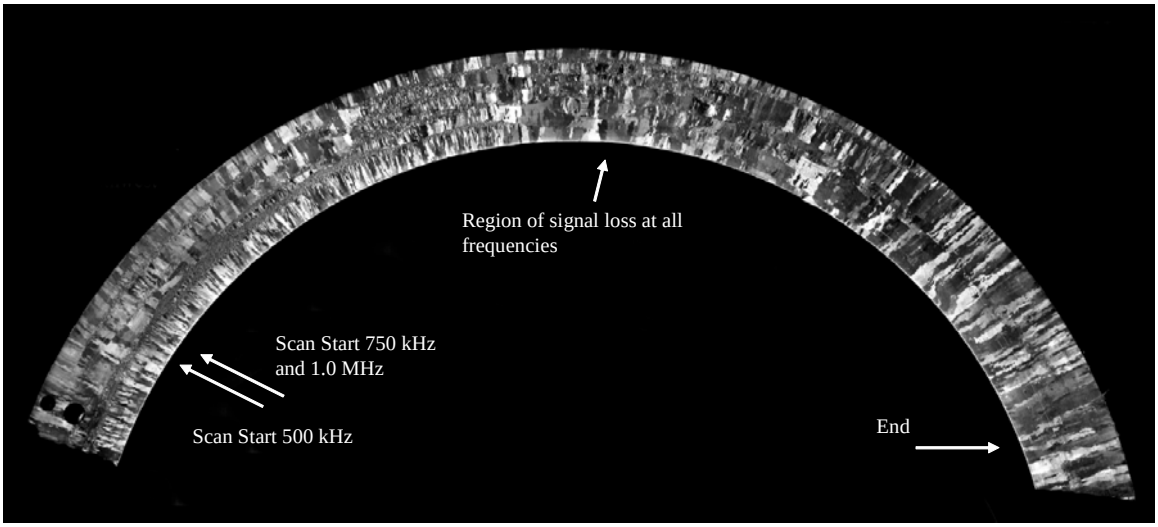

Figure 5.3 Polished and Etched Surface of IHI-SW Segment. Shown are the phased-array scan start and end as well as the approximate region of corner signal loss noted in the 750-kHz and 1.0-MHz scans.

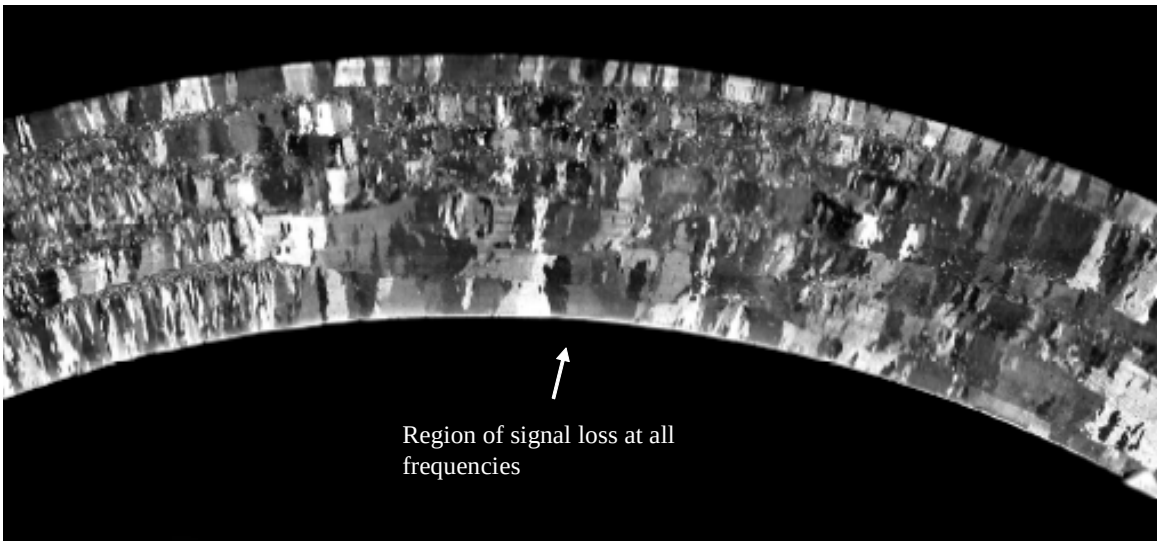

Figure 5.4 Blowup of the Region of Signal Loss

from a stratified region at the start of the scan on the left to a region of columnar grains at the end of the scan on the right of the photo. The data on the Westinghouse segment are similarly shown in Figures 5.5 and 5.6 followed by the data from the EPRI segment in Figures 5.7 and 5.8.

The Westinghouse polished and etched surface appears more columnar throughout the segment, with both the 500-kHz and 1.0-MHz data giving a fairly consistent response. At 750 kHz, the corner signal is not present at the start of the scan, and the data appear much noisier.

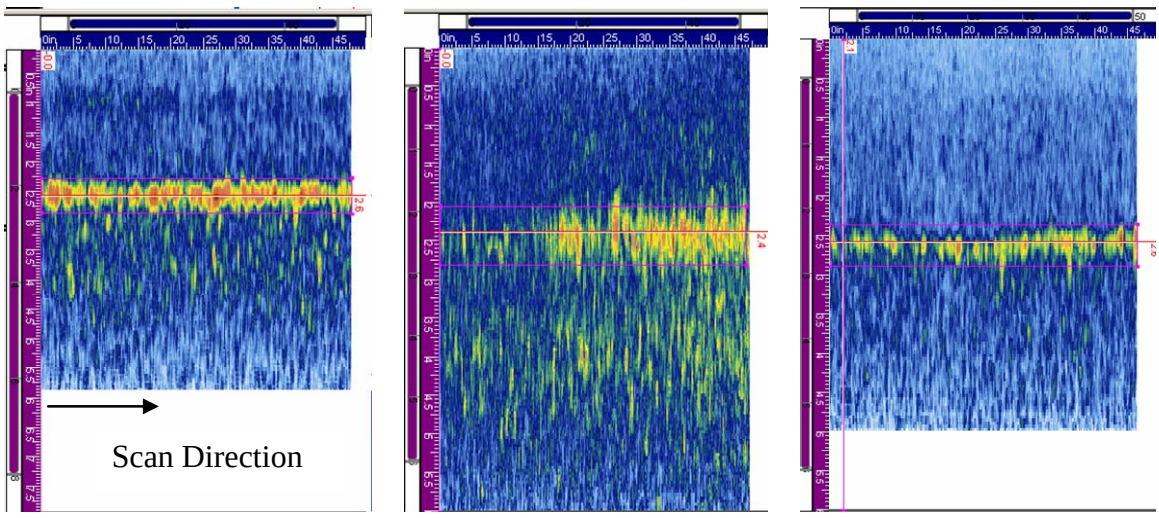

Figure 5.5 Merged B-Scan Views of Westinghouse Segment Corner Signal at 500 kHz (left), 750 kHz (center), and 1.0 MHz (right). Scan length is 121 cm (48 in.), 120 cm (47 in.), and 118 cm (46 in.), respectively.

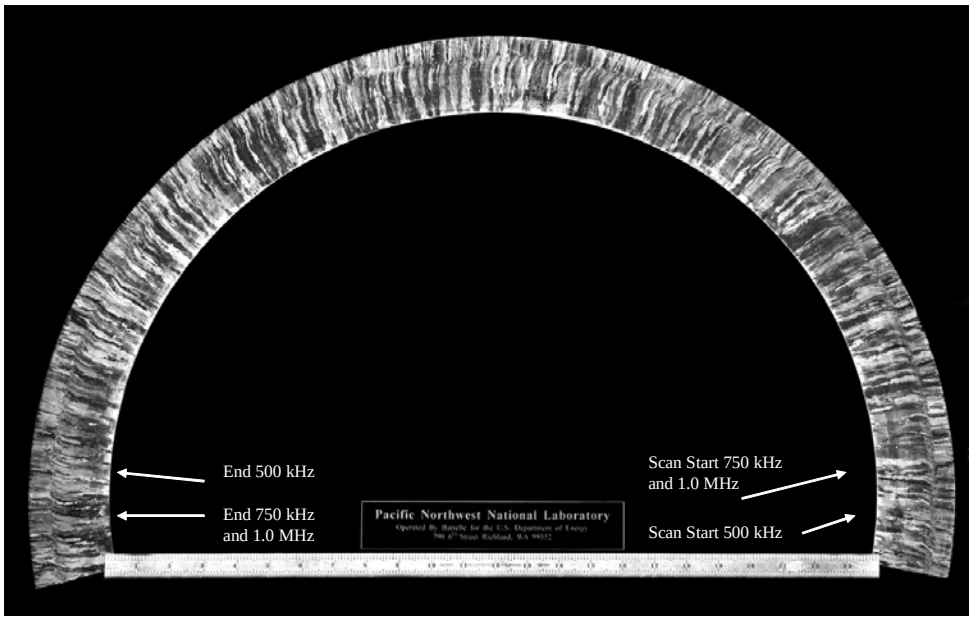

Figure 5.6 Polished and Etched Surface of Westinghouse Segment. Scan start and end points are shown for the 500-kHz, 705-kHz and 1.0-MHz scans.

The EPRI segment appears more equiaxed throughout, yet still produces areas with a weakened or loss of signal at 500 kHz. In this material, the 750-kHz and 1.0-MHz data appear more consistent.

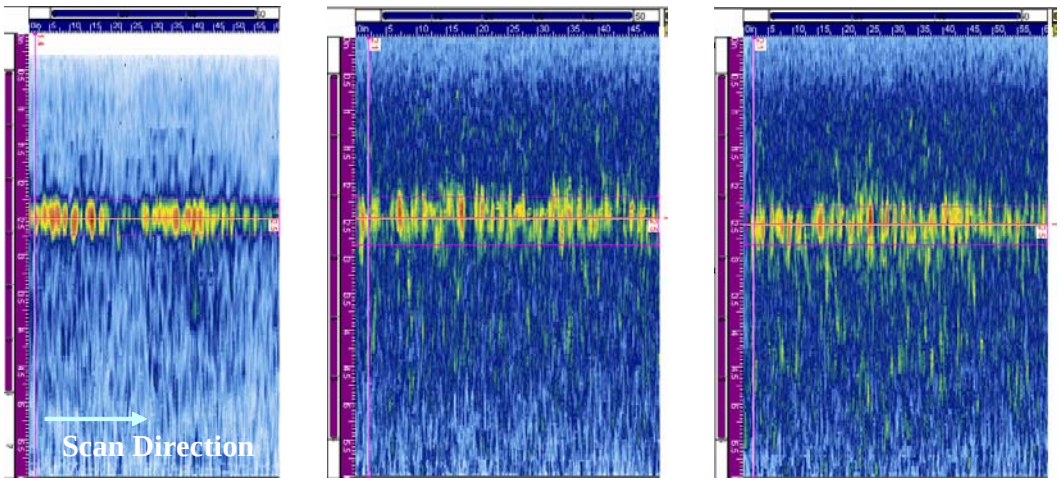

Figure 5.7 Merged B-Scan Views of EPRI Segment Corner Signal at 500 kHz (left), 750 kHz (center) and 1.0 MHz (right). Scan length is 127 cm (50 in.), 155cm (61 in.), and 155 cm (61 in.), respectively.

Figure 5.8 Polished and Etched Surface of EPRI Segment

Overall, this qualitative review indicates the best corner-trap detection performance occurs at 500 kHz, but even at this frequency the corner response is not always detected, thus further confirming the difficulty in ultrasonically examining this material.

To better characterize the material, a signal-to-noise value and a calculation of the normalized length of the corner signal detected for the unflawed CCSS base material listed earlier (vintage pipe segments, WOG, and PNNL specimens) were determined. The view in Figure 5.9 shows the corner signal running vertically through the image for IHI-SW data. A box (ZETEC contour shown in red) is drawn around the corner signal, and the value for the boxed image maximum is displayed. Each data file is normalized by adjusting the gain to give a maximum response of approximately 100% screen height. Additionally a vertical line is positioned in the center of the corner response, and a profile (ZETEC echo-dynamic curve) is drawn to the right of the image. From this profile, the normalized length of material or the percentage of length inspected that exceeds a 50% threshold is manually calculated. This represents corner-signal detection.

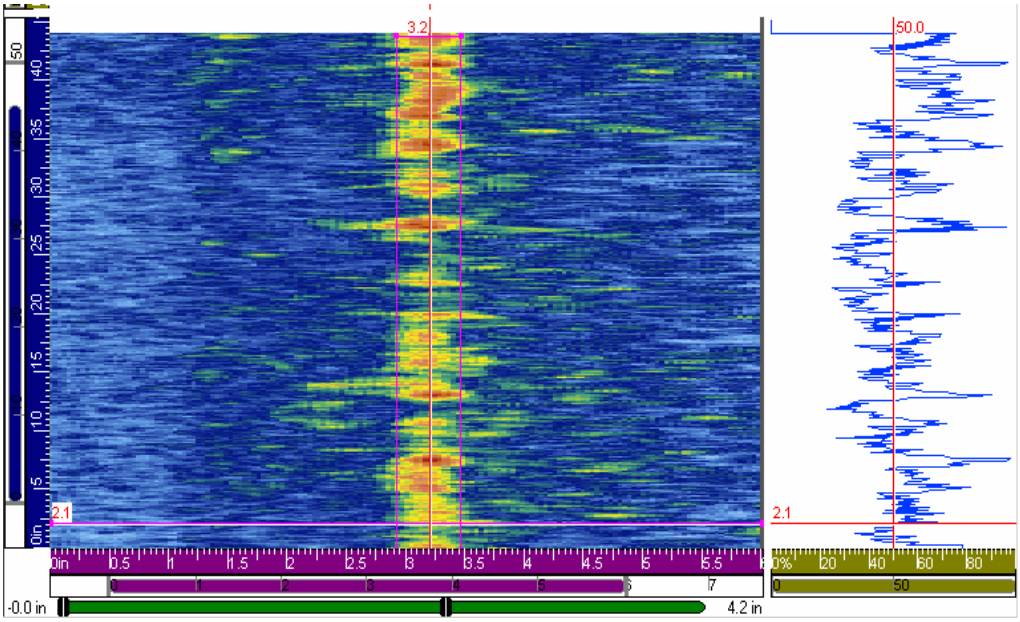

Figure 5.9 Merged B-Scan Image of IHI-SW Segment Corner Response at 500 kHz. Shown are echo-dynamics and amplitude contour mapping.

A similar box and line are drawn in an area representing grain noise in the B-scan view shown in Figure 5.10 for the IHI-SW sample at 500 kHz. The average noise value is determined from this boxed region. The profile line in the noisy region is only used as a visual indication of the noise level. A signal-to-noise value for each specimen at a specific transducer frequency is calculated from the peak signal response and the average noise value. End-of-block corner images of all vintage pipe segments and selected PNNL and WOG specimens investigated are shown in Appendix B. These include the IHI-SW, Westinghouse, EPRI unflawed segments, corner-trap responses from the CCSS pipe side of several WOG specimens, and both the columnar and equiaxed CCSS ends of the PNNL specimens.

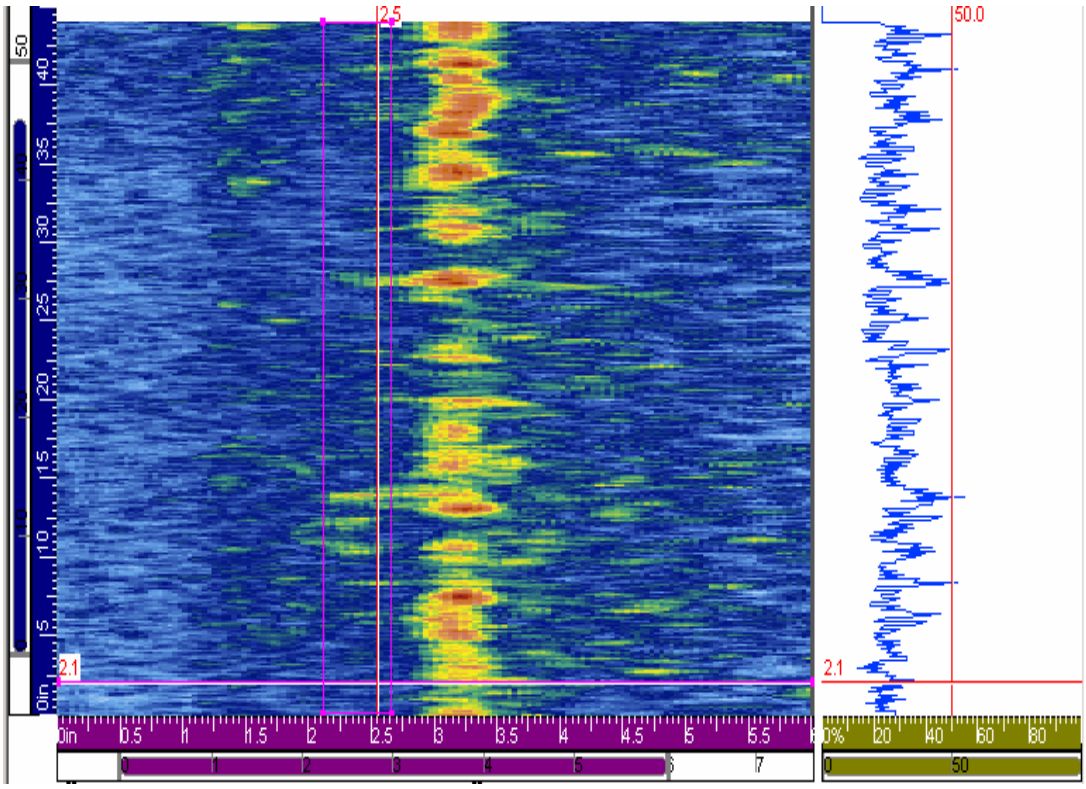

Figure 5.10 Merged B-Scan Image of IHI-Southwest Segment Noise Response at 500 kHz. Shown are echo-dynamics and amplitude contour mapping.

5.2 Low-Frequency/SAFT Base Metal Examination of Unflawed Centrifugally Cast Stainless Steel Material

To augment frequency domain information, corner responses from the IHI-SW and Westinghouse vintage pipe segments and WOG specimens APE-1 and MPE-6 were recorded at an inspection frequency of 400 kHz using the PNNL low-frequency SAFT system. Raster scans were acquired over sections approximately 127 cm (50 in.) long in the three vintage pipe segments and sections 23-30 cm (9-12 in.) long on the two WOG specimens.

The data acquisition setups for the Westinghouse and IHI-SW piping segments and the WOG specimens are shown in Figures 5.11 and 5.12, respectively. With a pitch-catch configuration for data collection for these evaluations, the transducer was positioned on the surface of the components, and radio frequency (RF) ultrasonic data were collected. As the transducer was scanned over the surface, the A-scan record (RF waveform) was amplified, filtered, and digitized on a predetermined spatial grid. The corner-trap responses produced a collection of echoes in the A-scan records. The unprocessed or RF data sets were then post-processed using the SAFT algorithm, invoking a variety of full beam-processing angles (between 8º and 24º).

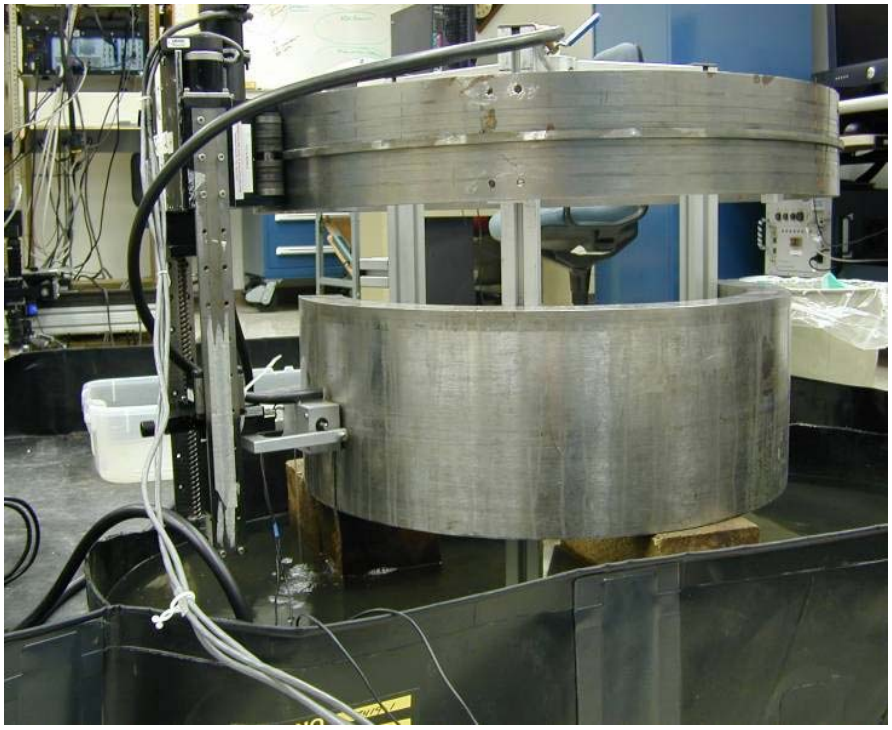

Figure 5.11 Low-Frequency Scan Apparatus for Westinghouse and IHI-Southwest Segments

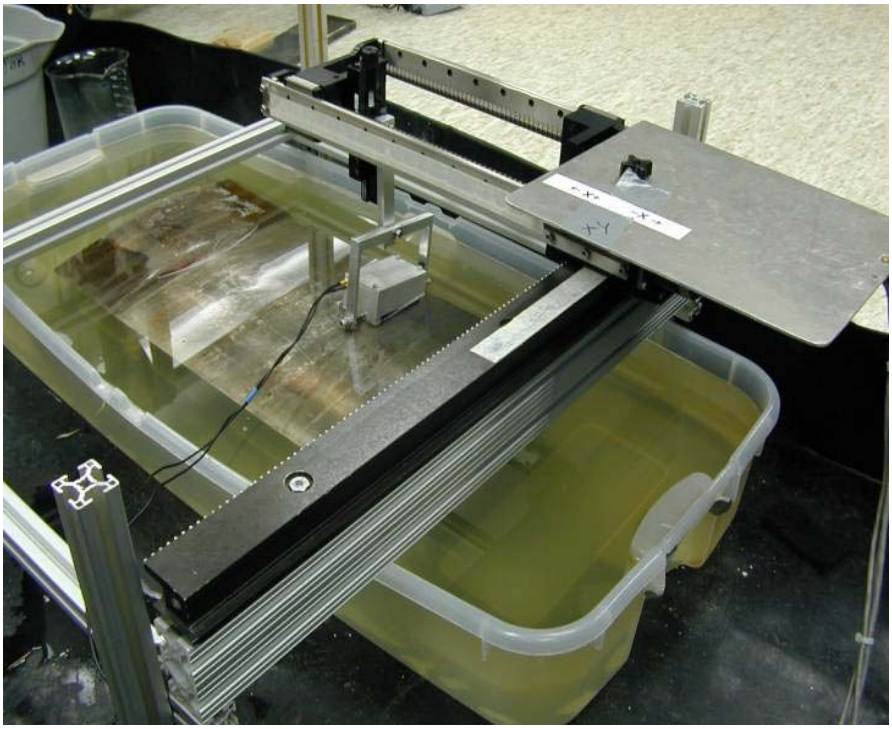

Figure 5.12 Low-Frequency Scan Apparatus for WOG Specimens

The automated pipe scanner was used for accurate and smooth scanning of the search unit through a specified number of grid points in the *x,y* plane while maintaining low noise conditions and a constant coupling of the transducer to the surface. The pipe scanner was configured with tailored gimbals for transducer attachment and smooth and effective translation over the surface of the specimens. A specially fabricated drip line attached to a couplant reservoir with a peristaltic pump provided a constant stream of water on the specimen surface for improved coupling and transducer motion.

The relationship between echo location in the series of A-scans and the actual location of the corner traps of the specimens makes it possible to reconstruct a high-resolution, enhanced signal-to-noise ratio image from the acquired raw data.

Six scans were acquired at 400 kHz for the vintage piping segments and WOG specimens shown below:

1. Westinghouse large-grained CCSS top corner trap
2. Westinghouse large-grained CCSS bottom corner trap
3. IHI-SW large-grained CCSS top corner trap
4. IHI-SW large-grained CCSS bottom corner trap
5. WOG APE-1 corner trap on the pipe side
6. WOG MPE-6 corner trap on the pipe side.

The top and bottom corner traps of the Westinghouse and IHI-SW large-grained CCSS segments were scanned from the outer diameter surfaces, thus imaging the inner-diameter corner traps of the segments. To scan the top and bottom corner traps of the Westinghouse and IHI-SW segments, PNNL simply flipped over the segments. Only the 6.6-cm (2.6-in.) thick pipe ends on the CCSS side of each WOG specimen were accessible and scanned. Surface conditions impacted probe coupling and prevented the opposite ends (SCSS) of the WOG specimens from being scanned.

In the images post-processed with SAFT, the corner trap response was easily identifiable based on signal intensity and axial and circumferential positioning. The corner-trap response and a reasonable amount of surrounding area were selected in the B-scan side view image (see Figure 5.13), isolated, and normalized relative to the maximum amplitude within the selected region.

The B-scan end view of the selected region was then displayed (see Figure 5.14), and the axial and circumferential positioning of the corner trap response was once again verified to be correct based on time-of-flight calculations and spatial positioning within the scan image.

To quantify the signal-to-noise ratio, a single line of data above the corner-trap response and a single line of data below the corner trap response in the B-scan end view of the selected region were sampled and averaged to compute the noise value. The line of data above the corner-trap response was as close to the corner trap response as possible without including data from the corner-trap echo response itself. A line of data essentially later in time, or after the corner-trap response, was chosen in the same manner. The maximum amplitude of the corner-trap response

itself was used for the signal value. The signal value was divided by the average noise value to determine the signal-to-noise ratio.

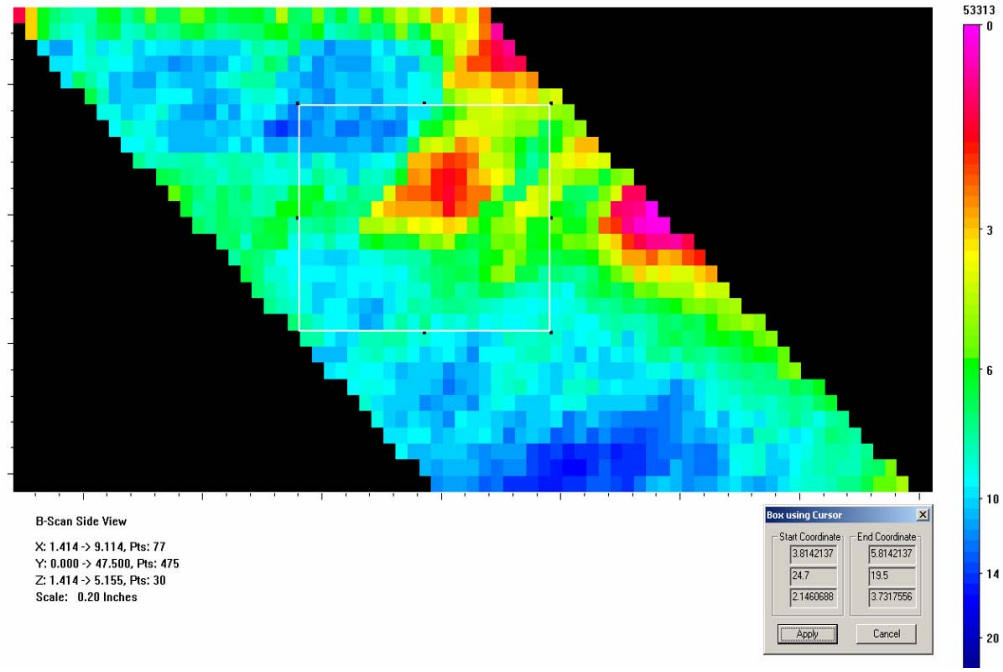

Figure 5.13 Corner Trap Selected Area Outlined in White Box Shown in B-Scan Side View (25.4 mm = 1.0 in.)

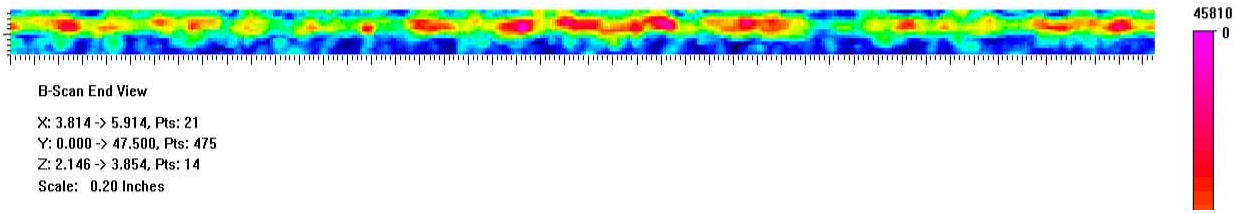

Figure 5.14 B-Scan End View of Corner Trap Selected in B-Scan Side View (25.4 mm = 1.0 in.)

To quantify the detection percentage of the corner trap, a 6-dB clip was performed in the B-scan end view to eliminate all data below 6 dB relative to the maximum amplitude within the selected region (see Figure 5.15). The remaining data in the B-scan end view that were in the correct axial and circumferential location within the scan were summed. This circumferential coverage divided by the total circumferential length was calculated to determine the detection percentage (linear scan length of the corner trap that was detected).

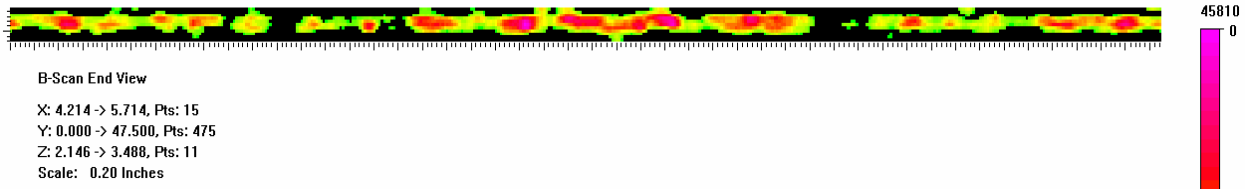

Figure 5.15 Results of 6-dB Clip Used in B-Scan End View (25.4 mm = 1.0 in.)

The 16º beam SAFT processing angle was used for analysis purposes, because processing angles greater than 16º did not significantly improve image enhancements and processing angles smaller than 16º did not provide the necessary focusing and signal-to-noise ratio enhancements to the imaged data. It should be noted that the SAFT presentation images are defaulted in the software to use dimensions in English units only. Summary analysis documentation for all corner-trap responses can be found in Appendix B.

The data acquired were evaluated by determining the detection percentage of the corner trap and the signal-to-noise ratio, as previously described. The results are summarized in Table 5.1.

Table 5.1 Low-Frequency/SAFT Corner-Trap Detection

Segment/Specimen	Corner Trap	Detection (%)	Average Signal-to-Noise Ratio
Westinghouse	Top corner trap	98	2.72
	Bottom corner trap	95	2.36
IHI-Southwest	Top corner trap	75	2.41
	Bottom corner trap	76	2.47
WOG APE-1	Corner trap	89	1.62
WOG MPE-6	Corner trap	90	2.18

A review of Table 5.1 shows that the detection percentage of the corner trap is a function of the sample thickness. The computed signal-to-noise values are above a 2:1 ratio (6 dB) for all scans except for the corner-trap scan for WOG specimen APE-1, which had a signal-to-noise value of 1.62 (4.17 dB).

5.3 Combined Results for Centrifugally Cast Stainless Steel Baseline Material

The signal-to-noise values for the specimens inspected with the PA and 400-kHz transducers are shown in Figure 5.16. Because of noise variation between specimens, the peak responses of the corner signals were normalized to nearly 100% screen height. Signal-to-noise ratio values for almost all the specimens were greatest with the 500-kHz PA probe, and at this frequency the lowest signal-to-noise value was 3.7 (11.4 dB), well above a minimal value of 2 (6 dB) for a

good detection call. The 750-kHz probe performed the worst of the PA probes and had a low of 2.2 (6.85 dB) on sample MPE-3. The 1.0-MHz probe lowest signal-to-noise value was 2.8 (8.94 dB) on specimens APE-1 and POP-7. Average signal-to-noise values were 5.7, 3.1, and 3.4 (15.1, 9.83, and 10.63 dB) for the three PA probes with increasing

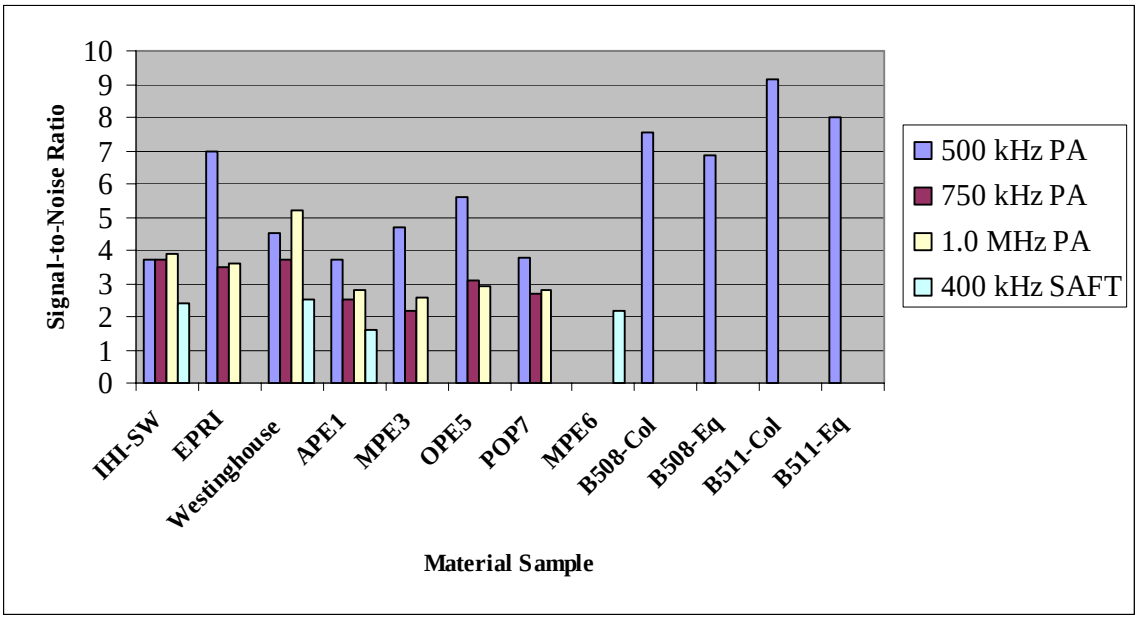

Figure 5.16 Signal-to-Noise Values for CCSS Base Material As Determined from Examining Specimen End (Corner-Trap Response)

frequency. The average signal-to-noise value for the low-frequency/SAFT probe was 2.2 (6.85 dB), putting its performance below that of the PA probes. It should be noted that the low-frequency/SAFT signal-to-noise values were calculated in a manner similar to that used on the PA data, but the results are thought to be conservative. Although these values are useful, they do not represent the influence of the presence or absence of the corner signal that is seen in this large-grained material over a scanned region.

To quantify the presence or absence of the corner signal, the segment length exceeding a 6-dB threshold (i.e., corner signal present at 50% of screen height or greater) was determined and is shown in Figure 5.17. As with the signal-to-noise analysis, the corner response had the best detection among the PA probes at 500 kHz, and with the 1.0 MHz probe slightly better than the 750 kHz data. Average detected lengths of the corner signal for the three frequencies are 84%, 52%, and 55%. It is possible to fully detect the corner signal as the data from OPE-5 and the PNNL specimens indicate (see Appendix B). The low-frequency/SAFT data was superior to the PA data in the three direct comparisons and one indirect comparison (MPE-3 to MPE-6) and had an average detected corner rate of 88%.

To combine the signal-to-noise and detected corner-response evaluations, another analysis step applied the detected corner-length fractional values as a weighting factor to the previously

calculated signal-to-noise values (maximum signal divided by the average noise multiplied by the length factor), with results as shown in Figure 5.18. The 500-kHz PA clearly outperformed the other frequencies, with the exception of the POP-7 specimen where results are similar. The average weighted signal-to-noise values for the three PA frequencies are 5.1, 1.6, and 1.8 (14.2, 4.08, and 5.11 dB). The low-frequency/SAFT data produced an average weighted signal-to-noise value of 1.9. This weighted value implies that the 500-kHz PA probe produces the best results by giving a higher signal-to-noise ratio over a unit length of inspected material.

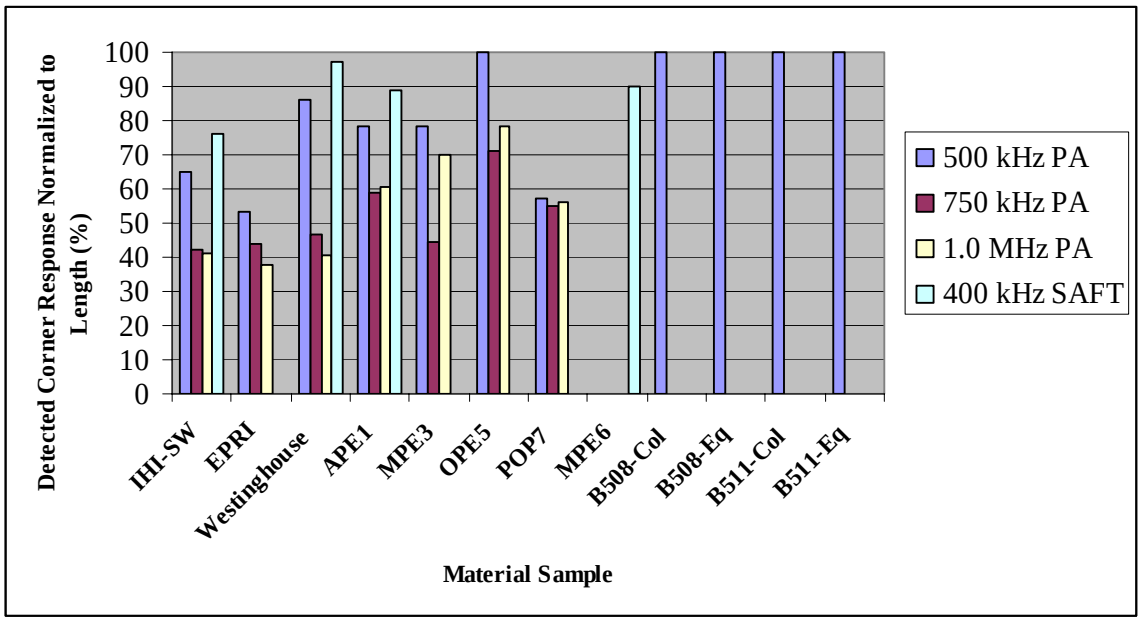

Figure 5.17 Detected Corner Response Values for Base Material As Determined from Inspecting End of CCSS Specimens

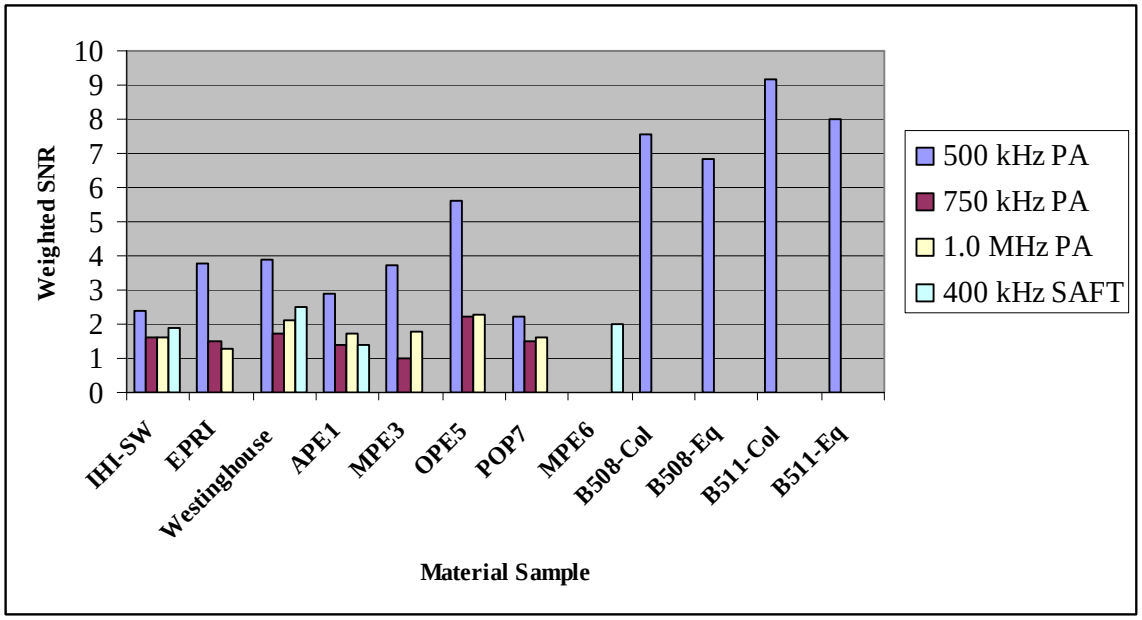

Figure 5.18 Weighted Signal-to-Noise Ratio for Base CCSS Specimens. The ratio has been weighted by the corresponding corner signal detection factor.

In general, the low-frequency/SAFT percentage of detection is greatest for those specimens that were examined at all the inspection frequencies. However, low-frequency/SAFT signal-to-noise value is lower in comparison to the signal-to-noise ratio for the higher PA inspection frequencies. This can perhaps be explained by the fixed 45° inspection angle of the 400-kHz transducer and the use of piezo-composite elements in the arrays; the phased array explores a range of inspection angles from 30° to 60° for improved signal-to-noise ratios, and higher pulse generation efficiencies are gained with composites.

As shown in Figure 5.17, 500-kHz PA and 400-kHz SAFT provided the highest percentage of corner trap detections in base CCSS materials. Also shown are short regions of diminished response below a 2:1 signal-to-noise ratio (–6 dB) along the scan length of the specimens. Some of this signal loss may be attributed to varied coupling conditions on individual specimens. However, it is believed that significant grain size variations and anisotropy are the primary factors in these regions of diminished response, which could potentially lead to flaws remaining undetected in limited areas of CCSS material welds in the field. PNNL measured each of these short regions of diminished response to understand how this might affect flaw detection, as a function of overall flaw length. A listing of the total number observed for each specimen, along with length (minimum, maximum, average, and median) of corner-trap signal-loss regions, is shown in Table 5.2 for the 500-kHz PA and 400-kHz SAFT probes.

Table 5.2 Regions of Diminished Signal Strength in Baseline CCSS Specimens

Specimen	Probe	Number of Regions Observed	Measured Length of Diminished Signal Regions			
			Minimum	Maximum	Average	Median
EPRI	PA	21	0.25 cm (0.10 in.)	11.43 cm (4.50 in.)	3.57 cm (1.41 in.)	2.29 cm (0.90 in.)
IHI-SW	SAFT	9	0.51 cm (0.20 in.)	10.92 cm (4.30 in.)	3.30 cm (1.30 in.)	2.29 cm (0.90 in.)
	PA	27	0.25 cm (0.10 in.)	6.10 cm (2.40 in.)	1.55 cm (0.61 in.)	1.02 cm (0.40 in.)
Westinghouse	SAFT	4	0.25 cm (0.10 in.)	2.79 cm (1.10 in.)	1.02 cm (0.40 in.)	1.02 cm (0.40 in.)
	PA	26	0.25 cm (0.10 in.)	3.05 cm (1.20 in.)	0.75 cm (0.30 in.)	0.51 cm (0.20 in.)
APE-1	SAFT	1	2.79 cm (1.10 in.)	2.79 cm (1.10 in.)	2.79 cm (1.10 in.)	2.79 cm (1.10 in.)
	PA	4	1.02 cm (0.40 in.)	3.05 cm (1.20 in.)	1.78 cm (0.70 in.)	1.52 cm (0.60 in.)
MPE-3	PA	5	0.25 cm (0.10 in.)	2.54 cm (1.0 in.)	0.91 cm (0.36 in.)	0.51 cm (0.20 in.)
MPE-6	SAFT	2	1.02 cm (0.40 in.)	1.27 cm (0.50 in.)	1.27 cm (0.50 in.)	1.27 cm (0.50 in.)
OPE-5	PA	0	0	0	0	0
POP-7	PA	4	0.25 cm (0.10 in.)	4.32 cm (1.70 in.)	1.97 cm (0.78 in.)	1.65 cm (0.65 in.)

In the worst cases, 500-kHz PA probe data exhibited a region of significant signal loss in the EPRI piping segment of 11.4 cm (4.50 in.) in length while 400-kHz SAFT data had a similar 10.9-cm (4.3-in.) area on the IHI-SW segment. These worst-case values in the data are not caused by coupling irregularities as evidenced by the consistent signal amplitudes in the B-scan images in the region before (earlier in time) the corner response. This then suggests that the signal loss is due to CCSS microstructural effects. A more appropriate loss-of-signal region length is shown by the median values in Table 5.2. The largest of the median values is on the order of 2.8 cm (1.1 in.), which indicates that flaws smaller than this length occurring in areas of coarsest grain structure may not be detected reliably. However, CSS materials are thought to be relatively flaw-tolerant with critical crack sizes on the order of 50% through-wall in depth and extending 180° in circumference having been postulated (Diaz et al. 1998). Therefore, even if one assumes the worst-case signal-loss value, these regions are a small fraction of the critical flaw length and it is expected that any flaws of significance would be detected reliably. It should also be noted that some CCSS materials exhibited very small regions of diminished signal. WOG specimen MPE-3 and the Westinghouse piping segment displayed median values of 0.51 cm (0.20 in.), while WOG specimen OPE-5 showed no areas of signal loss.

Previous work with CCSS specimens has shown that large variations in grain sizes and layered structures existing in vintage CCSS materials would cause UT beam reflection and scattering,

resulting in coherent noise responses that could be misinterpreted as flaws.[4] Yet during this study it was observed that 500-kHz PA data did not exhibit baseline material ultrasonic noise responses that might lead to high false call rates. As an example of this observation see the images in Figure 5.19. The end-of-block corner signal from the Westinghouse piping segment was recorded and a line scan performed farther away so as not to display the corner response. The offsets from the end of the segment were 7.6 cm (3 in.) and 20.3 cm (8 in.) for the corner and noise signals, respectively. Note that the Westinghouse segment was the only material with sufficient axial length to enable collection of only baseline material data with no responses from geometry such as corner reflectors.

The images in Figure 5.19 display the corner-trap response on the left and the inherent background material noise on the right. Both images were acquired with the same metal path and gain setting. All noise indications had responses that were less than 6 dB of the corner trap and are on the order of 0.5 cm (0.2 in.) in length. It is expected that qualified data analysts would correctly identify these small signals as non-flaws because of their low amplitude and short length.

Images from the flawed WOG specimens show a different result. It appears that responses from geometrical sources such as counterbore may provide signals that could more easily lead to potential false calls. This will be discussed further in Section 6.

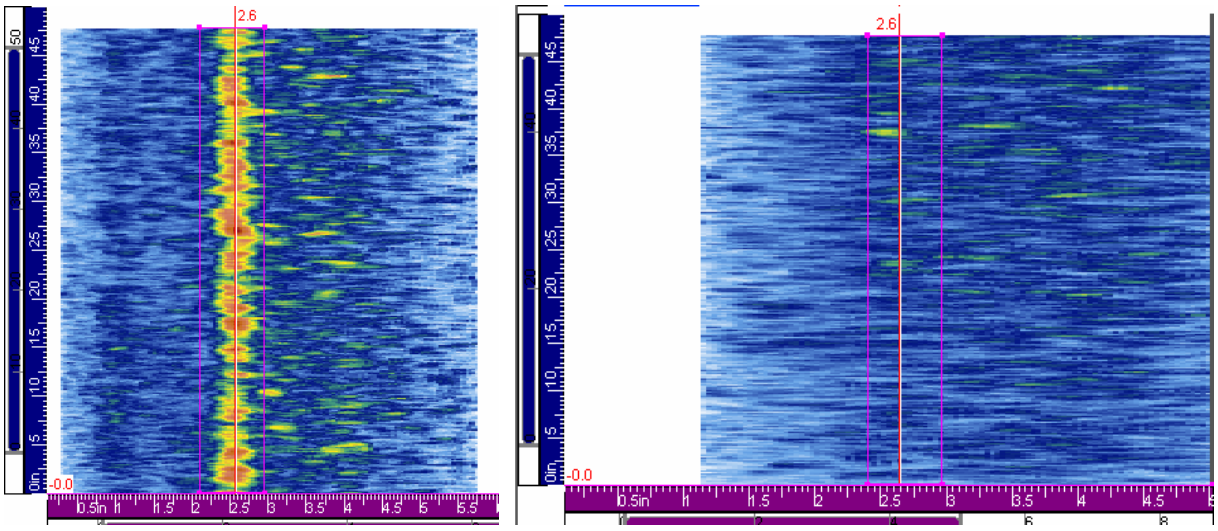

Figure 5.19 CCSS Material Noise Scans. The corner response from the Westinghouse piping segment is shown on the left; baseline noise with no geometrical reflectors is shown on the right. Scan length was 127 cm (50 in.) at 500 kHz.

([4]) Diaz, Harris, and Doctor. Unpublished. *Field Evaluation of Low Frequency SAFT-UT on Cast Stainless Steel and Dissimilar Metal Weld Components*. Submitted to the NRC.

6 Crack Detection and Characterization in Flawed Specimens

This section documents the detection and characterization of cracks in the Westinghouse Owners Group (WOG) and PNNL specimens containing flaws.

6.1 Flaw Detection

The WOG specimens were examined with 500-kHz, 750-kHz, and 1.0-MHz phased arrays from both sides of the weld. PNNL specimens were examined at 500 kHz only. Figure 6.1 shows the typical laboratory setup for data acquisition. Multiple line scans with beam direction perpendicular to the weld and scan direction parallel to the weld were acquired at varied distances from the weld centerline to create a comprehensive dataset. Delay laws were calculated to focus the sound field at approximately 60 mm (2.4 in.) into the material, and the insonification angle was swept from 30° to 60° in increments of 1°. Access to the flawed region from the safe-end side of the weld was restricted on ONP-type specimens due to the outside surface geometry of the nozzle-side of the mockup. Flaw length and through-wall dimensions were provided in WOG and PNNL documentation accompanying the specimens. However, because the processes used to make the cracks are not exact, and NDE is not capable of reliably characterizing cracks in these materials, true flaw sizes are unknown, and the documented values represent best engineering judgment with large uncertainty.

Figure 6.1 Laboratory Setup for Phased Array Data Acquisition on Westinghouse Owners Group Specimens

The data were analyzed with a priori knowledge of the approximate location of each flaw relative to side of the weld and position along the weld. This study was not intended to be a blind performance demonstration but an assessment to determine the performance of low-

frequency phased array technology in these coarse-grained materials. Based on analyses of data collected in this study, flaw detection involves several considerations and inspection parameters including inspection frequency, side of weld inspected (i.e., near- or far-side of weld), signal-to-noise ratio, flaw area available for specular response, flaw location, flaw type, and signal discrimination in multiple images. As shown by the analysis of end-of-block corner-trapped responses (discussed in Section 5), acoustic scattering and beam redirection of certain microstructures may cause even the largest flaws to diminish over portions of their length. Therefore, large flaws thought easier to detect may be mischaracterized, and small flaws thought difficult to detect are potentially adequately imaged, depending on the microstructures present around the flaw location.

In the analyses, data files were merged and displayed in volume-corrected (VC) top (C-scan) views, VC end (D-scan) views, and VC side (B-scan) views as shown in Figure 6.2. Merged images represent an integration or compilation of the data collected over the 30° to 60° of insonification and scan length, Y, with the peak response recorded at a specific spatial position in X (insonification direction), Y (scan direction), and Z (depth, or time). The advantage of merged data is that signals with continuity in length and depth, such as inside surface counterbore or flaws, will be detected at multiple positions and thus ideally present a better connected or "filled-in" response. The alternative is to analyze limited cross-sectional data in the side view as one scrolls through the angles in the volume-corrected sector scan. This technique is also valuable for analyzing individual responses from flaws but requires more time scrolling through the data and could potentially lead to a missed call if used as the primary method of analysis.

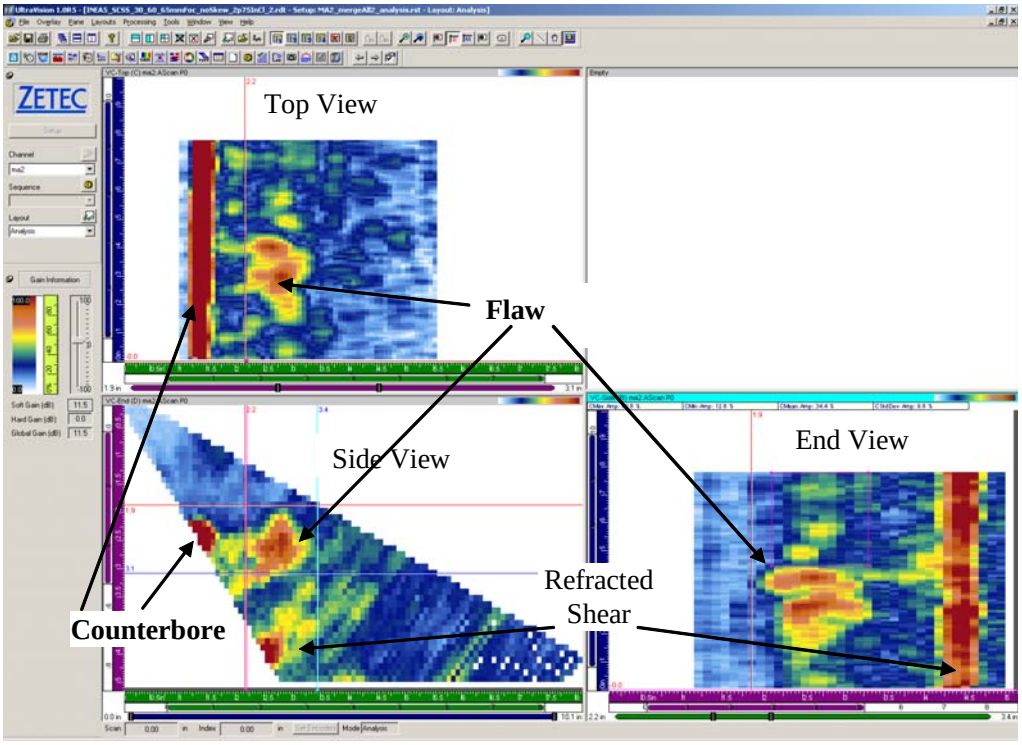

Figure 6.2 Merged Data File Showing Top, End, and Side Views for Longitudinal Inspection Mode

In the merged data in Figure 6.2, the region containing the flaw response is boxed in the side view to remove the counterbore signal and other signals outside the area of interest in the end or top view images. The vertical lines determine the region of data displayed in the end view, and the horizontal lines determine the data region displayed in the top view. A large counterbore signal is typically seen in the data and is best removed in the end view, making the side view and the end view the favored views for data analysis.

An easily detected flaw, a 30% through-wall mechanical fatigue crack on the CCSS side of the weld in WOG specimen MPE-3 as imaged from the SCSS side, is shown in Figure 6.3 for the three inspection frequencies. Flaw analysis generally involves locating the counterbore signal as a reference point and examining the adjacent regions for a flaw signal. A saturated counterbore signal on the left edge of the side view in Figure 6.3 is evident at all three frequencies. The flaw signal is to the right of the counterbore signal and is strong compared to background noise. The signal appearing later in time is a refracted shear response and is ignored.

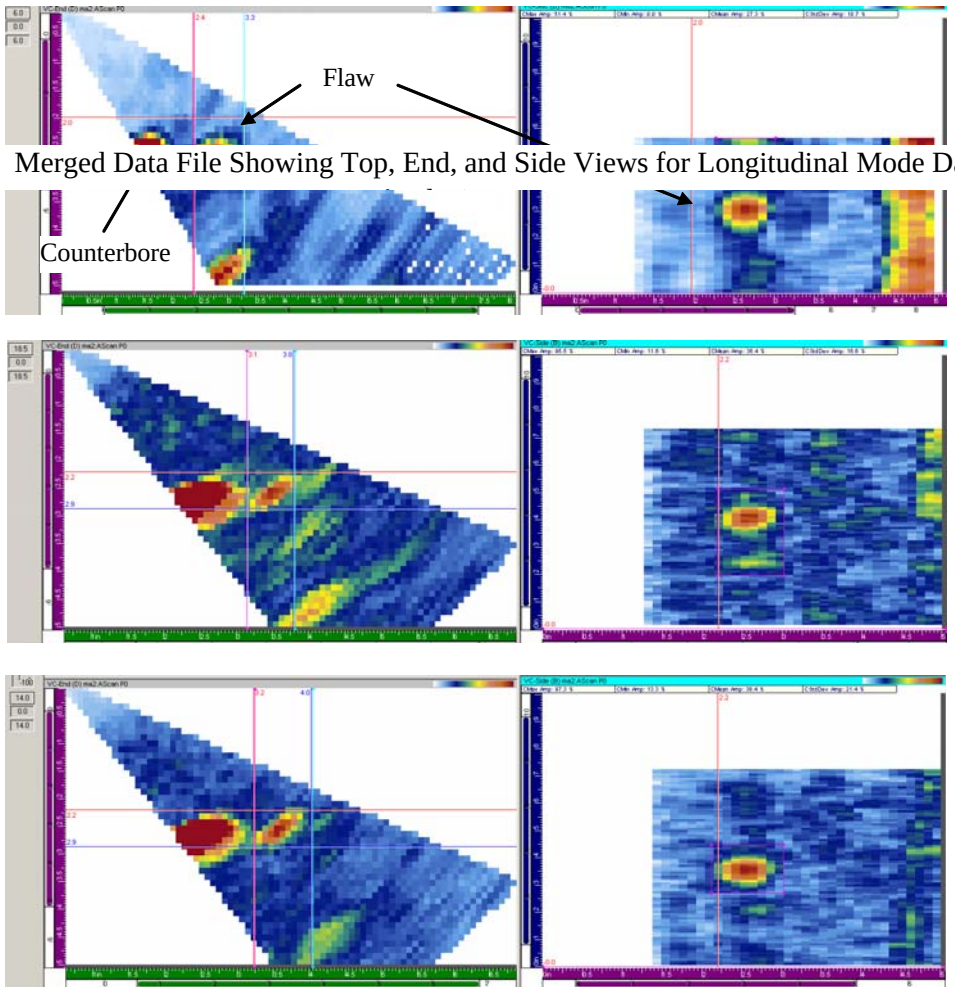

Figure 2 Merged Data File Showing Top, End, and Side Views for Longitudinal Mode Data

Figure 6.3 MPE3 SCSS Merged Data at 500 kHz, 750 kHz, and 1.0 MHz, Top to Bottom. The flaw is detected at all three frequencies.

A marginally detected flaw is shown in Figure 6.4. This is an approximately 28% through-wall thermal fatigue crack on the safe-end side of the weld in WOG specimen ONP-3-5 as viewed from the CCSS side of the weld. Again, the detection keyed in on the counterbore signal, when present, and adjacent regions, observing possible responses in the center of the scanned data. A possible counterbore signal is seen on the left edge of the side view. The signal to the right is boxed as a possible flaw because it shows slight separation from the counterbore signal. An end view image of the boxed region is shown in the right side of Figure 6.4 and shows a signal of interest near the center of the scanned length. However, a marginal call is made due to the poor signal-to-noise value (approximately 2:1) and minimal length associated with the signal.

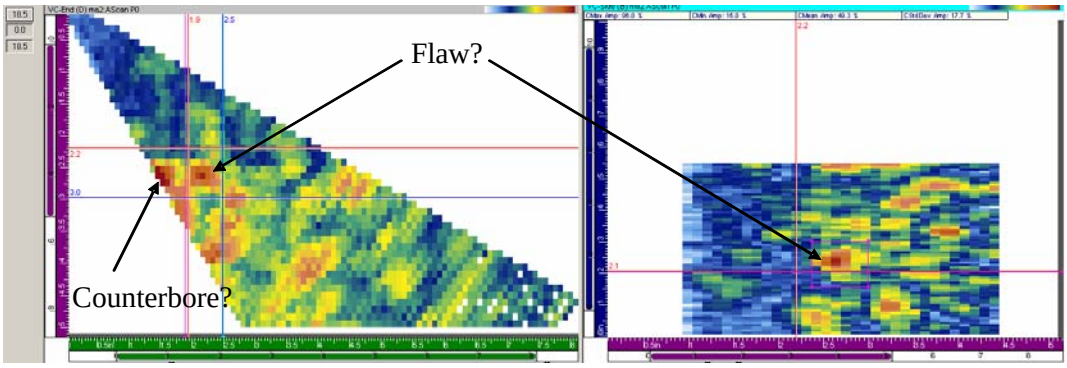

Figure 6.4 Thermal Fatigue Crack in ONP-3-5 As Viewed from CCSS Side at 500 kHz Judged To Be Marginally Detected

An example of a flaw judged to be undetected is shown in Figure 6.5. This is an approximately 30% through-wall mechanical fatigue crack in specimen MPE-3 as viewed from the CCSS side of the weld using the 1.0-MHz array. Note that this flaw was shown previously as easily detected from the SCSS side (see Figure 6.3). There was no counterbore signal in the data from the CCSS side of the weld, and a possible flaw signal shown boxed in the side view (left side image) did not correspond to any signal with length in the end view (right side image).

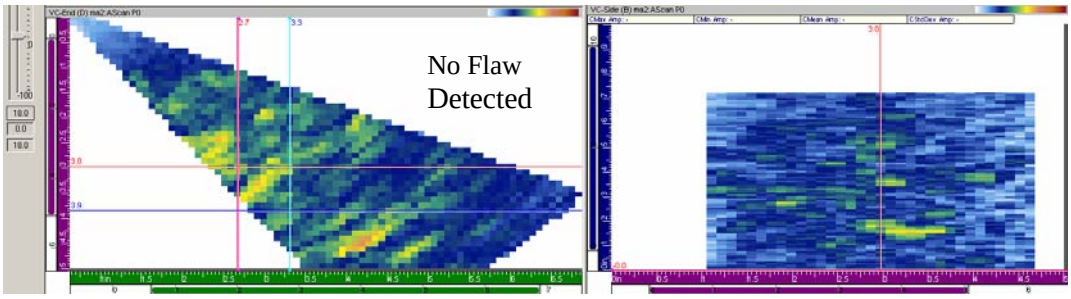

Figure 6.5 Mechanical Fatigue Crack in Specimen MPE-3 As Viewed from CCSS Side at 1.0 MHz Judged To Be Not Detected

A summary of the detection calls is shown in Table 6.1 where the flaws are listed by descending flaw specular area available for reflection. For simplicity, the flaw area calculation assumed a

rectangular flaw profile. Appendix C shows the end and side view images for all analysis results listed in Table 6.1.

Table 6.1 Detection of WOG and PNNL Flaws Listed by Flaw Specular Area

WOG Specimen ID	Side UT Applied[a]	Crack Type[b]	Flaw Through-wall Depth[c] (%)	Flaw Area[d] (cm^2)	Flaw Detection Results[e]		
					500 kHz	750 kHz	1.0 MHz
INE-A-1	SCSS[f]	MF	42	18.5	Yes	Yes	Yes
POP-7	CCSS	MF	31	17.4	Yes	No	Yes
	SCSS[f]				Yes	Yes	Yes
B504	CCSS-Col.	TF	48	17.2	Yes		
	CCSS-Eq.[f]				Yes		
INE-A-5	SCSS	MF	34	17.1	Yes	Yes	Yes
MPE-3	CCSS	MF	30	17.1	Yes	No	No
	SCSS[f]				Yes	Yes	Yes
B519	CCSS-Col.	TF	46	15.9	Marginal		
	CCSS-Eq.[f]				Yes		
INE-A-4	SCSS[f]	TF	29	12.7	Yes	Yes	Yes
ONP-3-5	CCSS	TF	28	11.7	Marginal	No	No
ONP-D-2	CCSS[f]	TF	28	11.7	Marginal	Yes	Marginal
OPE-5	CCSS	TF	23	10	Yes	Marginal	Marginal
	SCSS[f]				Yes	Yes	Yes
B508	CCSS-Col.[f]	TF	33	9.4	No		
	CCSS-Eq.				No		
ONP-3-8	CCSS	MF	28	9.1	Marginal	Yes	Marginal
MPE-6	CCSS	TF	18	8.8	Yes	Yes	Marginal
	SCSS[f]				Marginal	No	No
POP-8	CCSS[f]	TF	18	8.6	Marginal	Marginal	Yes
	SCSS				Yes	Marginal	Marginal
B501	CCSS-Col.	TF	34	5.8	Marginal		
	CCSS-Eq.[f]				Yes		
OPE-2	CCSS	MF	18	5.4	Yes	Yes	Yes
	SCSS[f]				Yes	Yes	Yes
APE-4	CCSS	MF	14	5.4	Yes	Yes	Yes
	SCSS[f]				Yes	No	No
ONP-D-5	CCSS[f]	MF	18	4.6	Yes	Marginal	Marginal
APE-1	CCSS	MF	13	4.5	Yes	No	Marginal
	SCSS[f]				Yes	Yes	Yes
B515	CCSS-Col.	TF[g]	25	4.4	Yes		
	CCSS-Eq.[f]				Yes		
B505	CCSS-Col.	notch	10	3.5	Yes		

WOG Specimen ID	Side UT Applied[a]	Crack Type[b]	Flaw Through-wall Depth[c] (%)	Flaw Area[d] (cm^2)	Flaw Detection Results[e]		
					500 kHz	750 kHz	1.0 MHz
	CCSS-Eq.[f]				Yes		
B520	CCSS-Col.[f]	TF	16	2.6	Yes		
	CCSS-Eq.				No		

Notes and Definitions:

(a) Denotes from which side of the weld the PA UT was applied; CCSS = centrifugally cast stainless steel, SCSS = statically cast stainless steel, CCSS-Col. = columnar grain structure, CCSS-Eq. = equiaxed grain structure

(b) MF = mechanical fatigue; TF = thermal fatigue

(c) Flaw depth information provided with WOG and PNNL specimens

(d) Assume rectangular aspect ratio using depth and length information to show potential area available for specular reflections

(e) Determination based on image quality and S/N; Yes = clearly detected with > ~2:1, No = not detected, Marginal = Marginal detection with ≤ ~2:1 ratio

(f) Denotes side of weld on which flaw is located

(g) TF crack was bent open then closed

These data were used for determination of flaw detection and length sizing. Occasionally, a single angle or plane view of the data (i.e., unmerged data) provided a better representation of the flaw and was used in the analysis instead of the merged data.

The tabulated results (Table 6.1) suggest that flaw detection is best accomplished with the 500-kHz array. Cumulative flaw detection is 71% for the given flaw types, depths, and materials. At 750 kHz, the detection rate drops to 57%, and at 1.0 MHz, the overall detection rate is 52%.

Another interesting fact as shown by the information in Table 6.1 is that thermal cracks in these specimens are clustered in a range of approximately 20-30% through-wall for WOG specimens. These thermal fatigue cracks represent the mid-range of all flaws and yet appear to cause the most difficulty in detection. Even the smaller mechanical fatigue cracks are generally detected. Typically, cracks produced by the thermal fatigue process are tighter and more faceted than mechanical fatigue cracks, making them more difficult to detect ultrasonically, as the data in this study confirm. Table 6.2 lists flaw detection rates by phased array frequency as a function of flaw type. For all three frequencies applied, there is a marked decrease in detection rate for the thermal fatigue cracks as compared to mechanical fatigue cracks.

Table 6.2 Detection of Flaws by Type of Flaw

	Flaw Detection by Crack Type (%)		
Frequency	**Mechanical Fatigue**	**Thermal Fatigue**	**Combined**
500 kHz	93	57	71
750 kHz	64	44	57
1.0 MHz	64	33	52

Another perspective on low-frequency phased array performance is shown in the bar chart of Figure 6.6, where detections as a function of the side of the weld on which the ultrasound is applied are given for the three phased array examination frequencies for WOG data only. Examinations through SCSS materials, whether the flaw is on the near- or far-side of the weld, are more easily detected than are flaws examined from the CCSS side of the weld. Flaw detection rates from the SCSS side are 91% for the 500-kHz array and 73% each for the 750-kHz and 1.0-MHz arrays. However, from the CCSS side of the weld, the flaw detection rates drop to 67%, 42%, and 33% for increasing PA frequency for WOG data. If CCSS PNNL data is included, the detection rate drops to 63% at 500 kHz. Of equal importance are that marginal and no detection calls are higher within the CCSS insonification side of the weld, thus indicating the propagation difficulties caused by the large range in variability of microstructures in CCSS over SCSS materials.

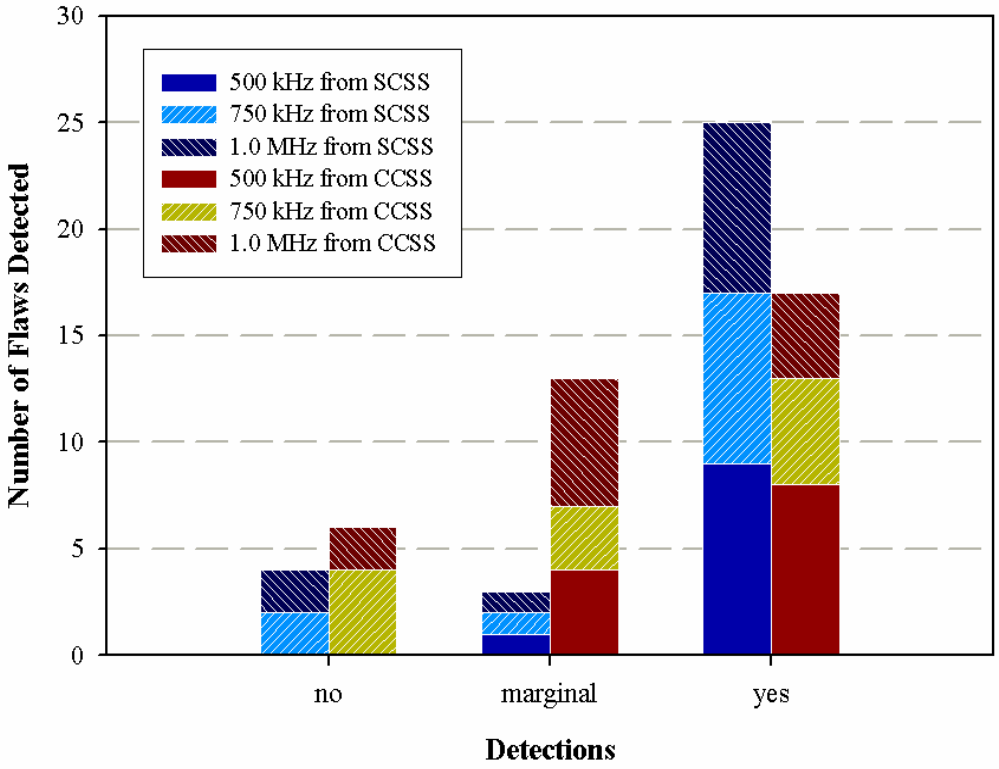

Figure 6.6 WOG Crack Detections As a Function of Insonification Side of Weld

As was shown in Section 4, the *average* grain sizes in the CCSS and SCSS materials are 1.66 and 2.54 mm (0.065 and 0.1 in.), respectively. The maximum grain size, as determined from lineal intercept measurement data, is 26.67 mm (1.05 in.) in SCSS and 26.81 mm (1.06 in.) in CCSS. However, the maximums present extremes and the average values are unrealistically small due to a limited distribution of extremely fine-grained banded regions. A more appropriate overall grain size for these materials is on the order of 12–15 mm (0.47–0.59 in.) for SCSS and 17–20 mm (0.67–0.79 in.) for CCSS microstructures. Coupling this information with theoretical ultrasonic wavelengths of approximately 11, 8, and 6 mm (0.4, 0.3, and 0.2 in.) for the 500-kHz, 750-kHz, and 1.0-MHz transducers, respectively, it is clear that scattering is significant and leads to poorer performance at higher frequencies in the larger-and more variable-grained CCSS material. With a grain size comparable to the wavelength, the scattering is largely due to reflected and refracted waves at each grain boundary. Velocity differences of up to 14% (Doctor et al. 1989) are possible in this material, leading to small reflections at each grain boundary. At grain sizes from one-tenth of the wavelength to a full wavelength in value, scattering approximates the third power of the grain size (Krautkramer and Krautkramer 1990).

This value of scattering is roughly the regime of UT wavelengths versus CSS grain sizes of the specimens used in this study, and the data show agreement with theory in that scattering increases with increasing frequency, which results in degradation of performance.

In this coarse-grained material, signal-to-noise ratios were not as high as expected and could not be used alone for a determination of flaw detection. Often, signal discrimination in multiple images was more important, and the basic presence or absence of a counterbore reflection for a reference point greatly influenced the detection call. For completeness, however, a signal-to-noise analysis as a function of flaw area was conducted. Individual signal-to-noise values for each detected flaw at the three PA probe frequencies were calculated and plotted as a function of flaw area for flaws detected from the SCSS side of the weld (Figure 6.7), and from the CCSS side of the weld (Figure 6.8). A linear regression line was fit for the data in Figures 6.7 and 6.8, showing the trend (if existing) for each frequency. As can be seen from the scattering of data and the resultant regression fits, no strong indication for increasing or decreasing trends, based on signal-to-noise ratio and flaw specular area, can be observed.

Qualitatively, a signal-to-noise value of 2 (6 dB) is typically used as a lower end for flaw detection. In these data, the highest signal-to-noise value for a marginal call was 3.0. The lowest value for a yes-detection call was 2.2. Thus, a better threshold for a detected flaw call in this study is to have a minimum signal-to-noise value equal to or greater than 2.2 (6.9 dB). However, this does not guarantee a detected flaw. Other factors such as signal discrimination aided by counterbore detection are also significant and need to be considered.

A brief review of 500-kHz PA signal responses of cracks in several WOG specimens as compared to their corresponding CCSS base material corner-trap signals was performed to determine if any correlation was evident. During the first part of this comparison, responses in the data were observed with the total system gain fixed at 40 dB and peak amplitude signals were recorded from the cracks and the corner signals on the CCSS side of the specimens. Signals were not normalized, but peaks recorded as observed. Full screen height (FSH) values are shown in Table 6.3, as well as the ratio and dB difference of associated responses.

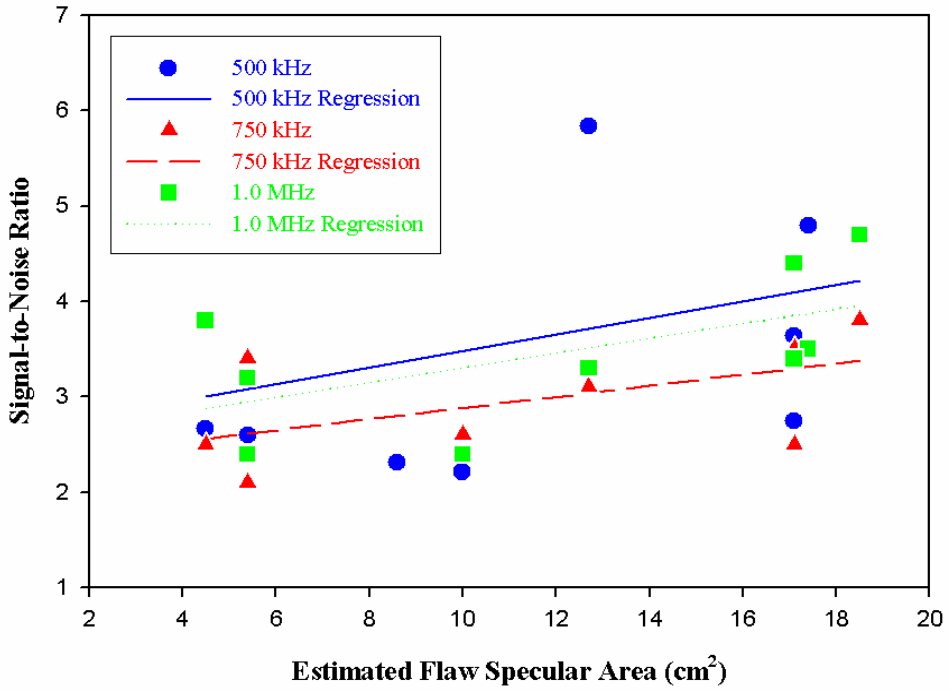

Figure 6.7 Regression Analyses of Detected Flaws Observed from SCSS Side of Welds in WOG Specimens

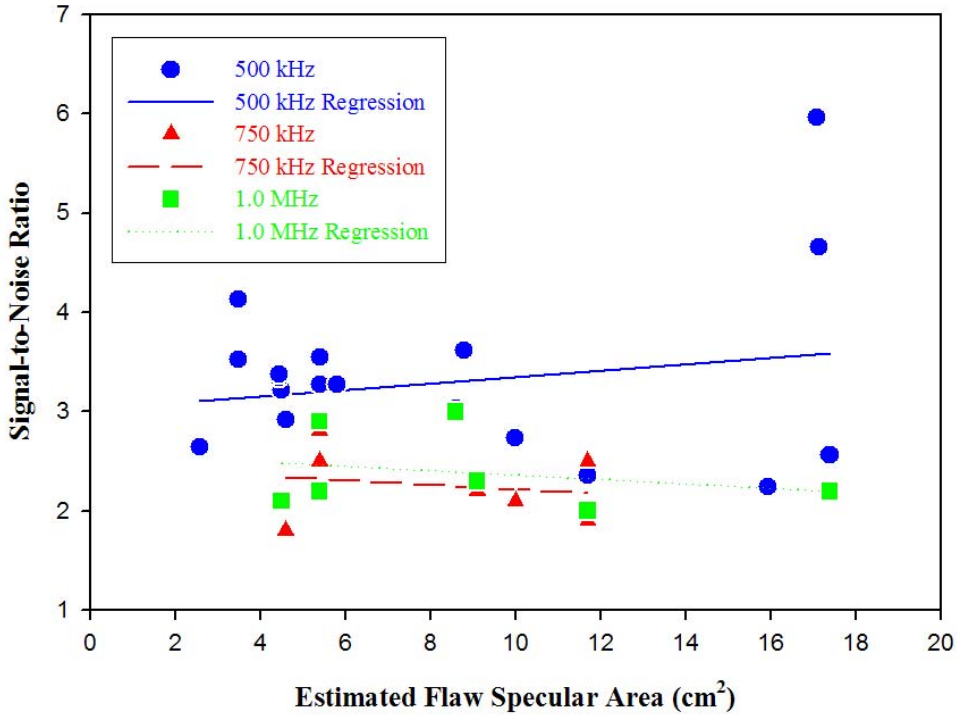

Figure 6.8 Regression Analyses of Detected Flaws Observed from CCSS Side of Welds in WOG and PNNL Specimens

Table 6.3 Peak Response Comparison for Cracks and Corner Traps in CCSS

WOG Specimen	Crack Type	Flaw Response (% FSH)	Corner Response (% FSH)	Flaw/Corner Response (fraction/dB)	Flaw SNR	Base Material SNR
APE-1	MF	57.2	89.5	0.64/−3.9	3.2	3.7
MPE-3	MF	31.1	64.0	0.49/−6.3	6.0	4.7
OPE-5	TF	53.5	87.6	0.61/−4.3	2.7	5.6
POP-7	MF	64.0	65.3	0.98/−0.17	2.6	3.8

Signal-to-noise ratio values were determined also, by normalizing the signal of interest to approximately 100% FSH. This approach accounts for differences in gain settings and coupling when comparing different data sets. The signal of interest was normalized to nearly 100% of screen height in the data analysis. The far right two columns in Table 6.3 show the flaw and end-of-block, or CCSS base material, SNR values from this part of the 500-kHz PA response analysis.

The WOG MPE-3 specimen shows the greatest difference between flaw and corner responses at -6.3 dB with POP-7 having nearly equal responses from these two signals. This analysis shows a range of responses from cracks as compared to ideal reflectors represented by the corner signals in the same CCSS material.

As one would expect, the corner response was always larger than the corresponding crack in the same WOG specimen by up to approximately 6 dB. In two of the four cases, the SNR value for mechanical fatigue cracks was slightly lower than the corner trap. For the third case, the SNR value was larger for a mechanical fatigue crack as compared to the corner trap, and in the fourth case, the thermal fatigue crack SNR value was nearly one-half the value of the corner trap in this specimen. Thus, no systematic pattern could be observed for cracks versus corner-trap SNR values.

As indicated in Section 5, background noise due to the coarse microstructures does not appear to present significant flaw detection problems (false calls) when using the 500-kHz PA method—that is, material noise responses should not produce high false call rates. However, data from several WOG specimens indicate that responses from inside surface geometries such as counterbore may obscure small flaws and could potentially cause cracks to remain undetected. Although the counterbore provides a good benchmark response to ensure adequate sound is penetrating to the ID of the piping, decreased resolution at 500 kHz, coupled with diminished bandwidth that produces repetitive echoing of these geometrical reflectors, can overshadow responses from flaw indications if the flaws are spatially located within or very near the ID geometry. This will be especially true for shallow flaws whose responses are not large enough in amplitude to be distinguished from the counterbore reflections. Examples of this effect can be seen in the PA images shown in Figures C.8, C.10, and C.12 in Appendix C. These figures show that careful analyses are required to produce distinct flaw images at 500 kHz and also indicate that a positive call is made more challenging due to the presence of the counterbore response.

Note that only obscure flaw images can be produced by the 750 kHz and 1.0 MHz PA frequencies shown in Figures C.8, C.10, and C.12.

6.2 Flaw Sizing

Time-of-flight diffraction techniques are the only proven and acceptable methods being used in the nuclear industry for through-wall sizing of detected cracks. The concept is to measure the differential time for signals to be detected from the inside surface-connected portion (corner-trap response) of the flaw and the diffracted pattern produced by the flaw tip. This time difference can be used to estimate the through-wall size, given a constant sound velocity in the material. However, throughout this study, no tip-diffracted responses from the flaws could be distinguished from baseline noise in data collected from either the CCSS or SCSS side of the welded specimens. In addition, for some cracks, it was indeterminate whether the actual corner-trapped response, or possibly, a crack face specular reflection was being detected. Therefore, through-wall sizing performance was not feasible.

A length-sizing analysis was conducted with flaw length determined by the 6-dB drop and the loss of signal (LOS) techniques on the flaws listed as detected in Table 6.1. The 6-dB drop technique sets crack-length endpoints where the signal falls below a 50% level of the peak response. The loss-of-signal technique sets the endpoints where the crack signal diminishes to baseline material, or background, noise level. As an example, a merged image for WOG specimen OPE-2 with data acquired from the CCSS side is shown in Figure 6.9. The end view on the right displays the crack with a vertical red line drawn through the center of the response. An amplitude profile for the crack is shown to the right of the image where 6-dB and LOS endpoints may be ascertained. As the magenta horizontal reference line is moved to the top and bottom measurement points, the linear position is displayed and recorded. Note in Figure 6.9 the magenta line is positioned to the lower LOS endpoint, which is measured at 8.6 cm (3.4 in.) along the scan line. The magenta line would then be moved to the upper LOS endpoint and a new line scan position measurement would be displayed. The difference in these measurements is the LOS length of the crack.

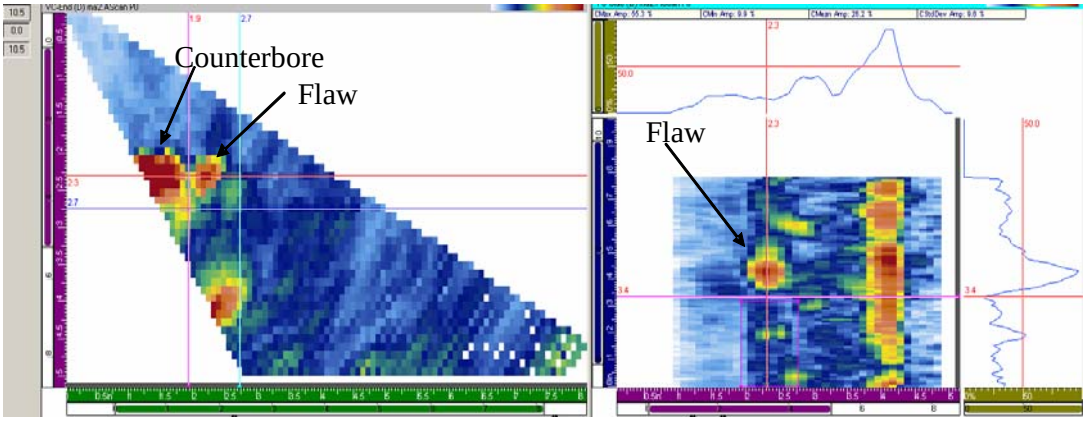

Figure 6.9 Flaw Length Sizing Method As Shown on WOG Specimen OPE-2

The signals generally had a sharp drop-off, so the two techniques produced fairly similar results. Length-sizing results are listed in Table 6.4 and the data are plotted in Figures 6.10 and 6.11.

Table 6.4 Length Sizing of Detected WOG and PNNL Flaws

WOG Specimen ID	Side UT Applied[a]	Reported Flaw Length (cm)	Flaw Length (cm) 6 dB/Loss of Signal[c]					
			500 kHz		750 kHz		1.0 MHz	
APE-1	CCSS	3.94	3.8	4.8	n/d	n/d	n/d	n/d
	SCSS[b]		4.8	6.4	3.0	3.6	3.0	4.3
APE-4	CCSS	4.19	6.6	7.4	9.9	8.4	5.6	7.1
	SCSS[b]		7.1	7.6	n/d	n/d	n/d	n/d
INEA-1	SCSS[b]	6.99	6.4	9.4	7.1	8.9	6.6	9.1
INEA-4	SCSS[b]	6.86	7.4	9.4	7.9	9.4	7.9	9.7
INEA-5	SCSS	6.73	7.4	8.4	6.1	7.6	6.9	8.4
MPE-3	CCSS	6.73	3.0	4.6	n/d	n/d	n/d	n/d
	SCSS[b]		2.8	5.6	2.3	4.1	2.5	4.1
MPE-6	CCSS	5.92	9.4	12.7	3.3	3.3	n/d	n/d
	SCSS[b]		n/d	n/d	n/d	n/d	n/d	n/d
ONP-35	CCSS	6.60	n/d	n/d	n/d	n/d	n/d	n/d
ONP-38	CCSS	5.13	n/d	n/d	0.8	1.3	n/d	n/d
ONP-D2	CCSS[b]	6.60	n/d	n/d	0.7	1.0	n/d	n/d
ONP-D5	CCSS[b]	4.06	1.1	1.6	n/d	n/d	n/d	n/d
OPE-2	CCSS	4.19	3.6	5.8	4.1	5.3	3.8	4.6
	SCSS[b]		3.6	8.4	3.3	4.3	4.8	6.4
OPE-5	CCSS	6.15	4.1	5.1	n/d	n/d	n/d	n/d
	SCSS[b]		6.4	7.1	3.3	5.3	5.1	6.6
POP-7	CCSS	6.78	3.0	4.6	n/d	n/d	4.6	5.3
	SCSS[b]		4.1	5.6	3.0	5.3	3.8	5.6
POP-8	CCSS[b]	5.72	n/d	n/d	n/d	n/d	2.5	4.1
	SCSS		1.8	2.8	n/d	n/d	n/d	n/d
B501	CCSS-Col.	2.92	n/d	n/d				
	CCSS-Eq.[b]		3.3	4.83				
B504	CCSS-Col.	6.15	4.57	5.59				
	CCSS-Eq.[b]		2.54	3.56				
B505	CCSS-Col.	5.72	3.56	4.32				
	CCSS-Eq.[b]		3.81	4.32				
B508	CCSS-Col.[b]	4.83	n/d	n/d				
	CCSS-Eq.		n/d	n/d				
B515	CCSS-Col.	2.92	2.29	3.81				
	CCSS-Eq.[b]		3.30	5.59				
B519	CCSS-Col.	5.72	n/d	n/d				
	CCSS-Eq.[b]		2.79	4.06				
B520	CCSS-Col.[b]	2.67	2.54	3.05				
	CCSS-Eq.		n/d	n/d				

WOG Specimen ID	Side UT Applied[(a)]	Reported Flaw Length (cm)	Flaw Length (cm) 6 dB/Loss of Signal[(c)]		
			500 kHz	750 kHz	1.0 MHz

Notes and Definitions:

(a) Denotes from which side of the weld the PA UT was applied; CCSS = centrifugally cast stainless steel, SCSS = statically cast stainless steel, CCSS-Col. = columnar grain structure, CCSS-Eq. = equiaxed grain structure

(b) Denotes side of weld on which the flaw is located

(c) n/d = flaw only marginally, or not, detected

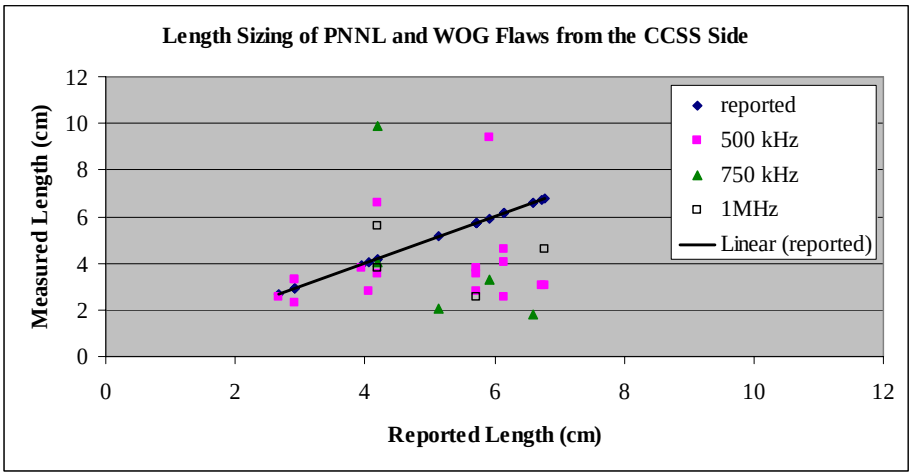

Figure 6.10 Length Sizing Results on Detected WOG and PNNL Flaws Using 6-dB Amplitude Drop as Inspected from CCSS Side of Weld

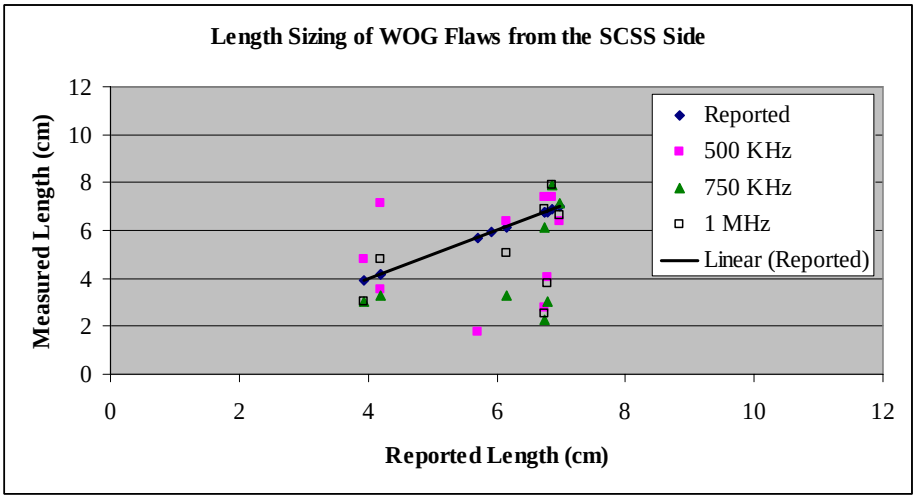

Figure 6.11 Length Sizing Results on Detected WOG Flaws Using 6-dB Amplitude Drop as Inspected from SCSS Side of Weld

The trend of the measured values shows that the phased array methods used in this study generally undersize the flaw length, which is understandable in this coarse-grained material. The base metal study (in Section 5) showed that a corner signal, which can be thought of as a through-wall flaw over the length of inspection, was intermittently detected. The material properties lead to this on/off effect and will cause flaws to be partially detected in length and therefore undersized.

The error calculated as the root mean square error (RMSE) in Table 6.5 shows mixed results. The 1.0-MHz transducer gives the least error. This is likely due to a smaller beam size as compared to the other two probes. Note that this error is based on detected flaws, and the 1.0-MHz transducer had the poorest detection rate. The data in Table 6.5 also show that the 500-kHz and 1.0-MHz transducers perform similarly from either the CCSS or SCSS side of the weld while the performance of the 750-kHz transducer is better from the SCSS side.

Table 6.5 Length Sizing of Detected WOG Flaws Using 6-dB Drop Method

Frequency	Flaw Length-Sizing Error (RMSE)		
	CCSS	SCSS	Combined
500 kHz	2.54 cm (1.0 in)	2.22 cm (0.87 in)	2.37 cm (0.93 in)
750 kHz	3.81 cm (1.5 in)	2.37 cm (0.93 in)	3.00 cm (1.18 in)
1.0 MHz	2.07 cm (0.81 in)	1.93 cm (0.76 in)	1.98 cm (0.78 in)

Length sizing errors from the PNNL data are shown in Table 6.6 for the CCSS columnar and equiaxed material at 500 kHz. While the sizing errors are smaller for this material, it should be noted that there are other factors to consider in these results. All of the PNNL flaws were located close to the edge of the specimen (flaws started within approximately 2.5 cm from the edge) so the sound field reflected from the flaw is adversely affected by interactions with the edge of the sample. Additionally, the large footprint of the 500 kHz probe prohibited full insonification of the flaw on the end close to the specimen edge. This would lead to an undersizing of the flaw. Skewing the beam often provided an end point to the flaw that was not seen in the unskewed data.

Table 6.6 Length Sizing of Detected PNNL Flaws at 500 kHz

	Flaw Length-Sizing Error (RMSE)	
Sizing Technique	CCSS – Columnar	CCSS – Equiaxed
6 dB	1.37 cm (0.54 in.)	2.26 cm (0.89 in.)
LOS	0.89 cm (0.35 in.)	2.10 cm (0.83 in.)

To rule out potential beam forming irregularities of the phased arrays for the length-sizing error observed, the data for flaws with the sound directed from the fine-grained wrought stainless steel (WSS) side of the welds were analyzed. The WOG specimens that afforded this configuration are the INE-A type (see Appendix A, Figure A.2). Sizing results were compared with those from the CSS side. Table 6.7 provides the resulting 6-dB and LOS values, as well as RMS error for these three specimens, as a product of flaw length-sizing from the wrought side of the welds.

Table 6.7 Phased Array Length-Sizing Measurements from Fine-Grained Material

Specimen	Reported Flaw Length (cm)	Flaw Length (cm) from WSS Side of Weld 6 dB/Loss of Signal					
		500 kHz		750 kHz		1.0 MHz	
INE-A-1	6.99	6.10	11.94	5.08	7.87	4.32	5.33
INE-A-4	6.86	8.89	9.65	8.13	8.64	7.62	8.13
INE-A-5	6.73	5.08	5.33	6.10	7.87	6.35	7.11
Root Mean Square Error		1.59	3.38	1.37	1.32	1.61	1.22

As one can readily see, length-sizing performed with data acquired from the fine-grained wrought stainless steel side of the welds in these WOG specimens is much better than from the coarse-grained CSS materials. The RMSE values (although calculated with only 3 data points), with the exception of the LOS method at 500 kHz, all meet the 1.91-cm (0.75-in.) RMSE limits imposed for acceptable length-sizing found in the ASME Boiler and Pressure Vessel Code, Section XI, Appendix VIII, Performance Demonstration for Ultrasonic Examination Systems. This comparison therefore shows that the phased arrays are functioning adequately in the passive aperture direction, and that length-sizing error exhibited in Tables 6.4, 6.5, and 6.6 can be attributed to the coarse-grained microstructures of SCSS and CCSS.

An example of comparing the images available for sizing is shown as Figure 6.12. Note the general asymmetric and irregular shape of the images as observed in the data collected from the SCSS side of this INE-A specimen. Compare these to the same flaw images collected from the WSS side of the weld, which exhibit more linear and consistent amplitude responses; this facilitates placing the reference cursers (shown as red and blue lines) in the correct position to acquire more accurate length measurements.

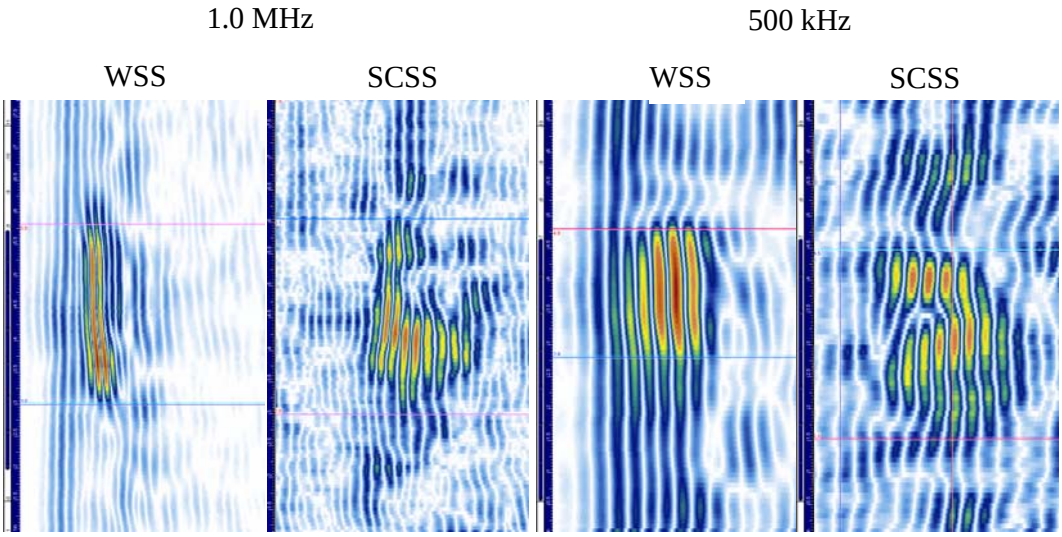

Figure 6.12 Images for Comparing Length-Sizing Capabilities at 1.0 MHz and 500 kHz in Fine-Grained Stainless Versus Cast Material

7 Summary and Conclusions

The volumetric examination of CSS piping in operating nuclear power plants remains a significant challenge to NDE technologies. Low-frequency UT offers the capability to penetrate relatively thick-walled sections of primary piping circuits. However, detection and characterization of flaws is problematic due to the varied microstructures of both CCSS and SCSS materials. During this study, we built upon decades of low-frequency/SAFT UT work at PNNL by migrating to an approach that uses state-of-the-art phased array methods operating at low frequencies to determine if detection and sizing of flaws could be improved. Phased array techniques offer the ability to electronically steer the UT beam through multiple propagation angles nearly simultaneously so that if "windows" for optimum material penetration exist, these may be more readily accessed. Phased array systems are being increasingly deployed on a wide range of component inspections because their use allows a more rapid examination than conventional automated UT while providing enhanced imaging capabilities to facilitate data analyses.

Longitudinal waves produced by dual phased arrays operating at 500 kHz, 750 kHz, and 1.0 MHz, and a conventionally designed dual transducer operating at 400 kHz, were applied to thick-section (65–80 mm, or 2.6–3.3 in.) unflawed CCSS piping segments to determine whether ultrasound at these frequencies could be expected to adequately penetrate the varied microstructures and to assess inherent background noise that may interfere with detection and characterization of flaws. The work indicated that the lower range of frequencies—for example, 400 and 500 kHz—produced the best overall corner-trap responses obtained from the machined end of the specimens.

Over normalized scan lengths, the 400-kHz SAFT-processed images provided the most consistent corner detection, while the best SNR was obtained from the 500-kHz phased array method. Both techniques used large-aperture focusing probes to enhance sound propagation, but the advantage of the phased array is that multiple-angle beams were electronically transmitted nearly simultaneously and may have enabled better penetration when a wide range of grain sizes and shapes were confronted. The frequency response from returned corner-trap signals in vintage CCSS shows that 500 kHz is a stable operating frequency, while higher frequencies exhibit variability and filtering due to the microstructures. It should be noted, however, that certain vintage CCSS microstructures, especially those with multiple layers and grain sizes on the order of 20–25 mm (0.8–1.0 in.), produced signal loss and high background noise in certain areas of the tested segments. Similar CCSS microstructures may be present in portions of primary coolant system piping of early Westinghouse-designed nuclear power plants, and in these areas, ultrasonic inspection reliability will be affected. This research has shown that the use of large-aperture, low-frequency phased arrays, coupled with careful analyses of data images, is necessary to support robust and effective examination of this material.

Baseline analyses of unflawed parent material indicate that vintage CCSS piping microstructures may produce limited areas of diminished UT response, and the SNR of signals in these areas may fall below 2. (Most conventional UT procedures require a SNR of ≥ 2 for a positive detection call to be made.) However, as with all modern UT methods, flaw amplitude does not provide a singular basis for detection, and especially in CCSS, SNR for actual crack responses

should not be used as a primary indicator for flaw detection. The unflawed CCSS piping segments available for this study consisted of only a small population of circumferential piping material. However, from the results of detected corner-trap responses using the 500-kHz PA probe, the largest contiguous regions exhibiting diminished UT response were approximately 10 cm (4 in.) in circumferential length. These areas of low SNR may have little consequences, given the high fracture toughness of CCSS piping under normal reactor operating conditions. Flaws would need to be 5 to 10 times longer than these worst-case areas of diminished UT response to challenge structural integrity (Diaz et al. 1998). Therefore, it is concluded that structurally significant cracks would be detected in CCSS, as these cracks would extend well beyond the diminished response regions.

The 500-kHz PA data show that background UT noise due to scattering from the CCSS grains does not appear to cause detected responses that one might misinterpret as a crack. Reflections produced solely by the microstructure are generally much lower in amplitude and very short in length, which indicates that the CCSS material may not significantly contribute to a high false call probability. However, it was noted that small flaws located very near ID geometry, such as counterbore, may be overlooked because of the large-amplitude, and broad time-base responses from these geometrical reflectors. Of course, only a small number of flawed specimens having ID geometrical features adjacent to thermal and mechanical fatigue cracks were available for this study. Because of the small population of specimens, final conclusions cannot be made regarding the limitations to flaw detection as a function of spatial location relative to geometrical reflectors.

Further, OD weld profiling and ID contour mapping using focused straight-beam methods should be performed on all CCSS welds prior to implementing any angle beam UT procedure. This is a standard practice with other austenitic piping examinations that rely on discriminating cracks from ID geometrical reflectors, such as in the detection of intergranular stress corrosion cracks in recirculation systems of boiling water reactors. By using these techniques, one gains an understanding of the cross-sectional features of the weld and adjacent base material that may lead to non-relevant UT reflections and potentially obscure service-induced degradation.

The ability of low-frequency phased array methods to detect and characterize flaws was explored using a set of specimens developed by industry. The WOG specimens contain mechanical and thermal fatigue cracks adjacent to welds joining CSS materials in configurations representative of those installed in Westinghouse-designed primary coolant systems. Both CCSS and SCSS piping materials were used to fabricate these short circumferential piping segments, which exhibit inside and outside surface geometries one would expect to encounter in large-bore reactor coolant circuit welds. Phased arrays operating at 500 kHz, 750 kHz, and 1.0 MHz were applied from the outside surface to detect the inside surface-breaking cracks. Line scans adjacent to the welds were performed using inspection angles from 30–60°. It should be pointed out that applying line scans may be the only feasible method of acquiring acceptable data on these components, considering the large footprints (~85 × 85 mm) of low-frequency probes and tapered outside surface geometries that may exist. Conventional raster scanning would be severely constrained due to flat/ground limited surface availability. However, it may be possible through careful modeling and evolving fabrication methods, to construct improved low-

frequency phased arrays with smaller footprints, or with new designs that incorporate flexible arrays that would contour to challenging surface conditions.

Crack detections were made by careful analyses of composite data images acquired from both CCSS and SCSS sides of the welds. The 500-kHz phased array proved to be the better performer, with a combined detection rate of approximately 77% (91% from the SCSS and 63% from the CCSS). The performance of the 750-kHz and 1.0-MHz arrays was significantly affected by the microstructure of the CSS materials, with detection rates of around only 50% for each frequency. As expected, thermal fatigue cracks are generally more difficult to detect than mechanical fatigue cracks; this is shown by detection capabilities of the 500-kHz array (the best performer), with 93% of mechanical fatigue cracks being detected versus only 57% of those produced by thermal fatigue. This is simply an observation because only a small and unequal population and size distribution of mechanical and thermal fatigue cracks were available for this study. However, the result is consistent with previous work on these cracking processes reported in Becker et al. (1981).

Crack detection is highly influenced by the material through which the ultrasonic wave must propagate in order to insonify the crack. The CCSS piping presented the more challenging microstructure and resulting varied acoustic properties; consequently, detection performance was lower from this side of the weld. We do not believe that dendritic weld structures greatly influenced beam propagation at 500 kHz. Parent material microstructure (SCSS versus CCSS) appears to dominate attenuation of the sound beam, as no trend was observed to indicate enhanced detection based on whether the flaws are located on the near- or far-side of the weld. Again, only a small number of flaws were available, so this observation could not be fully explored.

Length sizing was attempted for all detected cracks. Measurements were made by using standard 6-dB drop and loss-of-signal techniques to ascertain the overall length of these flaws. The results were poorer than expected but not surprising, given the CSS microstructural effects on ultrasonic sound fields. Beam redirection and partitioning, which especially affects side-to-side resolution (passive dimension of the arrays), caused the length-sizing RMSE to be approximately 24 mm (0.95 in.) for the 500-kHz array. The 1.0-MHz array performed better, with an RMSE of approximately 20 mm (0.79 in.). The theoretical beam spot size at the appropriate depth within homogeneous and isotropic stainless steel material is estimated to be approximately 20 mm (0.79 in.) for the 500-kHz, and 14 mm (0.55 in.) for the 1.0-MHz, phased array probes and would degrade in propagating through CSS materials. Length-sizing resolution is directly proportional to the beam diameter, or focal spot size, of the probe at a given depth in the material. This suggests that the best length-sizing performance possible would be on the order of the beam diameter values stated above. However, as evidenced by the RMSE values obtained in this study, the coarse microstructure resulted in degradation of length-sizing capability for thick-walled CSS piping. The general trend for these low-frequency arrays is to undersize the length of the cracks. This is consistent with results of the corner-trap responses on the unflawed CCSS segments described above, in that portions of the crack response may be significantly diminished over the crack length so that images of the flaws are shorter than actual length. Also, if shallow flaws cannot be reliably detected, and the crack shape tends to be semi-

elliptical so that the ends have only confined areas for reflection, the length of the crack will be undersized.

The reader should note that no through-wall sizing was attempted for any of the WOG specimen flaws. Modern depth-sizing techniques rely upon detecting a signal from the inside surface corner trap (crack opening) and a crack-tip diffracted response denoting deepest penetration into the material. The time difference between these two responses, for a given inside surface-breaking crack, can be used to calculate the depth of penetration. However, for the low-frequency techniques applied in these challenging CSS materials, it is unclear whether detected crack responses are from the inside corner trap or simply specular reflections from the crack face. In addition, tip-diffracted signals are generally much lower in amplitude (approximately −20 dB from typical corner-trap responses) and were not distinguishable from inherent background noise in the material. Therefore, standard depth-sizing methods could not be used to estimate through-wall dimensions of the cracks.

It is concluded that 500-kHz large-aperture phased arrays are capable of detecting ID-connected cracking in heavy-walled CSS piping when inspected from the OD surface of the pipe. The results show that for inside surface-breaking thermal and mechanical fatigue cracks greater than approximately 30% through-wall in depth, the 500-kHz method detected 100% of the flaws, provided that access to the outside surface was sufficient for adequate transducer placement and coupling. Further, cracks smaller than 30% through-wall could also be periodically detected with the 500-kHz phased array method. No through-wall sizing of flaws was performed due to an absence of tip-diffracted responses. Length sizing is possible, although the RMSE is slightly higher than currently allowed by the ASME Code, Section XI, Appendix VIII, Supplements 2 and 3. Many industry personnel have argued that current NDE technologies are not capable of inspecting cast austenitic piping materials. This study strongly refutes that contention and provides evidence that automated low-frequency PA methods, while not fully explored, have the potential to detect and length-size cracks in CCSS reactor primary coolant piping welds.

This study shows automated low-frequency phased array technology to be capable of detecting cracks and, therefore, superior to conventional UT methods for CSS materials installed in primary coolant piping at nuclear power plants. This suggests that low-frequency phased array methods be used to supplant current examination techniques, which typically employ manual 1.0-MHz transducers, for increasing the reliability of weld inspections in these systems. It should be noted that only heavy-walled, large-bore specimens, indicative of primary reactor coolant circuits, were evaluated during this research, and ultrasonic technique variables may differ for CSS piping that is thinner-walled and/or smaller in diameter. Future PNNL plans include performing ultrasonic research on thinner-walled CSS piping, such as might be found in pressurizer surge lines.

Based on reasonably high flaw-detection capabilities, low responses due to coherent sound energy from the grain structures (high responses may result in false calls), and the limited areas of reduced signal response, automated low-frequency phased arrays are shown capable of detecting structurally important cracks in CSS weldments. Because of the complexity of data acquisition and analysis methods using phased arrays to detect service-induced cracks on these coarse-grained microstructures, examiners, equipment, and procedures need to demonstrate

effective performance—for example, to the criteria specified in the ASME Code Section XI, Appendix VIII—for reliable ISI deployment.

8 References

ASME. 2004. "Rules for Inservice Inspection of Nuclear Power Plant Components, Section XI." In *ASME Boiler and Pressure Vessel Code – An International Code.* American Society of Mechanical Engineers, New York.

Anderson MT, SE Cumblidge, and SR Doctor. 2003. "Applying Ultrasonic Phased Array Technology to Examine Austenitic Coarse-Grained Structures for Light Water Reactor Piping." Presented at the Third EPRI Phased Array Inspection Seminar, June 9–11, 2003, Seattle, Washington.

Bates DJ, SR Doctor, PG Heasler, and E Burck. 1987. *Stainless Steel Round Robin Test: Centrifugally Cast Stainless Steel Screening Phase*. NUREG/CR-4970, PNL-6266, PISC III Report No. 3, U.S. Nuclear Regulatory Commission, Washington, D.C.

Becker FL, SR Doctor, PG Heasler, CJ Morris, SG Pitman, GP Selby, and FA Simonen. 1981. *Integration of NDE Reliability and Fracture Mechanics, Phase 1 Report.* NUREG/CR-1696, PNL-3469 Vol. 1, U.S. Nuclear Regulatory Commission, Washington, D.C.

Diaz AA, SR Doctor, BP Hildebrand, FA Simonen, GJ Schuster, ES Andersen, GP McDonald, and RD Hasse. 1998. *Evaluation of Ultrasonic Inspection Techniques for Coarse-Grained Materials.* NUREG/CR-6594, PNNL-11171, U.S. Nuclear Regulatory Commission, Washington, D.C.

Doctor SR, JD Deffenbaugh, MS Good, ER Green, PG Heasler, FA Simonen, JC Spanner, and TT Taylor. 1989. "Inspection of CCSS." Section 6.3 in *Nondestructive Examination (NDE) Reliability for Inservice Inspection of Light Water Reactors -- Semi-Annual Report, April-September 1988.* NUREG/CR-4469, PNL-5711 Vol. 9, U.S. Nuclear Regulatory Commission, Washington, D.C.

Good MS, BP Hildebrand, and CM Batson. 1990. "Phase Mapping of Ultrasonic Fields Passed Through Centrifugally Cast Stainless Steel." In *Review of Progress in Quantitative Nondestructive Evaluation,* Vol. 10B, pp. 1975–1982. American Institute of Physics, Melville, New York.

Good MS. 1991. "UT Measurements Performed on CCSS Material Contained within PISC III Action 3 NDW Assembly 25." Appendix C in *Nondestructive Examination (NDE) Reliability for Inservice Inspection of Light Water Reactors -- Semiannual Report, October 1990-March 1991*. NUREG/CR-4469, PNL-5711 Vol. 13, U.S. Nuclear Regulatory Commission, Washington, D.C.

Heasler PG and SR Doctor. 1996. *Piping Inspection Round Robin*. NUREG/CR-5068, PNNL-10475, U.S. Nuclear Regulatory Commission, Washington, D.C.

Jeong YH. 1987. *An Ultrasonic Material State Classifier for Elastically Anisotropic Materials*. Doctoral dissertation, Department of Mechanical Engineering and Applied Mechanics, Drexel University, Philadelphia, Pennsylvania.

Krautkramer J and H Krautkramer. 1990. *Ultrasonic Testing of Materials*. 4th ed. Springer-Verlag, Berlin.

Poguet J, J Marguet, F Pichonnat, and L Chupin. 2001. "Phased Array Technology: concepts, probes and applications." Presented to the Third International Conference on NDE in Relation to Structural Integrity for Nuclear and Pressurized Components, November 14–16, 2001, Seville, Spain.

Taylor TT. 1984. *An Evaluation of Manual Ultrasonic Inspection of Cast Stainless Steel Piping*. NUREG/CR-3753, PNL-5070, U.S. Nuclear Regulatory Commission, Washington, D.C.